Chapter 1

Introduction

1.1 Preface

Alternative energy to fossil fuel and a decrease in the release of greenhouse gases are major challenges to face at the beginning of this century. Molecular hydrogen is expected to be the ideal fuel source for global human activity, as it is a clean burning energetic molecule. A key technology in the drive towards a hydrogen economy is the development of efficient fuel cells which allow the cold combustion of hydrogen with oxygen to produce electrical rather than thermal energy. When dihydrogen is burned or oxidised in a fuel cell it emits no pollution, and gram for gram it releases more energy than any other fuel. Thus, it provides hope as an alternative to all carbon based energy sources that are believed to be responsible for global warming. [1, 2]

Dihydrogen production as a fuel and its use as an energy source by coal combustion in fuels cells are central to advance a hydrogen economy. Four main techniques are currently used for molecular hydrogen production, *i.e.* hydrocarbon reforming, ammonia cracking, pyrolysis (decomposition of hydrocarbons into dihydrogen and carbon in water-free and air-free environment) and aqueous reforming. [3, 4] Unfortunately, all these methods utilise unsustainable hydrocarbon feedstock and release greenhouse gases, which is clearly not "green" enough. However, despite the negative commentary, the way dihydrogen is produced can provide the transitional

capacity as infrastructure is developed and alternate ways of generating dihydrogen using solar, nuclear, hydro, wind, or wave energy come to the fore. [5, 6] Hydrogen fuel or producer cells based on the interconversion of **Equation 1.1** will play a major part in such an economy. [7]

$$H^+ + e^- \leftrightarrow \frac{1}{2}H_2 \qquad \textbf{Equation 1.1}$$

However, formation and utilisation of molecular hydrogen require electrode materials that can sustain high current densities for oxidation of dihydrogen or reduction of protons close to the thermodynamic potential of the reversible reaction. By far the best materials for this are platinum and palladium. This is attributed to the M-H bond where M = platinum (Pt) or palladium (Pd), being strong enough to ensure high surface coverage, but weak enough to allow coupling of surface H atoms and desorption of dihydrogen. These metals are of very low abundance and have been recognised as being economically unviable in the long term, due to their limited availability. Living organisms have used and produced molecular hydrogen for millions of years. Mediators of hydrogen metabolism in living organisms such as Achaea, Bacteria and Eukarya are key enzymes called hydrogenases. They catalyse the simplest chemical reaction: the reversible conversion of protons to dihydrogen. Their structure is however extremely complex and the comprehension of their action remains, to date, a fundamental question. Understanding and expanding the chemistry of the hydrogenases by the design of artificial enzymes or "convergent" chemical systems which utilise biomechanistic insights provides crucial challenges to all chemists and biochemists. [5]

1.2 Biomimetism of enzymes-Hydrogenase

Biomimetic chemistry portrays chemistry that is inspired by that done in living systems. It has always been the chemists' vision to catalyse reactions the way enzymes do: working at room temperature and low pressure, using simple starting materials like nitrogen to make only useful products and benign by-products, like ammonia and water.

One of the obstacles to understanding enzymes is their large size. Each enzyme comprises thousands of atoms, with various sections of an enzyme performing different functions. The "active site", located at a specific position within the enzyme is where the reacting molecules come together, break apart, and recombine as they interact with the enzyme, and then leaves as different molecules. Other sections of the enzyme can block the active site, allowing access to only certain molecules, or permitting approaches to the active site from only one direction.

Artificial enzymes are an important part of this field, in which one tries to imitate the catalytic process that occurs in the wild type of an enzyme, and not just the substances of biology. The studies of artificial enzymes help us to understand and to evaluate the properties of natural enzymes. One great challenge to overcome using artificial enzymes is the outstanding catalytic activity that the best natural enzymes can achieve, promoting chemistry at rates which are not available with "conventional" catalysts.

One example is the reversible reduction of proton to dihydrogen as indicated in **Eq. 1.1**. This is deceptively the simplest of reactions, but also one that requires multistep catalysis to proceed at practical rates. Yet, in nature, the members of an enzyme class called hydrogenases can easily perform this reaction with exceptional efficiency, with

rates for proton production in the range of 6000-9000 turnovers per second and dihydrogen production of 10000 turnovers per second. [8, 9] This type of enzyme was first discovered by Stephenson and Stickland in 1931 when they demonstrated that colon bacteria could evolve and use H_2 to reduce artificial and physiological substrates. [10]To date, all of the known hydrogenases are rich in sulphur and iron. Based on the structure of the active site, the enzymes are divided into three classes:

i. [Fe]-hydrogenases (formerly known as iron-sulphur cluster-free hydrogenases) contain one Fe atom coordinated with two carbonyls, CO and one water, H_2O ligand. [11] They are found in methanogenic archea and are exclusively specialised in H_2 oxidation. An organic cofactor (methylenetetrahydromethanopterin) plays an essential role in the catalytic mechanism of this class of enzymes.

ii. [FeFe]-hydrogenases (formerly called iron-only hydrogenases) contain a unique binuclear Fe cluster which is connected to a conventional cubane {4Fe-4S} cluster. It contains an unusual CO and cyanide, CN^- ligands to the binuclear cluster. These hydrogenases occur in a wide variety of microorganisms, mostly however, in anaerobic sulphur reducing bacteria [12, 13] and mono cellular algae. [14]

iii. [NiFe]-hydrogenases contain a binuclear Ni-Fe complex coordinated by CO and CN^- ligands. This group of hydrogenases is most widely distributed in nature and is relatively well studied. [13, 15, 16] The enzymes occur in several types of bacteria living in regions with a higher oxygen concentration.

Among these, [NiFe] and [FeFe]-hydrogenases have received much interest from biologists, biochemists, and chemists over 25 years. This is because both classes of hydrogenases are able to catalyse either proton reduction or dihydrogen oxidation, but it is commonly claimed, according to their different affinities for molecular hydrogen that [FeFe]-hydrogenases have greater activity for H_2 production, [9] while [NiFe]-hydrogenase is more efficient for dihydrogen uptake. Moreover, the activity of [NiFe]-hydrogenases is lower than that of [FeFe]-hydrogenases, while the latter seem to be more sensitive towards oxygen and inhibition by carbon monoxide. [17] A more detailed discussion on [FeFe]-hydrogenases can be found in **Chapter 2**.

1.3 Artificial hydrogenases based on active site analogues

One of the main directions of study is to prepare synthetic analogues of the active site of metal containing enzymes, in order to reproduce their catalytic activity. The advantage of such models is that they are smaller and therefore easier to handle, in terms of isolation and spectroscopic data collection, than the enzyme itself. The success of a synthetic catalyst is based on three characteristics: cost, efficiency and robustness:

i. A good catalyst is a cheap catalyst; hydrogenases are fascinating because they catalyse the **Equation 1.1** reaction interconversion at high rate and small overpotentials from equilibrium, using cheap first row transition metals at the active sites, such as iron, nickel and cobalt. Mimicking the functions of the active site of an enzyme could lead to the replacement of unsustainable platinum electrocatalysts in electrolyser/fuel cell applications. The replacement of platinum with inexpensive materials is critical to the large-scale use of molecular hydrogen as a clean energy vector.

ii. A good catalyst is an economically viable catalyst; application of an electrocatalyst in a large-scale electrolyser or fuel cell obviously requires high turnover frequencies to achieve high currents and low overpotential. From the viewpoint of solar energy conversion, the development of photocatalysis for overall water splitting is an attractive goal.

iii. A good catalyst is a robust catalyst; the crucial point for any technological application is the robustness of the catalyst, which means both thermodynamic and kinetic stability under normal atmospheric conditions and high turnover numbers. Up to now, all promising molecular chemical systems for proton reduction or dihydrogen uptake have been abandoned because they were not reliable enough. The following aspects have to be taken into consideration: (1) involvement of two electron transfers in the catalytic cycle implies that the selected catalysts, at the deprotonated or hydridic state (depending on the mechanism), should display electrochemically and chemically reversible redox features occurring at a relatively mild potentials, to avoid any irreversible ligand decomposition. (2) The chelate effect has been widely used as a general strategy for the design of robust complexes. By preventing ligand exchange in the active intermediate states, this indeed ensures the conservation of the entire set of ligands governing the reactivity of the metallic centre over the catalytic cycle. Note that the biomimetic approach could be in contradiction with this strategy, since the carbonyl ligand could be likely subjected to irreversible displacement during catalysis.

1.4 Outline of thesis

The outline of this PhD thesis is as follows:

Chapters 1 and 2 briefly give an introduction and the literature background about hydrogenases respectively. This chapter, Chapter 1, has provided a general introduction to the scope of this work in the context of the background literature on hydrogenases. Chapter 2 develops this in more detail, with a focus on the structure and mechanism of action of the hydrogenases and a description of synthetic models, particularly those related to the sub-site of [FeFe]-hydrogenase.

Chapter 3 describes the synthesis of materials used in the studies detailed in this thesis. This covers the synthesis of iron-sulphur materials such as the {4Fe-4S} cubane, the artificial sub-site containing the {2Fe-2S} centre and the synthesis of functionalised ligands for modifying electrode surfaces and protein. In the context of electrode surface modification, the synthesis of key monomers which can be electropolymerised is described.

Chapter 4 is concerned with building a structure related to [FeFe]-hydrogenase on electrode surfaces. First, we show how the incorporation of a sub-site unit into an ionic polymer can stabilise the hydride form by protonation. In further work on electrode assembly, we describe the construction and characterisation of an electrode surface chemistry which possesses H-cluster type unit.

Chapter 5 describes attempts to construct an H-cluster within a mutant ferredoxin extracted from hyperthermophile *Pyrococcus furiosus*.

Chapter 6 reports the construction of a photoelectrochemical platform for molecular hydrogen production which is based on the modification of indium phosphide nano-crystals and the incorporation of procatalyst which has a framework nominally related to the catalytic diiron sub-site of [FeFe]-hydrogenase.

1.5 Objectives

The goals of this PhD thesis are as follows:

Firstly, the synthesis and characterisation of [FeFe]-hydrogenase biomimetic synthetic derivatives in order to provide the spectroscopic and reactivity precedent for the biological systems.

Secondly is to explore new functionalisation of electropolymerisation method in protonation studies of iron sub-site and the construction of an artificial hydrogenase active site on electrode surface with the prospect of producing new material assembly for dihydrogen production.

Third, is to study the electrochemical behaviour related to active site of [FeFe]-hydrogenase based on reaction between mutant ferredoxin extracted from hyperthermophile *Pyrococcus furiosus* and synthetic diiron sub-site.

Fourth is to construct a photoelectrochemical platform for hydrogen production which based on modification of indium phosphide nanocrystals and incorporation of a procatalyst which has a framework nominally related to the catalytic diiron sub-site of [FeFe]-hydrogenase.

Chapter 2

Iron-sulphur centres in biology and related chemistry: An overview of the hydrogenases

This chapter describes the iron-sulphur centre in biology, with particular focus on those found in hydrogenases and on the chemistry related to synthetic and mechanistic mimics of diiron dithiolate carbonyls which resemble the sub-site of the H-cluster of [FeFe]-hydrogenase.

Although there is much interesting model chemistry reported and newly emerging which is related to the [NiFe]- and mono [Fe]-hydrogenases, only [FeFe]-hydrogenase model chemistry pertinent to this thesis is reviewed.

2.1 Iron proteins: Properties and biology

Iron (Fe) is everywhere. It is the second most abundant metal (after aluminium) and the fourth most abundant element in the Earth's crustal rock (after oxygen, silicon and aluminium). The relative atom mass of iron is 55.847 $g.mol^{-1}$ and its electronic configuration is $[Ar]3d^6 4s^2$. A wide range of oxidation states exists for iron in between two extremes of -II and +VI. Iron complexes with oxidation states over +III are rare and it is for +II and +III that iron is mostly represented chemically as well as biologically. Lower oxidation states are confined mainly to its carbonyl and phosphine

complexes. [18] Due to its availability, iron has been widely involved in living systems where it is responsible for vital biological mechanisms such as dioxygen uptake, transport and storage and electron transfer.

Metalloprotein is a generic term for a protein that contains a metal ion cofactor. Iron protein specifically means that the protein contains iron. [19] Iron protein can be classified into two categories namely *heme* and non-*heme* iron proteins as depicted in **Table 2.1**. Haemoglobins, myoglobins and cytochromes are *heme* proteins as they are characterised by the presence of the *heme* group where Fe is coordinated to a porphyrin ligand. Apart from these, all other proteins such as iron-sulphur proteins belong to the non-*heme* classification. Iron-sulphur proteins are widely distributed in living organisms, they play key roles as electron carriers in processes such as nitrogen fixation, dihydrogen evolution-consumption and photosynthesis. [20]

Table 2.1. Some proteins containing iron.

	Protein	**Function**	**Source**	**No. of Fe atoms in molecule**
Heme	Haemoglobin	O_2 transport	Animals	Four *hemes*
	Myoglobin	O_2 storage	Animals	One *heme*
	Cytochromes	Electron transfer	Bacteria, plants, animals	Four *hemes*
Non-*heme*	Transferrin	Fe transport	Animals	Two
	Ferritin	Fe storage	Animals	20 wt% Fe
	Ferredoxins	Electron transfer	Bacteria, plants, animals	Two to eight
	Rubredoxins	Diverse	Bacteria	One

Iron-sulphur centres can be sub-grouped into four types of site: rubredoxin (Rb) [Fe(S-Cys)$_4$], and three different sites for the ferredoxin (Fd) proteins based on the number of

iron atom in the centres. [21-23] The oxidation states of iron in these clusters are Fe(II) and/or Fe(III) in approximately tetrahedral FeS_4 coordination unit.

2.1.1 Rubredoxins (Rb)

Rubredoxins are proteins known as those containing only one iron atom. They participate in a number of biological reactions in anaerobic bacteria, for instance as electron carrier in oxygen detoxifying pathway. Four S atoms belonging to cysteine residues in the protein chains coordinate the single iron atom from rubredoxin, **Figure2.1**. It has a high-spin configuration in a high-spin state, in a tetrahedral environment based on spectroscopic studies.

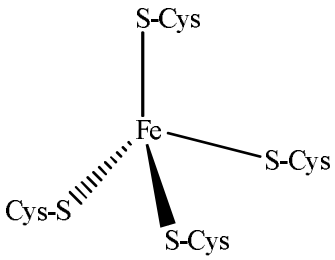

Figure 2.1. Rubredoxin.

Rubredoxin iron differs from the other iron-sulphur cluster proteins in having no labile sulphur, S^{2-} (so called inorganic sulphur) from which hydrogen sulphide, H_2S can be generated by treatment with mineral acid.

The reduced form of the protein is colourless, but when it in its oxidised state, an intense red colour is observed resulting from a ligand-to-metal charge transfer transition (LMCT) from the σ- and π-orbitals of thiolate ligands (electron-rich) to the oxidised ferric Fe(III) (electron-poor). This observation highlights the strong electronic interaction between iron and sulphur which will induce specific spectroscopic and

redox properties in all the different Fe-S centres. The reduction potentials for rubredoxins are generally between -50 and +50 mV (*vs*. standard hydrogen electrode, SHE).

2.1.2 Ferredoxins (Fd)

Iron-sulphur proteins possessing inorganic sulphur are commonly designated as ferredoxins. These are found in living systems such as green plants (including algae), photosynthetic bacteria, protozoa and some fermentative anaerobic bacteria. Their redox potential can be as low as -700 mV *versus* SHE which makes them good reducing agents for biochemical processes. There are three different classes of ferredoxins based on the number of iron which are rhombic $[Fe_2S_2(S\text{-}Cys)_4]$, cuboidal $[Fe_3S_4(S\text{-}Cys)_3]$ and cubane $[Fe_4S_4(S\text{-}Cys)_4]$.

2.1.2.1 {2Fe-2S} centres (Two-Iron ferredoxin)

This type of proteins has the peculiarity of possessing in the metal centre two inorganic sulphurs bridging two irons. The $\{Fe_2S_2\}$ centres are anchored to the protein by the coordination of four cysteines from the backbone of the protein (**Figure 2.2**).

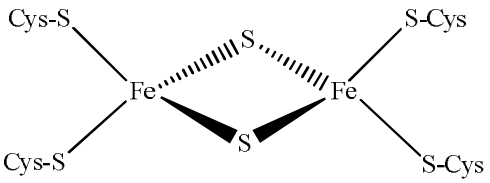

Figure 2.2. {2Fe-2S} ferredoxin.

The two biologically relevant oxidation states are the oxidised form Fd_{ox} $\{Fe_2S_2\}^{2+}$ [Fe(III)-Fe(III)] and the mixed valence form Fd_{red} $\{Fe_2S_2\}^{+}$ [Fe(II)-Fe(III)]. The one electron transfer reaction by the protein involves the reduction of Fd_{ox} to Fd_{red}.

Reduction potentials for $\{Fe_2S_2\}$ centres are generally between -450 and -150 mV (*vs.* SHE). Some unusual redox potentials have been observed in so-called "Rieske centres", showing uncommon spectroscopic properties and relatively high redox potentials (-100 to +400 mV). These properties are assigned to the asymmetrical coordination involving two histidines instead of two cysteines $\{(Cys)_2Fe(\mu\text{-}S)_2Fe(His)_2\}$.

2.1.2.2 {3Fe-4S} centres (Three-Iron ferredoxin)

Figure 2.3 shows the {3Fe-4S} ferredoxin. This cuboidal structure (*i.e.* a cube with one vacancy) has been found in several Fe-S proteins as well as in the inactive form of the enzyme aconitase (aconitase hydratase/isomerise). It is also present as a cofactor in the [NiFe]-hydrogenase to transfer electrons after dihydrogen oxidation.

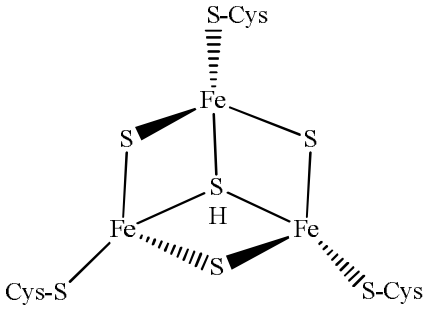

Figure 2.3. {3Fe-4S} ferredoxin.

The reduction potentials of the couple $\{Fe_3S_4\}^+/\{Fe_3S_4\}^0$ are variable, ranging from -425 mV in *Azobacter vinelandii* ferredoxin I to -70 mV in *Desulfovibrio gigas* [NiFe]-hydrogenase (*vs*. SHE), and exhibit substantial pH dependence.

2.1.2.3 {4Fe-4S} centres (Four-Iron ferredoxin)

The most common iron-sulphur centre in biology is the {4Fe-4S} type. Four cysteines from the polypeptide chain anchor the cubane to the protein (**Figure 2.4**).

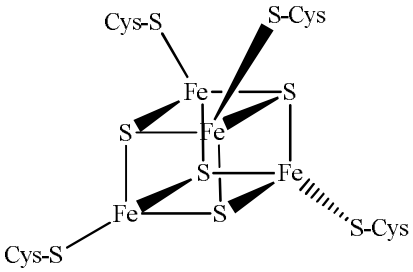

Figure 2.4. {4Fe-4S} ferredoxin.

These types of Fe-S centre exhibit three possible oxidation states, $\{Fe_4S_4\}^{3+}$, $\{Fe_4S_4\}^{2+}$ and $\{Fe_4S_4\}^{+}$, but they have not been observed in any proteins unless its tertiary structure is significantly disturbed. Like the {2Fe-2S} ferredoxin, the cluster acts as a one-electron transfer agent and depending on their redox behaviour. The ferredoxin proteins can therefore be divided into two subclasses: Fd using the $\{Fe_4S_4\}^{2+}/\{Fe_4S_4\}^{+}$ redox couple (-700 to -300 mV *vs.* SHE) and Fd proteins that can sustain a higher oxidation state using $\{Fe_4S_4\}^{3+}/\{Fe_4S_4\}^{2+}$ redox couple (+100 to +400 mV *vs.* SHE) and called HiPIP (high potential iron protein) (**Scheme 2.1**). These potentials are also pH-, ionic strength- and temperature-dependent.

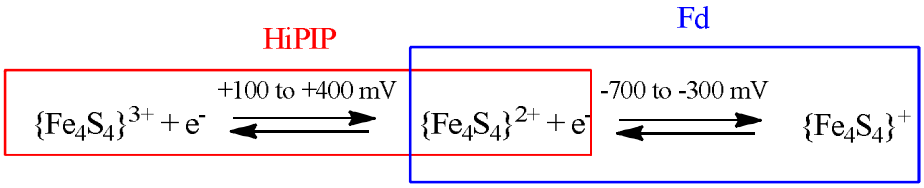

Scheme 2.1. Redox potentials for HiPIP and ferredoxin proteins.

Such differences in redox potentials between Fe-S clusters in Fd and HiPIP are not due to their structures, as they appear to be nearly identical, but to the cluster environment. Crystallographic data indicate that in Fd, the Fe-S centre is very close to the protein surface compared to the more buried Fe-S centre in HiPIP. This indicates that the accessibility of the cluster to aqueous solvent and potential hydrogen bonding interaction is easier for Fd, whereas the environment is more rigid for HiPIP.

2.2 Hydrogenases

Hydrogenases have the ability to control molecular hydrogen, H_2, concentration and reduction activity by facilitating the uptake and the oxidation of H_2 to protons with release of electrons; or its production, [24, 25] according to the reverse reaction (**Equation2.1**). The reversible oxidation of H_2 provides electrons at a low potential ($H_2/2H^+$: E^o = -414 mV at pH 7 and 1 atm of H_2 *versus* standard hydrogen electrode, SHE), [26] nevertheless H_2 activation is energetically unfavourable due to the low acidity of the H-H bond (p*Ka* = 35).

$$2H^+ + 2e^- \leftrightarrow H_2 \qquad \textbf{(Equation 2.1)}$$

The hydrogenase enzyme was named by Stephenson and Stickland in 1931 when they demonstrated that colon bacteria could evolve and use H_2 to reduce substrates. [27]

In 1956, the understanding of this class of enzyme changed substantially when the presence of non-*heme* iron was confirmed. [28] On the basis of electron paramagnetic resonance, EPR studies, it was agreed that hydrogenases contained iron-sulphur clusters of HiPIP ferredoxin type, [29-31] but it was not until the early 1980s that nickel was also detected in some hydrogenases. [32]

The mid 1980s classified the ambiguity surrounding the nickel and iron content. In fact, at this time it became clear that hydrogenases could be divided in two principal classes, those that contain only iron, [FeFe] and those that also contain nickel, [NiFe]. A third class which is the iron-sulphur cluster-free hydrogenase (now abbreviated as [Fe]-hydrogenase or H_2-forming methylenetetrahydromethanopterin dehydrogenase, Hmd), initially was thought to incorporate no metal centre, was discovered about 20 years ago in methanogenic archaea. [33, 34] There is a minor group of hydrogenase, [NiFeSe]-hydrogenase principally found in methanogenic organisms which is responsible for oxidation of dihydrogen. [35] It was suggested that [NiFeSe]-hydrogenases in general are less sensitive to oxygen attack compared than the other metallic hydrogenases. Classes of hydrogenases are summarised in **Table 2.2**.

Table 2.2. Classification of hydrogenases.

Classification	Source	Structure	Localisation	Major function
[NiFe]-hydrogenase	Anaerobic, photosynthetic bacteria, cyanobacteria	Heterodimeric, multimeric	Cytoplasmic, periplasmic	Dihydrogen uptake
[FeFe]-hydrogenase	Green algae, photosynthetic bacteria, cyanobacteria, protozoan	Monomeric, heteromeric	Cytoplasmic, periplasmic, chloroplast	Dihydrogen production
[Fe]-hydrogenase	Methanogens	Monomeric	Cytoplasmic	Formation of dihydrogen
[NiFeSe]-hydrogenase	Sulphate-reducing bacteria, methanogens	Oligomeric	Cytoplasmic	Oxidation of molecular hydrogen

The vast majority of known hydrogenases belong to the first two classes and over 100 of these enzymes have been characterised genetically and/or biochemically. [12, 13]

Although most hydrogenases can catalyse proton reduction (**Table 2.3**) in either direction in *vitro*, they usually catalyse either molecular hydrogen uptake or evolution in *vivo*. [9]

Table 2.3. Catalytic activities (measured as molecules of dihydrogen per second per hydrogenase molecule at 30 °C) of purified [NiFe]- and [FeFe]-hydrogenases. [9]

	[NiFe]-hydrogenase	**[FeFe]-hydrogenase**
H_2 production	700	6000-9000
H_2 consumption	700	28000

Figure 2.5 shows a functional scheme of a hydrogenase enzyme. In both [NiFe]- and [FeFe]-hydrogenases, flow of electron to the active site is transmitted over a different path and the most common way is through electron hopping along the classic {4Fe-4S} cubane clusters.

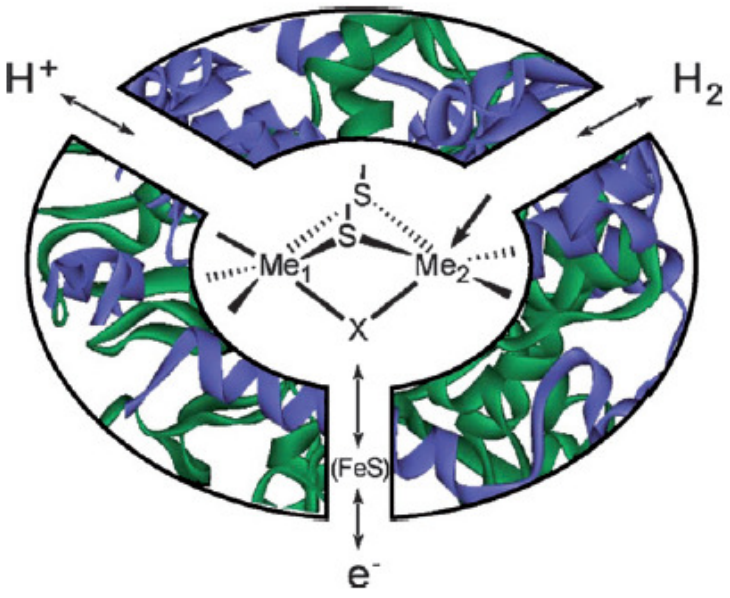

Figure 2.5. Schematic representation of hydrogenase showing the S-bridged bimetallic catalytic centre, the proton and hydrogen channels together with the electron transfer chain. Arrow on the metal, Me_2 indicates the coordination site (adapted from ref. [36]).

2.2.1 [Fe]-hydrogenase

H_2-forming methylenetetrahydromethanopterin dehydrogenase (Hmd), also abbreviated as [Fe]-hydrogenase is an enzyme discovered about 20 years ago in *Methanothermobacter marburgensis* which is mainly found in methanogenic archaea. Previously, this enzyme was referred to as metal free hydrogenase, later it was discussed that it contains a single Fe atom. It also sometimes referred to as iron-sulphur cluster-free hydrogenase to highlight an important structural difference with the [FeFe]- and [NiFe]-hydrogenases. Presence of iron is essential for the activation of H_2 and therefore Hmd is not a metal free hydrogenase as previously proposed. [37, 38] Hmd contains two irons and no acid labile sulphur in its homo dimer. Hmd catalyses the reversible reduction of methylenyltetrahydromethanopterin (methylenyl-H_4MPT$^+$) with dihydrogen to methylenetetrahydromethanopterin (methylene-H_4MPT) and a proton. [33, 34] A hydride is stereospecifically transferred from H_2 to the *pro-R* site of methylene-H_4MPT (**Scheme 2.2**). Hmd does not catalyse H_2/H^+ exchange in the absence of methylenyl-H_4MPT$^+$.

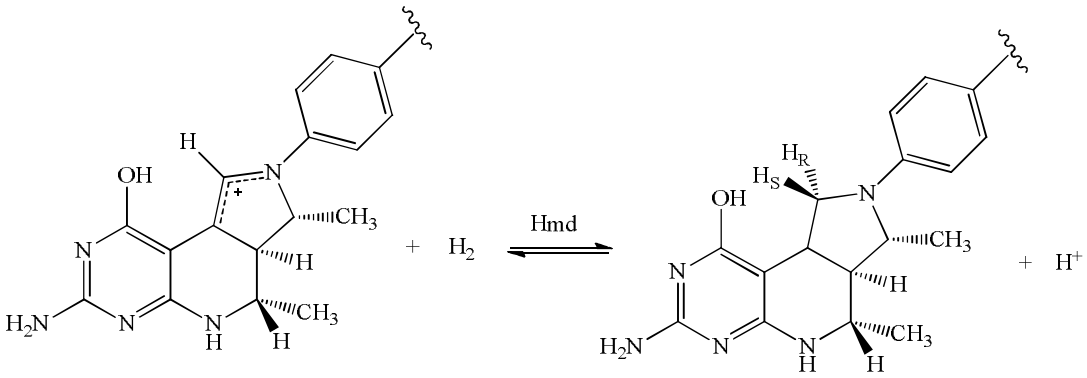

Scheme 2.2. Reversible reaction catalysed by Hmd. [33, 34]

To date, crystal structure of active Hmd has yet been obtained, but in exceptional work by Shima and his co-workers, they manage to obtain the X-ray structure of an active enzyme reconstitution from *Methanothermobacter jannaschii* apoenzyme with iron cofactor from *Methanothermobacter marburgensis.* [39] In this structure (**Figure 2.6**), iron which is EPR-silent is coordinated to the pyridine derivative. The oxidation state of this iron is most probably Fe(0) or Fe(II) low-spin as suggested by Mössbauer spectroscopy. [40] Infrared spectroscopy showed the presence of two carbonyl ligands coordinated to the iron, together with thiolate sulphur. The nature of fifth ligand is unknown as its electron density cannot assign definitely as monatomic or diatomic ligand. The sixth ligand is more to a vacant site of the iron, which Shima and his co-workers interpret as monatomic solvent (water) molecule, but the possibility of another CO group on the same position cannot be ruled out. [41]

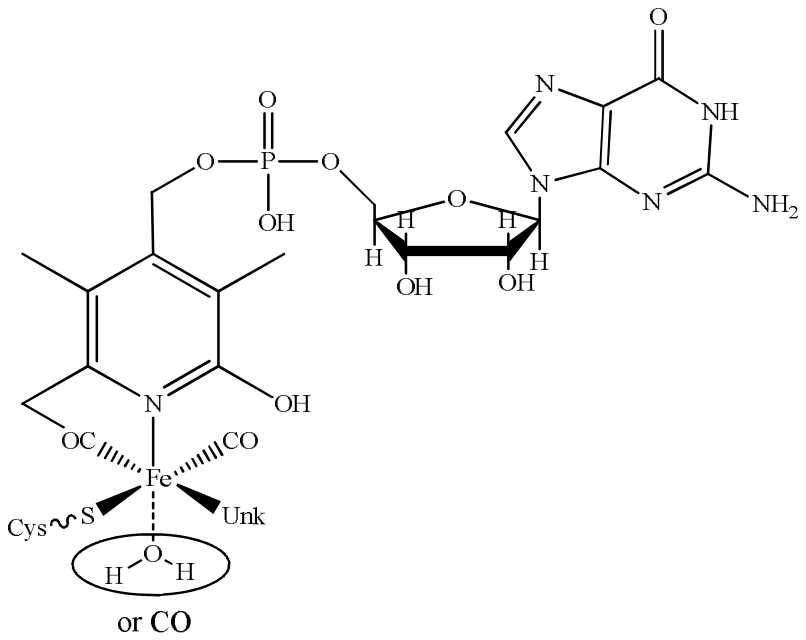

Figure 2.6. Schematic representation of the active site of Hmd. Unk, unknown ligand; this site appears to bind cyanide.[39, 41]

2.2.2 [NiFe]-hydrogenase

[NiFe]-hydrogenases have been the subject of extensive research [42-44] and were the first hydrogenases to be studied by X-ray diffraction methods. The X-ray structure of [NiFe]-hydrogenase from *Desulfovibrio gigas* was solved at 2.85 Å resolution in 1995 [44] and demonstrated clear evidence concerning the type and spatial arrangement of iron-sulphur (FeS) clusters within the protein and also allowed a picture of the active site structure for the first time. As isolated, the enzyme is a heterodimeric periplasmic protein consisting of two sub-units: one large (60 kDa) and one small (20 kDa). The X-ray structures of [NiFe]-hydrogenases depicted in **Figure 2.7** have revealed a bimetallic nickel-iron centre at the active site, located in the large subunit and buried inside the protein. The protein contains a total of 12 iron atoms, 12 acid labile sulphides and one nickel atom. 11 of the 12 Fe atom are incorporated within the three iron-sulphur cluster, one $\{3Fe\text{-}4S\}^{+1/0}$ and two $\{4Fe\text{-}4S\}^{2+/+}$ moieties. [44] The Ni in the active site centre is ligated by four cysteinates, two of which are terminal, and two of them bridge to Fe. The Fe centre is ligated further by three non-protein diatomic ligand (cyanide and carbon monoxide), with a third bridging ligand that has been assigned to oxo-oxygen. It is rarely observed in biological systems since the cyanide and the monoxide are normally associated with inhibition and poisoning, but in this case, they can stabilise the low-oxidation stage of the iron (+2, diamagnetic). Hydrophobic channels have been identified by crystallographic analysis of xenon binding and these channels permit the diffusion of H_2 within the interior of the enzyme. [45]

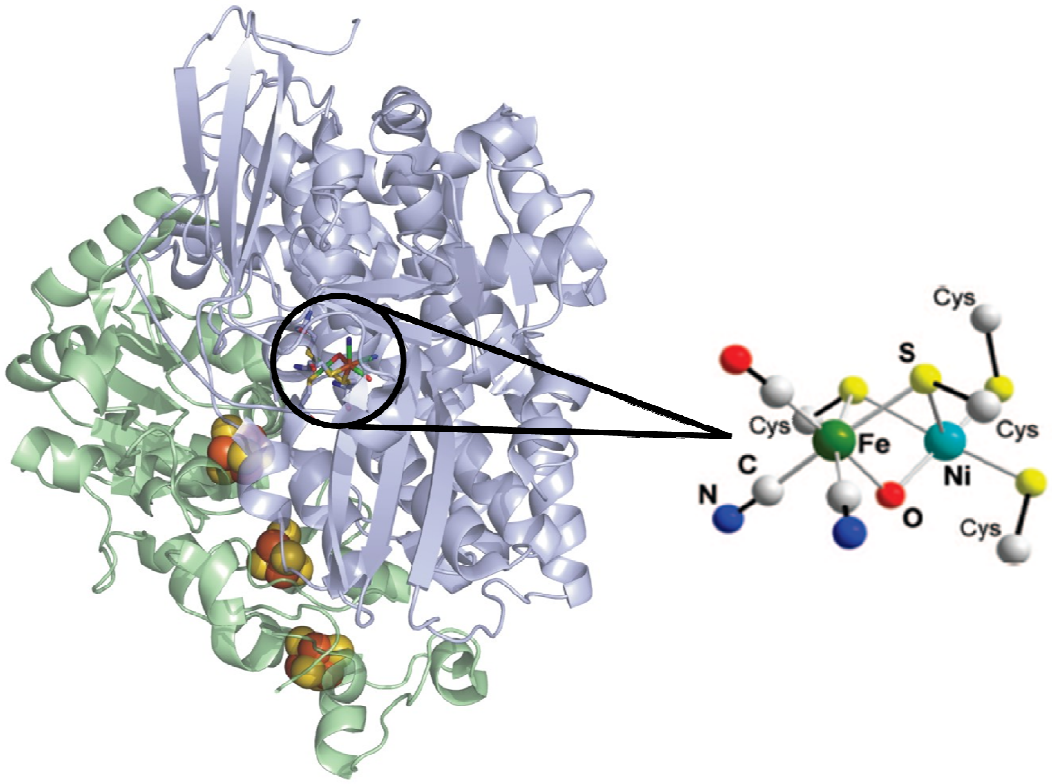

Figure 2.7. Crystal structure on active site of [NiFe]-hydrogenase isolated from *Desulfovibrio gigas*. [46]

Prior to the X-ray structure showing that the active site of the [NiFe]-hydrogenase was comprised of a nickel and an iron connected by bridging thiolates, it was believed nickel provided the catalytic centre and undergoes several oxidation state changes (+1, +2, +3) whereas the iron centre remains Fe(II) during the catalytic cycle and is only involved as a constituent of the iron-sulphur cluster electron transfer relay.

2.2.3 [FeFe]-hydrogenase

[FeFe]-hydrogenase enzymes have been especially difficult to study due to their high sensitivity to oxygen. Nevertheless, two X-ray crystallographic data of [FeFe]-hydrogenases from *Desulfovibrio desulfuricans* (Ddh) and *Clostridium pasteurianum*

(Cp1) have been solved at 1.8 and 1.6 Å resolution respectively. [47, 48] Molecular masses of hydrogenases can vary from 45 to 130 kDa. Unlike [NiFe]-hydrogenases, [FeFe]-hydrogenases are mainly monomeric (in the cytoplasm), but dimeric, trimeric and tetrameric enzymes are also known (in the periplasm).

The heterodimeric periplasmic hydrogenase from Ddh is comprised of a small and a large subunit of 11 and 42 KDa. The active site is buried in the molecule and is interacting with a ferredoxin type domain containing two {4Fe-4S} clusters. No other iron-sulphur clusters are observed in DdH. For Cp1, the monomeric cytoplasmic hydrogenase is comprised of four non-overlapping domains. The largest domain contains the active site while the three remaining domains all contain iron-sulphur clusters of ferredoxin type. The closest to the active site is comprised of two {4Fe-4S} clusters and away from the latter are positioned two domains with one containing a {4Fe-4S} cluster and the other containing a {2Fe-2S} cluster.

2.2.3.1 The active site: H-cluster

Prior to the publication of crystal structures of Cp1 and DdH, together with the spectroscopic data on [FeFe]-hydrogenase from *Desulfovibrio vulgaris*, [49] active site at which protons are reduced to dihydrogen (or dihydrogen oxidised to protons) can be viewed as a six iron (6Fe) cluster. This active site or H-cluster is perhaps the most remarkable feature of this hydrogenase. H-cluster is buried deeply within the protein and a continuous hydrophobic channel has been observed between the surface and the active site, and is conserved in the two [FeFe]-hydrogenases (Cp1 and DdH) studied to date. As these enzymes are involved in different reactions (dihydrogen uptake for DdH and dihydrogen evolution for Cp1), it suggests that the same pathway is used by dihydrogen to access or exit the active site.

The H-cluster is composed of an {4Fe-4S} cluster linked by a cysteinyl residue to a {2Fe-2S} sub-site as displayed in **Figure 2.8**. The {4Fe-4S} cluster is anchored to the protein by three cysteines from the backbone of the protein. The {4Fe-4S} cluster plays the role of electron donor in the catalytic process.

On the diiron sub-site, each of the Fe atoms is bound to terminal carbon monoxide (CO) and terminal cyanide (CN^-) ligand. The binuclear metal centre is bridged by a dithiolate ligand, possibly 1,3-propanedithiolate, di(thiomethyl)amine or di(thiomethyl)oxo. The amino bridge is favoured by the possibility of hydrogen bonding with amino acids from the protein and also proton transfer to the active site, but no clear X-ray data has so far allowed discrimination between CH_2, NH or O. However the hyperfine sublevel correlation spectroscopy (HYSCORE) and electron nuclear double resonance (ENDOR) data from the Lubitz's group strongly indicates the binding ligand is di(thiomethyl)amine. [50]

Despite obvious structural similarities, the two active sites from Cp1 and DdH have some differences in their {2Fe-2S} sub-site that can result from at least two factors. Firstly, the resolution at which the X-ray crystal structures have been solved (dependent on the crystal quality) and secondly, the experimental conditions from which the crystals have been grown.

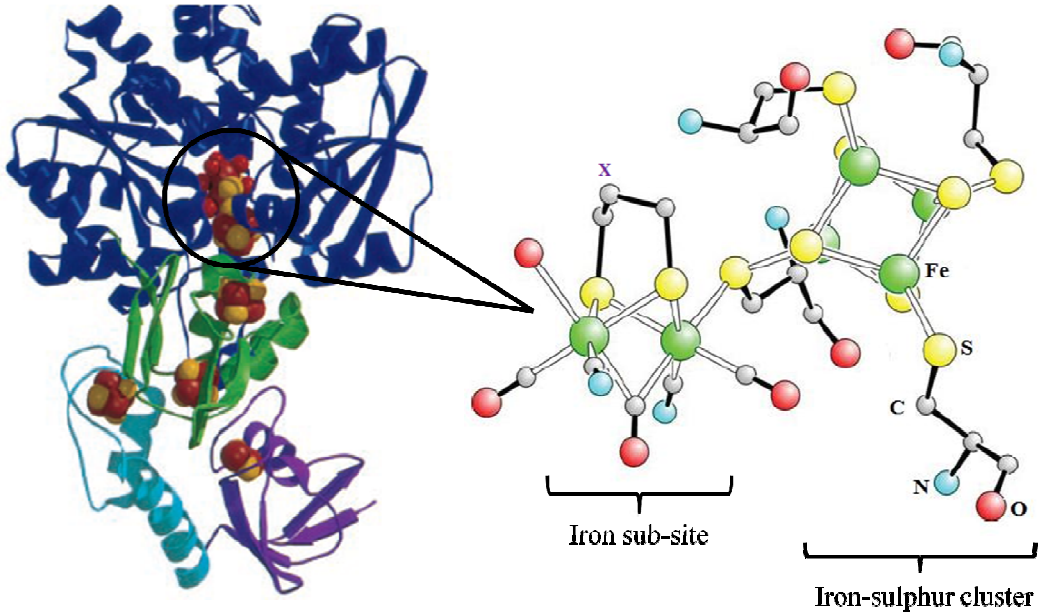

Figure 2.8. Composite structure of H-cluster constructed from crystal structure of [FeFe]-hydrogenase active site from Ddh, [47] Cp1 [48] and FTIR data of *Desulfovibrio vulgaris*. [36] The apical group on the sub-site ligand, X may possibly be CH_2, NH or O.

For Cp1, biologically unusual terminal CO and CN^- ligands coordinate the two irons and together with a bridging carbonyl. Early infrared studies by Albracht and co-workers [51] on [FeFe]-hydrogenase from *Desulfovibrio vulgaris* showed intense features in the 2100-1800 cm^{-1} region typical for chemical groups such as metal-coordinated CO and CN^-. Later studies by the same group suggested that a bridging CO is present in the oxidised state but absent when the enzyme is reduced, due to the observation of a broad intense infrared band at 1811 cm^{-1}. [52] CO has been shown to be a competitive inhibitor for hydrogen activation and induces changes in both the EPR [52] and infrared spectra in the H-cluster. The additional CO binds to the distal iron replacing water (or occupied) the vacant site on the distal iron.

2.2.3.2 The nature of the sub-site

The diiron sub-site which forms part of the active site of [FeFe]-hydrogenase is able to acquire several stable structures, either catalytically active or inactive, within a relatively narrow range of redox potentials. This functional property is probably due to the combination of different types of ligands that coordinate to the iron metals: thiolates (good π-donors), cyanides (good σ-donors), and carbonyls (good π-acceptors). Their special coordination may act as an electronic buffer that facilitates the entry and exit of electrons in the active site.

From the structural viewpoint, the most controversial differences surround the nature of the dithiolato unit by which the two iron atoms are bridged. In both cases (Cp1 and Ddh), this bridging unit is biologically unprecedented. In Cp1, it consists of one atom, X on **Figure 2.9(a)** (with X = C, N or O) covalently bound to the two sulphur atoms, whereas in DdH, this moiety is comprised of three atoms that were first assigned as carbon atoms to give the chemically known 1,3-propanedithiolate moiety, **Figure 2.9(b)**. Later on, it was noted that the X-ray crystallographic studies on both Cp1 and DdH were not able to give more details about the exact nature of this dithiolate unit in the electron density map. [5, 53, 54] Observations on DdH showed a hydrogen bonding mode between the central atom of the dithiolato unit and a proximal cysteine from the protein backbone. With respect to hydrogen bonding mode, the most probable nature of this central atom is nitrogen as claimed by Fontecilla-Camps and co-workers. [55] Hall and co-workers have also reported that a di(thiolatomethyl)amine ligand at the sub-site would provide a low energy barrier for H_2 formation-cleavage. [56] Yet, the truth as to whether the natural system possess CH_2, NH or O bridgeheads was still unresolved up until the middle of year 2009, when Lubitz and co workers [50] presented strong evidence

based on combination studies of HYSCORE, EPR and ENDOR measurements where they demonstrated the first experimental evidence for the presence of NH bridgeheads.

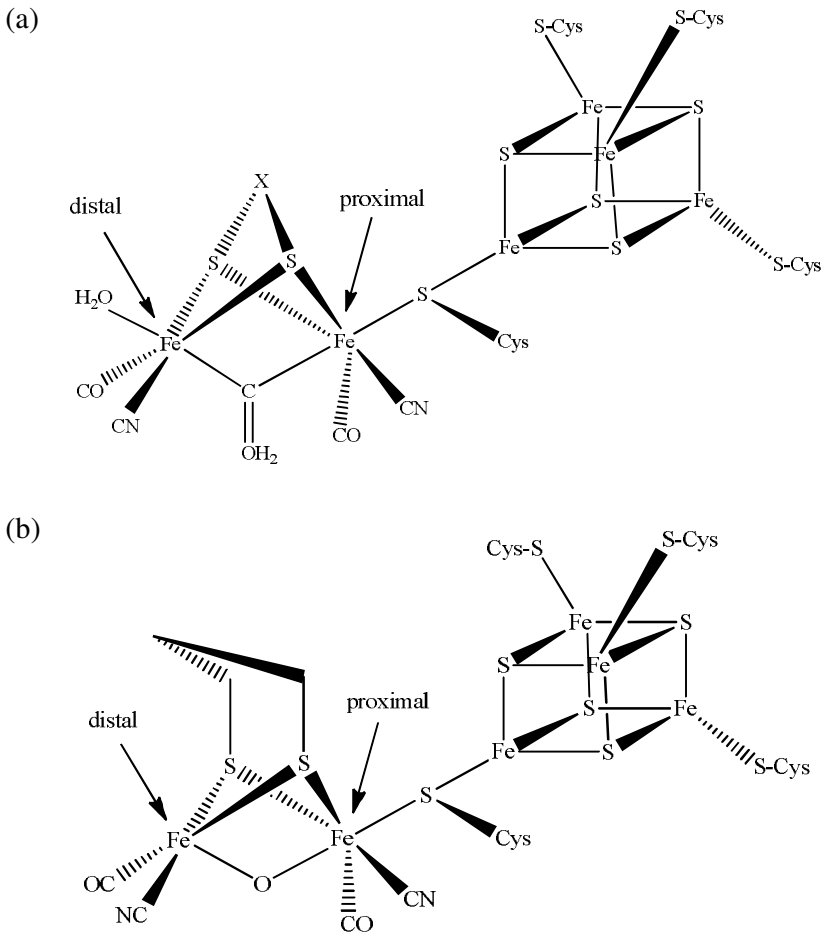

Figure 2.9. (a) Proposed active site of [FeFe]-hydrogenase, as isolated from (a) Cp1 [48] and (b) Ddh. [47]

In contrast with the unsaturated sub-site of DdH, the distal iron (far from the {4Fe-4S} cluster, as opposed to the proximal iron which is on the other end close to the cluster) of the sub-site in Cp1 binds with a water molecule. The absence of this weak ligand in DdH suggests that this vacant site might be involved in catalysis, possibly acting as a binding site for a hydride or a dihydrogen molecule. It has been shown by

crystallography [57] and infrared that instead of a water molecule, this iron can bind an additional CO molecule when the enzyme is incubated under a CO atmosphere. Under these conditions, the enzyme is fully inhibited and it is clear from this experiment that the distal iron must be highly implicated in the substrate bonding at the H-cluster.

2.2.3.3 Proposed catalytic mechanism

The catalytic mechanism of [FeFe]-hydrogenase is not completely understood with key steps remaining speculative such as the binding site for dihydrogen, the formation or not the bridging hydride or other terminal hydride, the location of the proton donor/transfer site(s) such as NH^-, CN^-, S^- or electron transfer mechanism from the {4Fe-4S} cluster to the {2Fe-2S} sub-site are the main questions which still have to be resolved. [58, 59] One working model for the mechanism of [FeFe]-hydrogense is shown in **Scheme 2.3**. This draws upon DFT biological and chemical knowledge of the hydrogenase reaction. [60]

Here we consider the possibility of di(thiolatomethyl)amine ligand as the bridging connected the bimetallic of sub-site. In particular, the occurrence of nitrogen would be of mechanistic relevance since the central atom could act as proton acceptor/donor in the dihydrogen oxidation/reduction reaction. In the active site of [FeFe]-hydrogenase, one of the intrinsic CO ligands switches between terminal and bridging positions, depending on the redox state of the enzyme. The first steps in the enzyme activation involve the introduction of proton into the {2Fe-2S} di(thiolatomethyl)amine ligand (coming from the $\{Fe_4S_4\}$ cluster). The binding of active site iron to the high field, π-acceptor CO and CN^- ligands promotes a low redox state of the metal ion, making it a relatively soft Lewis acid. This, in turn, favours its binding to the soft Lewis base H^-, a probable step in catalysis and combined with the proton from the di(thiolatomethyl)

amine at the sub-site. The two hydrogen atoms are then bonded together and lead to formation of dihydrogen which is ejected from the molecule. The CO and CN^- ligands in the crystal structure have assigned making use of FTIR data as well as taking into account the possibility for hydrogen bonding of the CN^- groups to nearby amino acid residues. After addition of a new electron, the cycle is back to its H_{ox} inactive state.

Notable, such a structure has inspired organometallic chemists to find out whether it was possible to build synthetic molecules, based on those abundant elements on the planet such as sulphur, iron, carbon monoxide and cyanide, having the same efficiency as that of the enzyme. These synthetic models were proposed in view of getting a better understanding of the chemistry of the active diiron sub-site and the minimal structural requirements for hydrogenase activity to provide alternative electrocatalysts for efficient molecular hydrogen production.

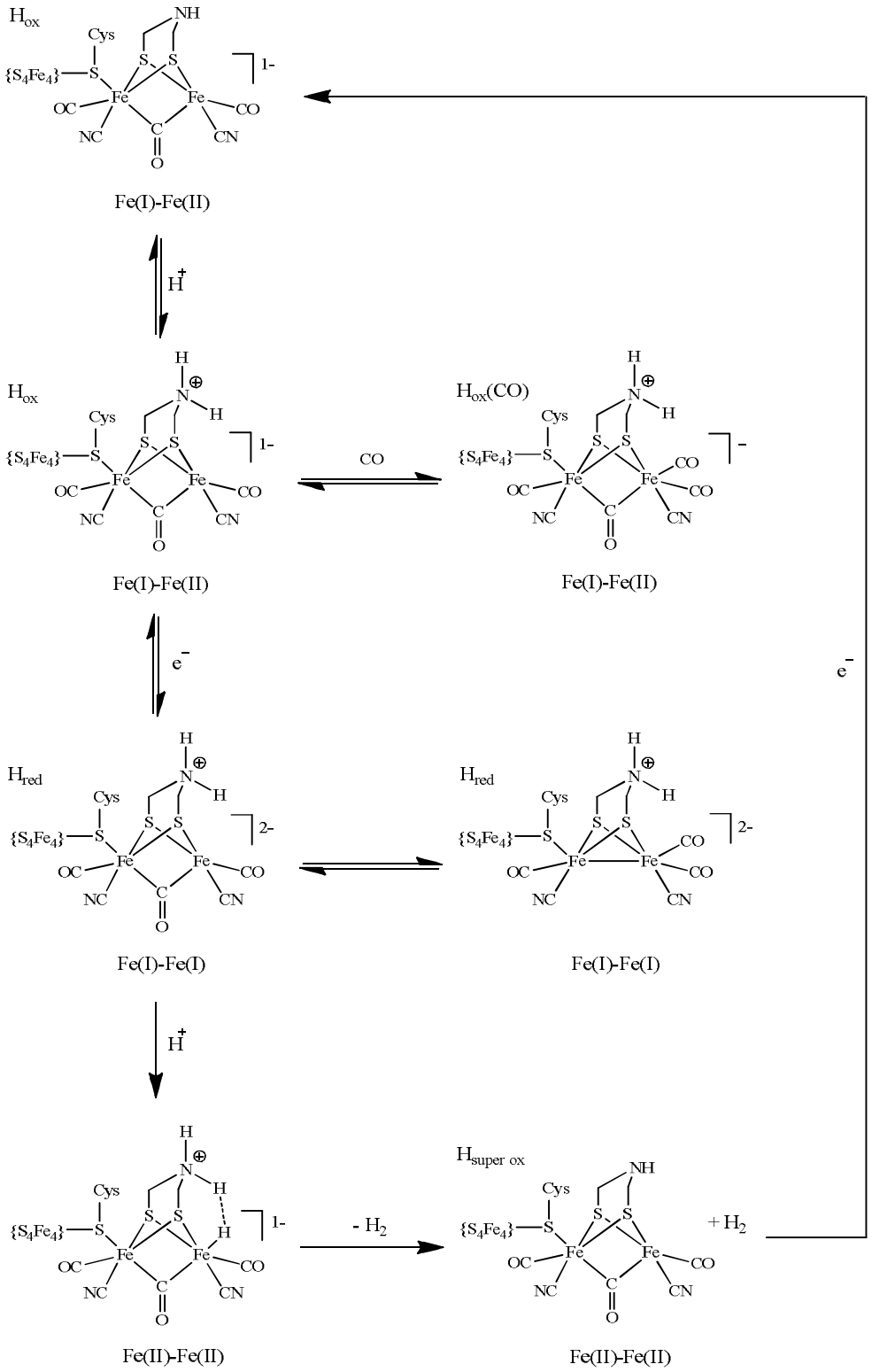

Scheme 2.3. Catalytic cycle of the production/oxidation of H_2 as presented by Fontecilla-Camps and her respective co-workers [60] (electrons/protons are provided by the {4Fe-4S} cluster; {4Fe-4S} cluster has been shown experimentally to be charged 2+).

2.2.4 Synthetic models related to the [FeFe]-hydrogenase

Iron-sulphur clusters are involved in the electron to the active site and the H-cluster itself is comprised of an $\{Fe_4S_4\}$ cluster and sub-site as discussed earlier in the chapter. Here we outlined some of the earlier synthetic studies on iron-sulphur cluster and more recent studies on sub-site analogues processing CO and CN^- or other donor groups.

2.2.4.1 Synthetic analogues of iron-sulphur cluster

Iron-sulphur clusters have a remarkable facility for conversion and interconversion in both the free and protein-bound conditions, supporting the concept that they are modular structures. They also undergo ligand exchange reactions and oxidative degradation, both of which are biologically significant. [61] The synthesis of iron-sulphur active site was initiated in the early 1970s following X-ray structural determination of iron-sulphur proteins. [62] These complexes, available in highly pure and crystalline form, were the beginning of what is now bioinorganic chemistry. The first analogue was a model of {4Fe-4S} centres, a cubane-type structure $[Fe_4S_4(SCH_2Ph)_4]^{2-}$. [63] The complex was simply prepared from ferric chloride, sodium methoxide, sodium hydrosulphide and appropriate alkyl mercaptan. The {4Fe-4S} core is a distorted cube, with iron-sulphur atoms at alternate vertices and is closely related to active site structures of HiPIP and ferredoxin proteins.

From the first rubredoxin analogues $[Fe(SR)_4]^{2-}$ synthesised in 1975 [64] to cuboidal $[Fe_3S_4(SR)_3]^{3-}$ in 1995, [65] the chemistry of iron-sulphur complexes has been extensively studied and led to a better comprehension of these type of assemblies and their electronic properties (**Scheme 2.4**). [62]

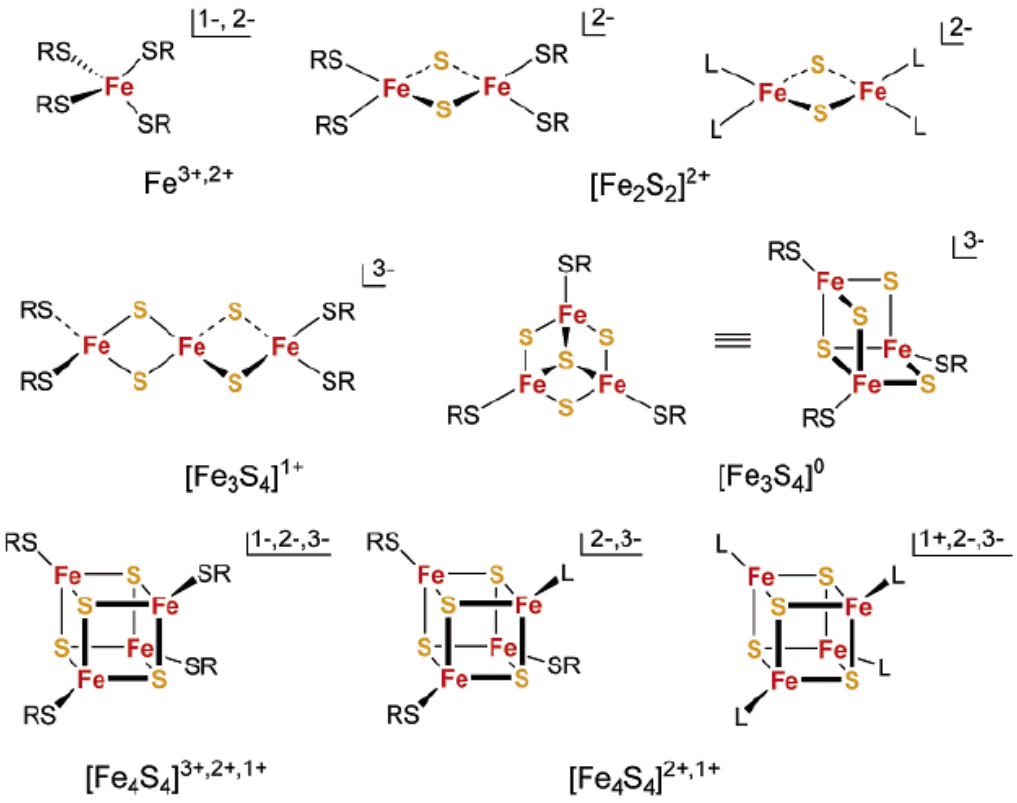

Scheme 2.4. Synthetic analogues of protein sites containing one, two, three and four iron atoms. Known oxidation states in isolated compounds are indicated. L = RO^-, halide, or neutral or a mono anion (adapted from ref. [62]).

The synthesis of the {4Fe-4S} cubane type received more attention than any other analogue. The term cubane type includes all $\{Fe_4S_4\}$ cores made up of six edge-shared non-planar $\{Fe_2S_2\}$ rhombuses, regardless the symmetry distortion. Over 70 homoleptic thiolate clusters of $\{Fe_4S_4(SR)_4\}^{n-}$ (n = 1, 2, 3) were synthesised, whereas more than 30 site-differentiated clusters with variant L ligands have been isolated or generated in solution, for example the clusters with halide ligands which are valuable starting materials for preparation of thiolate clusters. [66-69] The crystal structures of some 37 clusters of this type have been determined, including instances of the same cluster with

different counter ions. Aspects on the synthesis of these cubane clusters will be developed further in **Chapter 3**.

The protein bound {4Fe-4S} cubane is best known for its function in electron transfer. The protein structural and its environmental play a key role in determining the relative potential of each $\{Fe_4S_4\}$ species as indicated in **Scheme 2.5**.

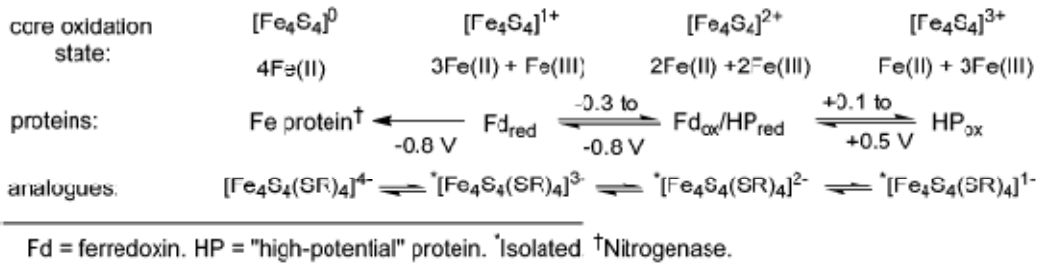

Scheme 2.5. Electron transfer series of $\{Fe_4S_4\}$ protein sites for $\{Fe_4S_4(SCys)_4\}$and analogues $\{Fe_4S_4(SR)_4\}$showing core oxidation states and formal iron valence states. Isoelectronic species are arranged vertically, potential indicated referred to SHE (taken from ref. [62]).

Two types of one electron redox behaviour were recognised which are conversion between oxidised and reduced ferredoxins with mid-point potentials near -0.40 V and between oxidised and reduced high potential (HP) proteins with mid-point potentials near to +0.3 V (*vs*. SHE) as previously described in **Section 2.1.2.3**. The overall charges in the series directly give information on the core oxidation state and mixed valence composition of each member. It is to be noted that significant variation of potentials can occur in native and mutated proteins [70, 71] and even for two clusters in the same protein. [72]

The $\{Fe_4S_4\}^{3+}$ oxidation state was first detected electrochemically by oxidation of $[Fe_4S_4(SBu^t)_4]^{2-}$ and is isoelectronic with the HP_{ox}, [73] where potential is positive (> +0.1 V *vs.* SCE). Oxidation state of $\{Fe_4S_4\}^{2+}$ is isoelectronic with Fd_{ox} and HP_{red} which makes its potential around -0.3 to -0.8 V *vs.* SCE, whereas potential of $\{Fe_4S_4\}^{+}$ is at the range -0.8 V (*vs.* SCE), which isoelectronic with Fd_{red}. This complex is conventionally prepared through reduction of $[Fe_4S_4(SR)_4]^{2-}$ with reducing agents such as sodium acenaphthylenide radical anion. [74, 75] Last but not least, the oxidation state of $\{Fe_4S_4\}^{0}$ was first detected in electrochemistry in aprotic solvents for the couple $[Fe_4S_4(SR)_4]^{3-/4-}$ with $E_{1/2}$ ligands < -1.7 V *versus* SCE. [73, 74] More recently a stabilised $\{Fe_4S_4\}^{0}$ core was synthesised using CN^- by Scott *et al.* [76] through treatment of the cyanide cluster $[Fe_4S_4(CN)_4]^{3-}$ [77] with $K[Ph_2CO]$ in MeCN/THF. Enzymatically, this $\{Fe_4S_4\}^{0}$ state has been generated in the Fe protein of *Azotobacter vinelandii* nitrogenase upon reaction with a strong reductant, Ti(III) citrate, although it is unclear whether or not it has a physiological role. [78, 79]

2.2.4.2 Synthetic models of the diiron sub-site

a) Early {2Fe-2S} complexes

In 1929, Reihlen *et al.* described the synthesis of $Fe_2(CO)_6(SEt)_2$ (**Scheme 2.6**). [80] However, no analytical methods available at this time could confirm the structure.

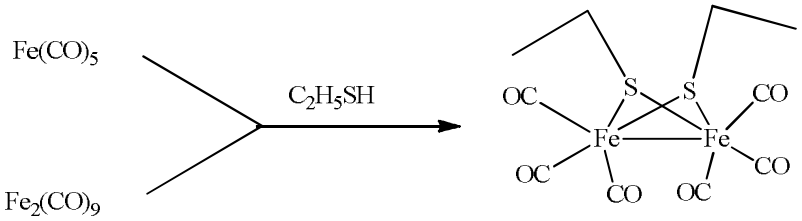

Scheme 2.6. Synthesis of $Fe_2(CO)_6(SEt)_2$. [80]

A similar compound, $Fe_2S_2(CO)_6$ was identified using X-ray diffraction by Dahl and his co-worker [81] (**Figure 2.10**) where they showed the complex is butterfly-shaped (distorted Fe_2S_2 tetrahedron) with a bent metal-metal bond. This volatile $Fe_2S_2(CO)_6$ complex was first identified as an intermediate of a reaction producing $Fe_3S_2(CO)_9$ and another iron carbonyl chalcogenide by Hieber and Gruber. [82]

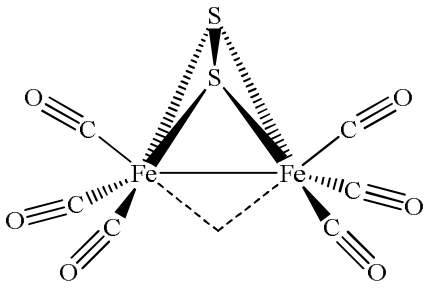

Figure 2.10. Schematic representation of the $Fe_2S_2(CO)_6$ complex. The dashed line represents the bent metal-metal bond (adapted from reference [81]).

It was not until 1979 that Seyferth and Henderson fully described the synthetic pathway leading to this sort of compound, which was developed from the "smelly" reaction between $Fe(CO)_5$, KOH and polysulphide. [83] The resulting complex was composed of two iron centres linked by two thiolato bridges, and each iron centre was surrounded by three carbonyl ligands. The two sulphurs constituting the thiolato bridges were either bridged or directly bonded together. In 1982, Winter *et al.* [84] described the synthesis of what unknowingly turned out to be the earliest synthetic model for the sub-site of [FeFe]-hydrogenase. In this complex the two sulphurs are joined by a $-(CH_2)_3-$ unit giving a propanedithiolate (pdt) bridging the two iron centres.

The striking resemblance of this complex with the {2Fe-2S} sub-site paved the way for the synthesis of analogues to the H-cluster. Using this type of compound as a basis, a large number of iron hexacarbonyl complexes have been synthesised.

b) {2Fe-2S} frameworks

Determination of the X-ray crystal structure of [FeFe]-hydrogenase encouraged the organometallic community to reconsider the chemistry of these $[Fe_2(SR)_2(CO)_6]$ (R = alkyl group) systems. The synthesis of the propanedithiolate (pdt) bridged diiron hexacarbonyl was the first step through the synthesis of the first models of {2Fe-2S} sub-site. [84, 85]

The ligands surrounding each metal centre have a non negligible influence on the molecule. In the enzyme, these ligands are usually carbonyl and cyanide groups. However, by synthesising compounds containing a different number of these ligands and/or ligands of different nature, one can control the properties and the catalytic efficiency of the new synthesised system. [86-88] Compounds containing only CO ligands, being easier to synthesise, were synthesised first following the method developed by Seyferth and Henderson. [83] The CN^- ligands are usually added afterwards by exchange with CO under excess of CN^-. [89, 90] The cyanation reaction is depicted in **Scheme 2.7**.

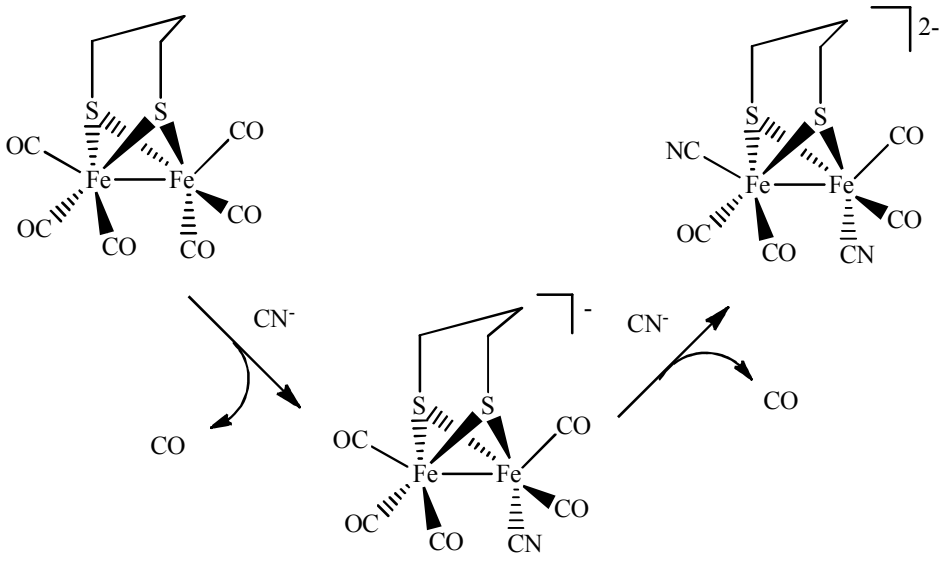

Scheme 2.7. Synthesis of the dicyanide propanedithiolate model derivative.[89, 90]

Compounds containing CN^- ligands are often made because the CN^- has the ability to stabilise the molecule more than the CO alone. Furthermore, their ability to serve as an anchor for the hydrogen due to its negative charge which can attract proton as suggested by Armstrong [58] and Rauchfuss [91, 92] is another noteworthy property. However, the overall structures of systems containing six CO and four CO with two CN^- are very similar with few geometrical differences. [93] CN^- is one of the most used ligands to replace CO ligands but a number of groups have also used phosphorus related ligands in place of CO. It has been revealed that diiron complexes with electron donating ligands can be protonated at the Fe-Fe bond. [94, 95] Thus, these phosphorus-derived systems increase the basicity of the site where protons will be bound. [96] This class of compounds include mono- (*e.g.* trimethylphosphine, PMe_3 [85]) and bidentate ligands (*e.g.*1,2-bis(diphenylphosphino)ethane, Dppe [90]) and recently, the use of a Dppe as ligand has shown promised in the creation of dihydrogen catalysts, because it involves an asymmetrical coordination environment, a key feature in the structure of

the natural site as shown by Hall *et al.* [97] and Sun *et al.*, [98] hence control the site of protonation and reduction on the compound. Other two electron donor ligands have been used, including methyl cyanide group, CNMe, [99] trimethylphosphane, $P(OMe_3)$ [100] or N-heterocyclic carbene, $(I_{Me}\text{-}(CH_2)_2\text{-}L$ where I_{Me} = 1-methylimidazol-2-ylidene, L = NMe_2). [101] Though propanedithiolate is one possibility for the bridging dithiolate ligand between the two metals of the sub-site, but amino [102] and oxo [103] derivatives are also been synthesised (**Scheme 2.8**).

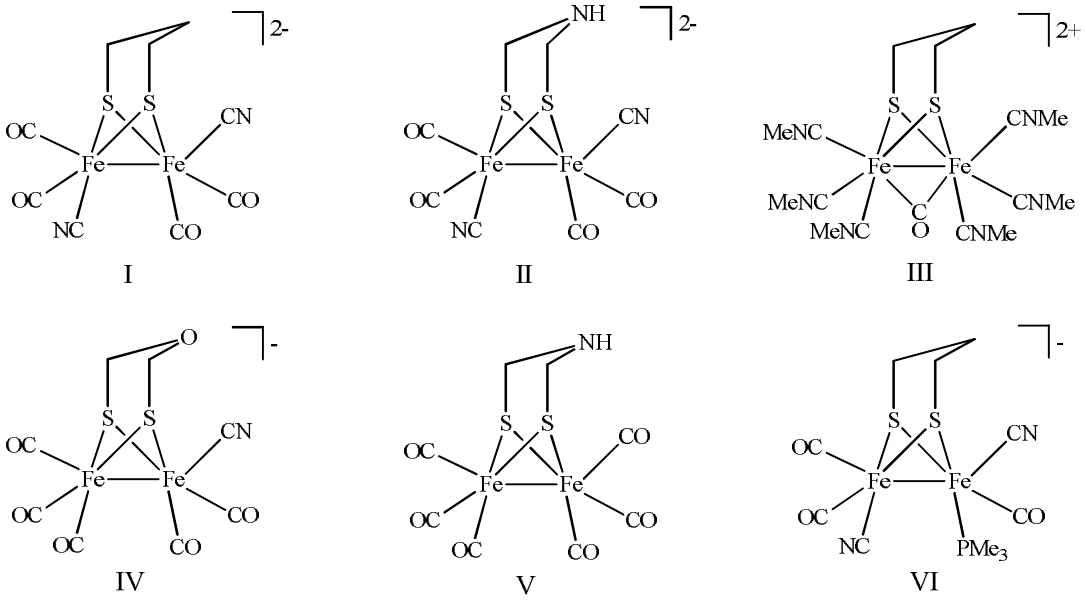

Scheme 2.8. Different {2Fe-2S} model compounds synthesised by Pickett (I [104]), Darensbourg (I, [93] VI [105]), Rauchfuss (I, [89] II, [102] III, [106] V, [102] VI [91]) and Song (IV [103]) and their co-workers.

Because of the presence of a bridging cysteine between the {4Fe-4S} cluster and the {2Fe-2S} sub-site of the H-cluster, these model complexes do not involve the third coordinating sulphur. Furthermore, the metal centres in the complexes described in {2Fe-2S} are in the Fe(I)-Fe(I) state. As discussed in **Section 2.2.3.3**, the catalytic cycle of the [FeFe]-hydrogenases involves higher oxidation states. The activation step

is reductive in nature and followed by the loss of either an aqua or a hydroxo ligand, thus creating an unoccupied coordination site and the active Fe(I)-Fe(II) oxidation state. Pickett and co-workers have therefore synthesised an Fe(I)-Fe(I) complex, $[Fe_2(MeSCH_2C(Me)(CH_2S)_2)(CN)_2(CO)_4]^{2-}$, which can stabilise the Fe(I)-Fe(II) state by the dynamic coordination of a pendant thioether arm. [107]

c) {2Fe-3S} framework

The sub-site of the H-cluster can be viewed as {2Fe-3S} assembly rather than {2Fe-2S} unit. The synthesis of the {2Fe-3S} core with carbonyl and cyanide ligands has been achieved by the synthesis of propanedithiolate, pdt ligands with a thioether group, act as one of the pendant group which allows a large range of extra-functionality to be introduced on the proximal iron. [104, 107-110] This tripodal framework is structurally very close to the sub-site of [FeFe]-hydrogenase (**Scheme 2.9**).

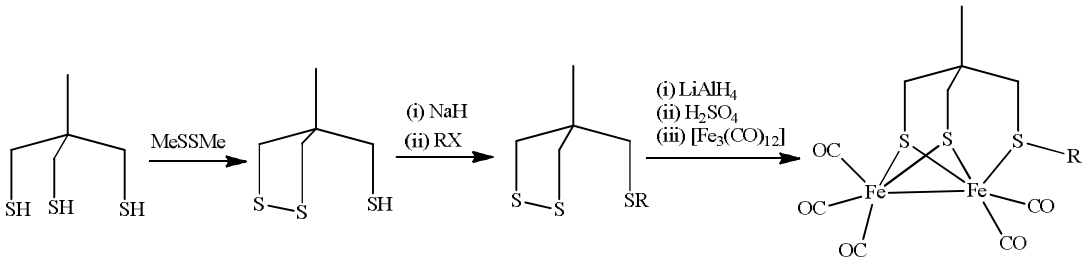

Scheme 2.9. Synthesis of {2Fe-3S}-complexes (R = Me or CH_2Ph).

The lability of the thioether group make them easily displaced by other electron withdrawing alkyl, R group, thus displaces the equilibrium toward CO bridging as observed by nuclear magnetic resonance, NMR. [104, 108]

Substitution of the pentacarbonyl dithiolate thioether system by cyanide has been studied in detail mechanistically and by theoretical methods. The cyanation of the pentacarbonyl complex gives a stable mono cyanide on the distal iron, and under further cyanation, a moderately stable intermediate can be isolated. It possesses a bridging carbonyl ligand and one CN^- on each iron, which is a key structural element of the CO inhibited form of the H-cluster.

Apart from dithiolate thioether system with pdt bridgehead, Rauchfuss and his co-workers [111] managed to synthesise this tripodal system with a nitrogen unit bridgehead. It can be mentioned that tripodal dithiolate ligands with appended amine, pyridine and other groups have been synthesised as well (**Scheme 2.10**) and these molecules have been investigated in the context of both hydride formation and generation of CO binding sites. [108, 111]

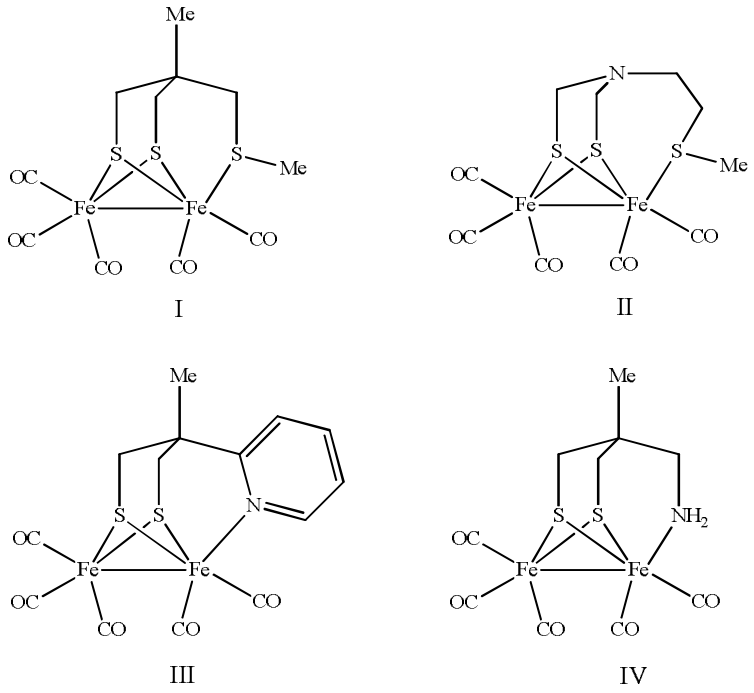

Scheme 2.10. Different {2Fe-3S} model compounds synthesised by Pickett (I, [104, 107] III, [108] IV [108]) and Rauchfuss (II [111]) and their co-workers.

When a CO ligand bridges the two iron atoms which are coordinated by CO and CN^- as depicted in **Figure 2.11**, Razavet *et al.* reported that this structure could be supported by a Fe(I)-Fe(II) unit. [110] This work shows a transient Fe(I)-Fe(II) bridging carbonyl species can be generated electrochemically and was characterised by fourier transform infrared, FTIR and stopped-flow methods. It exhibits a very similar spectrum to what has been observed with H_{ox}-CO active. [49] This supports the low oxidation state of the irons in the sub-site.

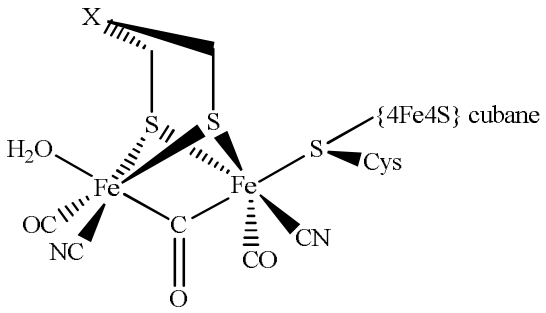

Figure 2.11. Schematic representation of active site of [FeFe]-hydrogenase (X = CH_2, NH, O).

The synthesis of mixed-valent Fe(I)-Fe(II) systems has been achieved using more subtle combinations of mono phosphine, diphosphine, and carbene units to form the steric effect. [112-117] It is notable that this kind of bulky ligand appears to play an imperative part in stabilising the sub-site systems by protecting the five-coordinate site, thus allowing isolation of compounds for further characterisation especially in X-ray crystallography studies. **Figure 2.12** lists out examples on the obtained crystal structures based on this approach.

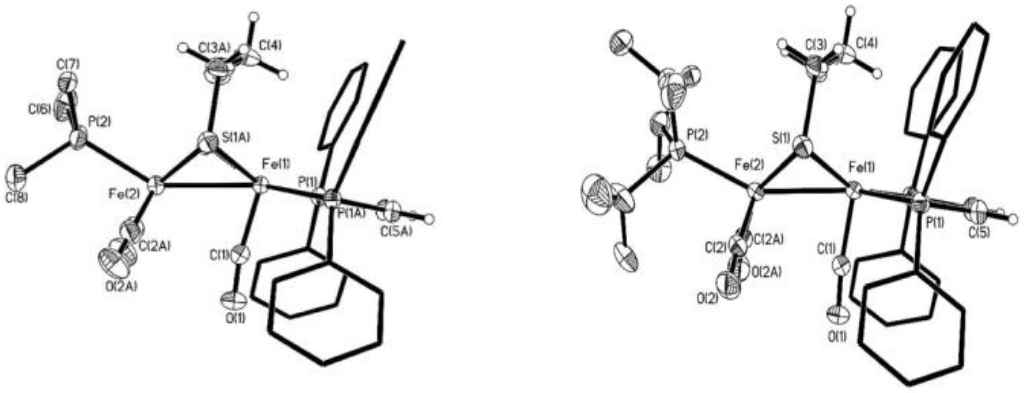

Figure 2.12. ORTEP view on the structure of the cation in $[Fe_2(S_2C_3H_6)(CO)_3(PMe_3)(dppv)]BF_4$ (left) and $[Fe_2(S_2C_3H_6)(CO)_3(P\textit{i}\text{-}Pr_3)(dppv)]BF_4$ (right) with thermal ellipsoids set at the 35% probability level (adapted from ref. [113, 114]).

The major challenge of modelling the actives site of [FeFe]-hydrogenase is to find a complex able to catalyse reversibly proton reduction. However, a clear failure of the synthetic diiron systems so far described is their inability to oxidise dihydrogen to protons, and this is of course related to their operation at potentials substantially removed from thermodynamic reversibility.

d) H-cluster models

As what has been known, sub-site in the enzyme is linked to a cubane unit by a μ-thiolate bridge. Song and co-workers showed that thiophenyl was capable of bridging a sub-site structure and the iron atom of a η5-cyclopentadienyl dicarbonyl iron unit. [103] Beyond a Fe(μ-SR)Fe linkage, relevance to the H-cluster is somewhat tenuous, biological system clearly proved the interplay between iron-sulphur cubane and iron sub-site in the H-cluster. Pickett and co-workers in 2005 reported the first synthesis of a freestanding H-cluster model complex (**Figure 2.13**) in which an $\{Fe_4S_4\}$ cubane cluster is coupled to an {2Fe-3S} sub-site as in [FeFe]-hydrogenase together with its

spectroscopic and electrochemical details which provide an insight into the electronic properties of the synthetic assembly. This brings major step in synthetic biochemistry placed in the context of the natural system. [109]

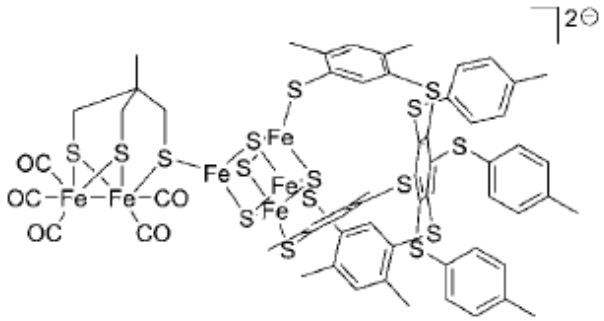

Figure 2.13. Synthetic analogue of H-cluster model (taken from ref. [5, 109]).

The isolation and characterisation of H-cluster complex with single diiron sub-site substitution by wrapping up the remaining cubane site with tripodal thiolate ligand, [118] indicates the essential $\{Fe_6S_{10}\}$ core or better described as an electronically inseparable {6Fe} cluster and presence of intrinsic electron withdrawing nature within the pentacarbonyl sub-site unit with ethyl thiolate.

e) Tetra-iron hexathiolate, $[Fe_2(CO)_4(CH_3C(CH_2S)_3]_2$

A stable tetra-nuclear which possesses two fused {2Fe-3S} sub-site units has been synthesised by Pickett and co-workers (**Figure 2.14**). [119] This tetra-iron complex, {4Fe-6S} is obtained by oxidative elimination of dihydrogen and loss of CO from the parent $[Fe_2(CO)_5\{CH_3C(CH_2S)CH_2SH\}]$. Interestingly, looking at formal oxidation states of irons in the molecule, external irons can be considered as Fe(I), and internal irons as Fe(II). This observation shows interesting electronic similarities with the natural {2Fe-2S} sub-site, its semi-reduced form as suggested by spectroscopists. [49] All previously synthesised complexes contain Fe(I)-Fe(I) diiron centres whereas here the presence of

an Fe(II) suggests the possibility of synthesising mixed valence compounds of relevance to [FeFe]-hydrogenase. The {4Fe-6S} undergoes two one-electron reductions, forming $\{4Fe\text{-}6S\}^{-}$ and $\{4Fe\text{-}6S\}^{2-}$ at -1.22 and -1.58 V (*vs.* Fc/Fc^{+}), respectively, in dichloromethane (CH_2Cl_2) solvent. Best, Pickett and co-workers undertook further and more detailed mechanistic studies of the system. [120] The density functional theory (DFT) calculated structures and FTIR spectra of {4Fe6S}, $\{4Fe6S\}^{-}$, and $\{4Fe6S\}^{2-}$ in comparison to the spectra from spectroelectrochemical, SEC experiments showed that {4Fe-6S} and $\{4Fe\text{-}6S\}^{-}$ have all terminal COs structures, whereas $\{4Fe\text{-}6S\}^{2-}$ has a bridging CO on each iron pair. [121] Fascinatingly, unlike the other Fe(I)-Fe(I) models, such as {4Fe-6S} which have all terminal COs, [89, 91, 122] the $\{4Fe\text{-}6S\}^{2-}$ species with equivalent oxidation states of all four Fe(I) has a bridging CO structure similar to the structure of the diiron sub-site in the H_{red} state of [FeFe]-hydrogenase. Moreover, when the 2,6-dimethylpyridinium acid ($LutH^{+}$) is used as a proton source, the rate of H_2 production for {4Fe-6S} at the lower potential is significantly higher than that for $Fe_2(\mu\text{-}S(CH_2)_3S)(CO)_6$ and $Fe_2(\mu\text{-}PPh(CH_2)_3PPh)(CO)_6$. [120] Simulations of the electrochemical results on {4Fe-6S} suggested that the slow H_2 production at the first reduction potential is an ECEC process, meaning one-reduction of {4Fe-6S} is followed by protonation to form a bridging hydride complex, then a second one-electron reduction is followed by a second protonation. In contrast to that, the more rapid H_2 production at the second reduction potential is an EECC process, where $\{4Fe\text{-}6S\}^{2-}$ with the bridging carbonyl on the diiron is protonated at a terminal iron and produces H_2 by picking up a second proton and regenerating back to {4Fe-6S}. [121]

Generally, it appears that terminal hydride structures become more favourable in more highly reduced species, and that the rapid hydrogen production from reduction of {4Fe-6S} to $\{4Fe\text{-}6S\}^{2-}$ is mainly through the proton reduction at a terminal position on a

single iron, rather than at a bridging position that is blocked by bridging COs in {4Fe-6S}$^{2-}$. This conclusion lends further support to the notion that the protein structure in the [FeFe]-hydrogenase supports and maintains a bridging or semi-bridging CO and an open terminal site for protonation. [121]

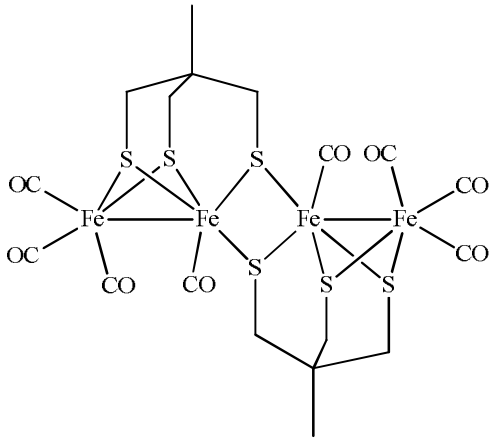

Figure 2.14. A view of the structure of $[Fe_2(CO)_4(CH_3C(CH_2S)_3]_2$. The two external Fe atoms are formally Fe(I) and the two internal Fe atoms are formally Fe(II).

f) Electrocatalysis of hydrogen evolution for synthetic analogues

As seen in the previous section, the {2Fe-3S} of H-cluster in the biological system is linked to a {4Fe-4S} cluster whose role is to deliver electrons to the diiron part. The reduction is an important part of the catalytic cycle as it induces protonation, which leads to the molecular hydrogen formation. A number of experiments focusing on the behaviour of the diiron compound at different levels of oxidation or reduction have been reported. [54] The reduction of diiron on the sub-site is the key point of dihydrogen production [68] and as such, it has been extensively studied using electrochemistry. [91, 123-125]

The proposed reaction pathway involved protonation of the diiron and also on the σ-donor properties of the ligands, which may occur either before or after one-electron reduction. Rauchfuss and co-workers [91, 92] reported the first example of electrocatalysis of proton reduction by a diiron system, the mono cyanide $[Fe_2(SC_3H_6S)(CN)(CO)_4(PMe_3)]^-$ which possesses a phosphine ligand. As established from spectroscopic data, [106, 126] catalysis by the cyanide/phosphine derivative involves protonation firstly at the metal-metal bond forming a stable and well-characterised bridging hydride and secondly at the cyanide ligand.

One of the possible oxidation states of the sub-site analogues during catalysis has been proposed by Darensbourg and co-workers [87] where they have adopted a strategy focuses on the use of weak acetic acid (p*K*a 28 in MeCN [127]) as the proton source. The weak acid avoids complications such as the irreversible destruction of the catalytic material. In their study, the initial oxidation state of the iron cores is proposed as Fe(I)-Fe(I) and its potential reduction cycles is displayed in **Scheme 2.11**. The first possible pathway (Pathway 1) involving $[Fe_2(\mu\text{-}S_2R)(CO)_6]$ where R = C_2H_5, C_3H_6 or *o*-$CH_2C_6H_4CH_2$ shows two successive electron additions and the resulting oxidation state becomes $[Fe(0)\text{-}Fe(0)]^{2-}$ through Fe(0)-Fe(I) anion intermediate. Two protons are added successively from this oxidation state, *via* a proton intermediate, $[(H)Fe(II)\text{-}Fe(0)]^-$. This is follows by the regeneration of Fe(I)-Fe(I) when the dihydrogen formed is released. The second possible catalytic pathway (Pathway 2) using $[Fe_2(\mu\text{-}S_2R)(CO)_4(PMe_3)_2]$ is parallel to the first with the difference that a proton is added immediately after each addition of a single electron. Contrary to the work reported by Rauchfuss and co-workers which involved stronger acids (HBF_4 in Et_2O), [91] no reaction of the neutral bis(phosphine) complexes with protons from acetic acid was observed. Electrochemical and DFT studies of the electrocatalytic proton reduction reaction of

acetic acid with the benzene-1,2-dithiolate sub-site analogue have revealed that the reaction proceeds with significant structural reorganisation following two-electron reduction and it is at this level that the first protonation step occurs, further reduction and protonation lead to dihydrogen elimination. [128]

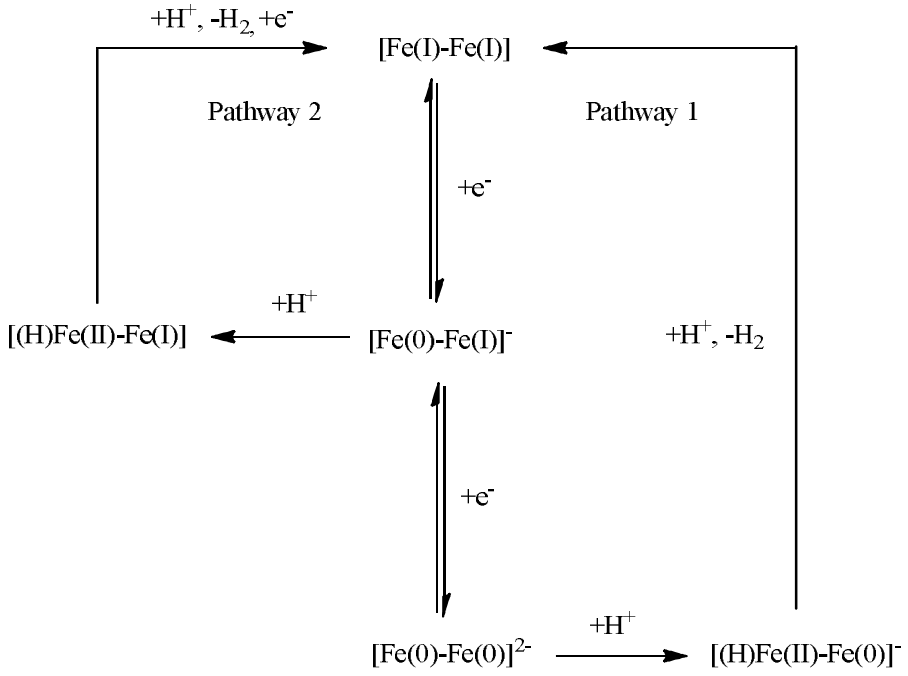

Scheme 2.11. Oxidation states of the iron centres during the catalytic process as proposed by Darensbourg and co-workers. [87]

On another hand, De-Gioia and co-workers [129] have proposed that the initial state of the sub-site possesses Fe(II)-Fe(I) oxidation state, which displays at **Scheme 2.12**. Addition of an electron generates an oxidation state of $[Fe(I)-Fe(I)]^-$ followed by the addition of the first proton. This leads to the iron cores become proton rich with [(H)Fe(II)-Fe(I)]. Similarly an electron and then a proton are added a second time giving two proton on the iron core, $[(H_2)Fe(II)-Fe(I)]$, using the previous stage,

[(H)Fe(II)-Fe(I)] as the intermediate. The initial species is then regenerated by release of the dihydrogen molecule formed. Both propositions are present in the biological catalytic processes and are dependent of the activation process of the enzyme.

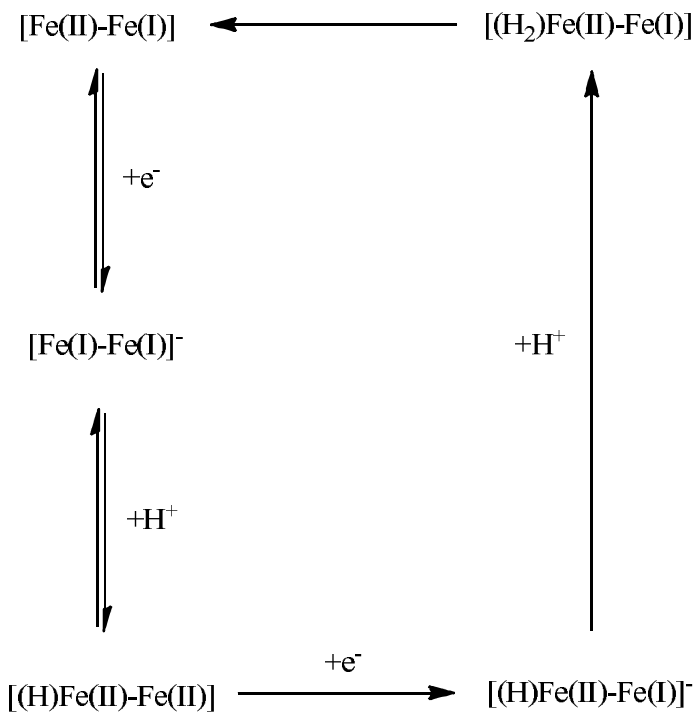

Scheme 2.12. Oxidation states of the iron centres during the catalytic process as proposed by De Gioia and co-workers. [129]

Chapter 3

Synthesis of Materials

For the subsequent work described in this thesis, it is necessary to synthesis diiron units and synthetic cubane clusters as well as monomers for electropolymerisation. Details of the chemistry of synthesis H-cluster systems presented in this chapter are highly relevant to the chemistry of the active site of [FeFe]-hydrogenase, in terms of the development of new materials as potential electrocatalysts for hydrogen fuel/producer cells. In general, literature methods were employed but with some key synthesis, the procedure was substantially improved upon. All experimental details for the synthesis of the materials used are described.

3.1 Experimental methods

In this work, the synthetic compounds were generally characterised by the standard techniques such as NMR (Nuclear Magnetic Resonance), FTIR (Fourier Transform Infrared Spectroscopy), ES-MS (Electron Spray Mass Spectroscopy) and micro-analysis.

Micro-analysis was performed at the London Metropolitan University, London.

ES-MS analysis was performed at Swansea University, Swansea, UK.

NMR spectroscopy was recorded on a JEOL Lambda 400 MHz and FTIR on a Perkin Elmer BX single beam spectrometer, FTIR-8300.

All manipulations were performed under an inert atmosphere of N_2 using Schlenk technique. Solvents were dried and distilled under N_2 following standard procedures (Na for toluene, hexane and diethyl ether, Na/benzophenone for tetrahydrofuran, Mg for methanol and CaH_2 for acetonitrile and dichloromethane). Chemical compounds were purchased from Sigma-Aldrich, Fluka and BDH and unless otherwise stated were used as supplied without further purification.

All synthesised model complexes in this thesis have an initial Fe(I)-Fe(I) oxidation state. Each Fe(I) centre has a d^7 configuration and the unpaired electron from each Fe centre form the Fe-Fe bond. The complexes are thus diamagnetic compounds and can be studied by nuclear magnetic resonance spectroscopy.

Notes on metal carbonyl species for FTIR measurements:

FTIR spectroscopy is invaluable in characterising the metal species described in this work because CO and CN^- ligands are strong chromophores and are sensitive to the electron richness of the metal centre. FTIR spectroscopy of carbonyl and cyanide ligands is commonly used in organometallic chemistry to probe the electronic environment around metal centres.

FTIR spectra arise from transitions between vibrational states of a molecule and the associated dipole moment changes. Compounds containing the polar CO units like carbon monoxide or carboxylate complexes exhibit strong and sharp CO-stretching bands. There are three metal-CO bonding interactions: i) metal-CO σ-bonding, ii) metal

to CO π-back bonding and iii) CO to metal π-bonding as illustrates in **Scheme 3.1**. The FTIR frequency is given by the bond strength and the reduced mass. In coordination compounds, the electron density at the metal centre effects the strength of the CO-bond and thereby its frequency. Terminal CO generally absorbs at higher frequencies (1850-2125 cm^{-1}; 2155 cm^{-1} for free CO) than a bridging CO (1700-1860 cm^{-1}). Terminal CO frequencies can be quite low if CO ligands are good donors but poor π-acceptors or if the molecule is negatively charged. In both cases, the back-donation is much larger. The lowest unoccupied molecular orbital (LUMO) of CO is an anti bonding π*-orbital and is low enough in energy to function as an acceptor orbital when interacting with filled *d*-orbitals on metals. This is the reason why coordination to electron rich metal centres shifts the υ(CO) stretching frequency to lower energy as the C-O bond weakens due to the $d \rightarrow \pi^*$ back-bonding. [49] The more back-donation from the metal to CO leads to stronger metal-carbon bond (*i.e.* shorter) and weaker C-O bond (*i.e.* longer). Therefore the CO-ligands in iron carbonyl complexes can be used as spectator ligands that monitor the electron density at the metal centres. [130] This justification can be used to explain the shifting in frequencies for different {2Fe-3S} complexes in this study.

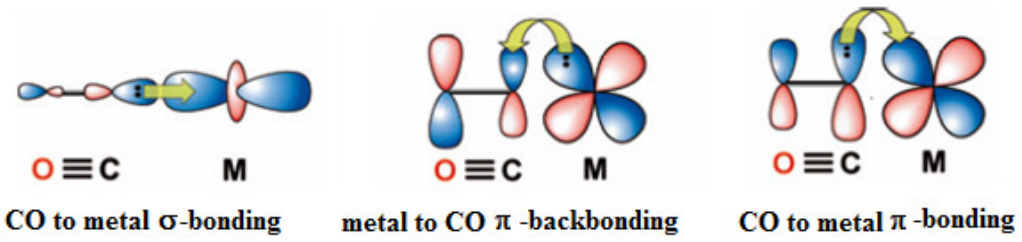

Scheme 3.1. The three metal-CO bond interactions.

3.2 $[Fe_4S_4(SPh)_4][(NBu_4)_2]$: Iron-sulphur cluster

The complex $[Fe_4S_4(SPh)_4][(NBu_4)_2]$ was synthesised by the scheme outlined in **Scheme 3.2**. The synthesis route to this material has been established by Holm and co-workers over several years. [62] To synthesise the iron-sulphur cluster, $[Fe_4S_4(SPh)_4][(NBu_4)_2]$ (**1**), sodium methoxy was prepared by reacting metal sodium with dry methanol, the solution was then added with thiophenol, followed by iron binding on the thiol site and insertion of cation tetrabutylammonium to stabilise the negative charge. Extra precautions have to be taken during synthesis as the iron-sulphur cluster is highly air sensitive.

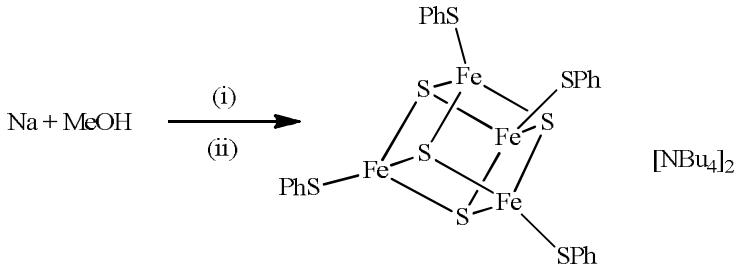

1

Scheme 3.2. Synthesis of $\{Fe_4S_4\}$ cluster (**1**). (i) thiophenol, CH_3OH, RT; (ii) $FeCl_3$, sulphur, $[NBu_4][I]$, RT.

3.3 Ligand synthesis: The tripodal $CH_3C(CH_2SH)_3$

As discussed in previous Chapter (refer **Section 2.2.3.2**), the active site of [FeFe]-hydrogenase, the H-cluster, consists of a {4Fe-4S} cubane cluster which is linked to a {2Fe-2S} sub-site, through a cysteine residue (**Scheme 3.3**).

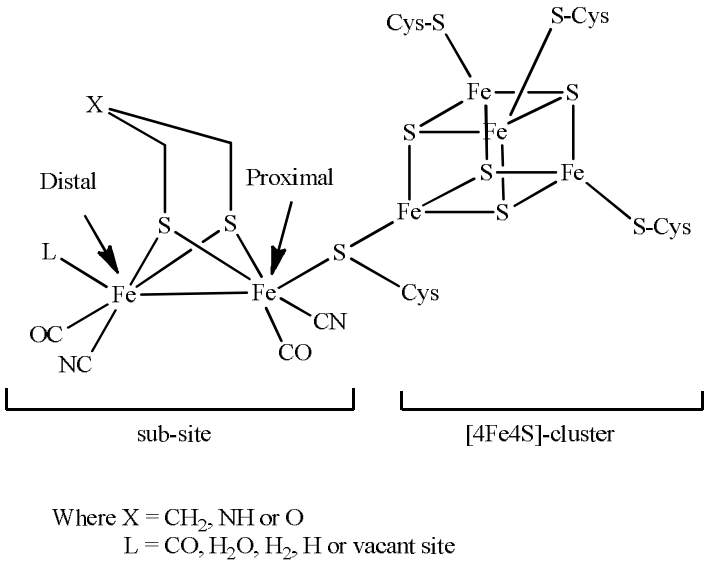

Where X = CH_2, NH or O
L = CO, H_2O, H_2, H or vacant site

Scheme 3.3. The [FeFe]-hydrogenase active site, H-cluster.[47, 48]

As discussed in **Chapter 2**, the {2Fe-2S} assembly was first reported [80] more than three quarters of a century ago and developed further half a century later, [131] and this paved the way for the synthesis of sub-site models of [FeFe]-hydrogenase. However, it can be argued that the protein sub-site is best considered as a {2Fe-3S} rather than {2Fe-2S} unit [104, 110] because an extra sulphur group/arm is required to introduce further functionality on the proximal iron. This {2Fe-3S} framework is structurally very close to the sub-site of [FeFe]-hydrogenase. To construct a complex that mimics {2Fe-3S} sub-site system, we begin with the tripodal ligand, $CH_3C(CH_2SH)_3$. This ligand was first described by Bosnich and his co-workers in the early eighties. [132] It was found that only a few complexes containing 1,1,1-tris(thiolatomethyl)ethane and its reactivity towards different transition metals have been described in the literature. An iridium-carbonyl complex $[Ir_3(CO)_6(CH_3C(CH_2S)_3]$ has been characterised by Poilblanc and co-workers where the trithiolato ligand coordinates a triangle of non-bonded iridium atoms. In the same study, analogues rhodium compound have been synthesised, as well as complexes in which CO is replaced by tertiary phosphine. [133]

Some studies also reported the synthesis of mercury complexes $[CH_3C(CH_2S)_3(HgCH_3)_3]$. [134] The mononuclear complex $[(CH_3C(CH_2PPh_2)_3)Rh(CH_3C(CH_2S)_3)$ has also been described. [135] Synthetic modifications of this ligand could also lead to organic self-assembled monolayer on gold electrodes. [136]

The tripodal ligand is synthesised from 1,1,1-tris(hydroxymethyl)ethane **2** which is activated by tosylation (**3**) to incorporate a thiocyanate group (**4**). The reduction by $LiAlH_4$ of **4** leads to the desired trithiol ligand **5** (**Scheme 3.4**). This starting material can be prepared on a multi-gram scale.

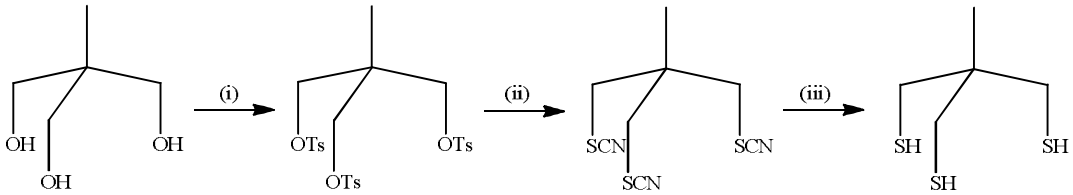

2 **3** **4** **5**

Scheme 3.4. Synthesis of the tripodal ligand $CH_3C(CH_2SH)_3$. (i) TsCl, pyridine, RT, 93%; (ii) KSCN, DMF, 135 °C, 74%; (iii) $LiAlH_4$, diethyl ether, 40°C, 73%.

With this ligand, we have the {2Fe-3S} complexes backbone. Our key synthesis is to generate an active {2Fe-3S} complex where it is able to link to an $\{Fe_4S_4\}$ cubane type cluster. The reverse procedure can be envisaged to solve this problem:

- synthesis of an activated form of the diiron carbonyl sub-site
- then react it with an iron-sulphur cubane.

3.4 $[Fe_2(CO)_6(CH_3C(CH_2S)_2CH_2SCOCH_3)]$: An activated diiron sub-site

It was reported in the seventies by Holm and co-workers that halide iron-sulphur clusters can be prepared from $[Fe_4S_4(SEt)_4]^{2-}$ and benzoyl chloride, releasing ethylthiobenzoate (**Equation3.1**). [137] Following this observation, the synthesis of an acyl activated diiron centre able to reproduce such reactivity was undertaken.

$$Fe_4S_4(SEt)_4]^{2-} + Ph\text{-}CO\text{-}Cl \rightarrow [Fe_4S_4Cl_4]^{2-} + Ph\text{-}CO\text{-}SEt \qquad (\textbf{Equation3.1})$$

As reported in earlier work from the group, [104, 109, 110, 138] the trithiol ligand, $CH_3C(CH_2SH)_3$ **5** reacts with acetic anhydride under basic conditions to give the thioester dithiol compound together with di- and tri-functionalised materials. Column chromatography allowed isolation of the clean mono substituted target ligand in moderate yield. The reaction of the thioacetyl ligand in toluene with $[Fe_3(CO)_{12}]$ led to the isolation of two compounds, the previously identified "open form" hexacarbonyl diiron complex, $[Fe_2(CO)_6(CH_3C(CH_2S)_2CH_2SCOCH_3)]$ and a "closed form" pentacarbonyl complex $[Fe_2(CO)_5(CH_3C(CH_2S)_2CH_2SCOCH_3)]$ (**Scheme 3.5**).

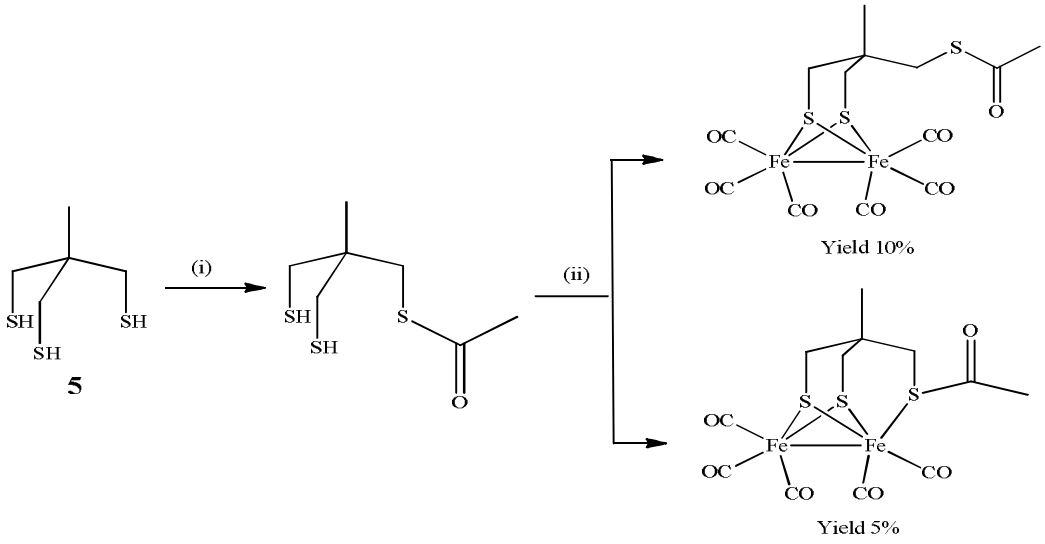

Scheme 3.5. Synthesis of the {2Fe-3S} thioester complex through mono substituted thioacetyl ligand. (i) Acetic anhydride, $NaHCO_3$, diethyl ether, RT (ii) $[Fe_3(CO)_{12}]$, toluene, 80 °C (ref. [110, 138]).

These complexes were purified by flash chromatography and characterised spectroscopically. The FTIR of the carbonyl region of $[Fe_2(CO)_6(CH_3C(CH_2S)_2CH_2SCOCH_3)]$ shows three major bands (2073, 2035, 1971 cm^{-1}). In $[Fe_2(CO)_5(CH_3C(CH_2S)_2CH_2SCOCH_3)]$, as expected, a set of lower frequencies is observed, υ (CO)/cm^{-1} 2018, 1983, 1927, because on CO is replaced by a more donating thioether ligand.

Previous studies of alkyl and benzyl thioether complexes with the {2Fe-3S} core exposed to carbon monoxide at one atmosphere exhibited no reactivity as the CO did not displace the thioether group to any significant extent. [139] Nevertheless, it is noted by exposing the solution of $[Fe_2(CO)_5(CH_3C(CH_2S)_2CH_2SCOCH_3)]$ under a CO atmosphere overnight, the hexacarbonyl, $[Fe_2(CO)_6(CH_3C(CH_2S)_2CH_2SCOCH_3)]$ can be obtained as represented in **Equation 3.2**. It was reasoned that the aryl thioether complexes are considerably more reactive and easily equilibrate with CO. The pentacarbonyl complex can always be recovered within few minutes by bubbling dinitrogen gas back into the complex solution.

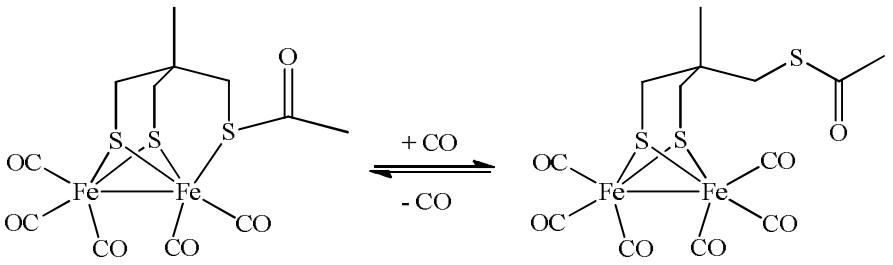

Equation 3.2

During the course of this work, we found that the diiron thioacetyl derivative can be synthesised in high yield using either the di- or the triacetylated trithiol ligand which are easier to separate from unreacted trithiol compared to its separation of the thiol from the unreacted di- and trithiol mixture.

Even under forcing conditions, it is difficult to drive the acetylation of the trithiol ligand **5** through the singe tri-substituted product **7**. Chromatography allows isolation of pure di-substituted **6** and tri-substituted **7** in yields of 21% and 37% respectively. With the di-substituted product **6**, reaction under carbon monoxide with triiron decacarbonyl, $Fe_3(CO)_{12}$ yielded 32% of the desired product **8** and a higher yield of 41% was obtained with the triacetyl ligand (refer **Scheme 3.6 and Scheme 3.7**). Both yields calculated based on the acetylated ligand used. This is a considerable improvement on earlier yield of the complex **8** from reaction with the mono acetyl. With this, we have the {2Fe-3S} complexes with thioacetyl group on it that offer the possibility to link to a synthetic {4Fe-4S} cluster *via* a bridging thiolate in polymeric systems, which will be discussed in **Chapter 4** later.

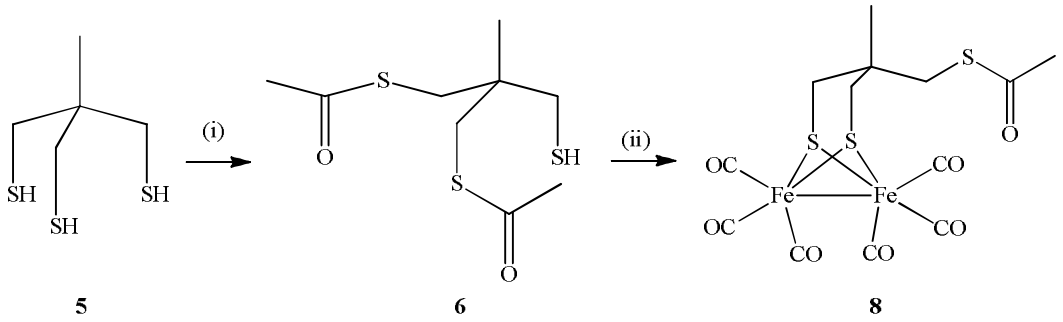

Scheme 3.6. Improved synthesis route of $Fe_2(CO)_6(CH_3C(CH_2S)_2CH_2SCOCH_3)$ (**8**). (i) Acetic anhydride, $NaHCO_3$, diethyl ether, RT; (ii) $[Fe_3(CO)_{12}]$, toluene, 90 °C, 32%.

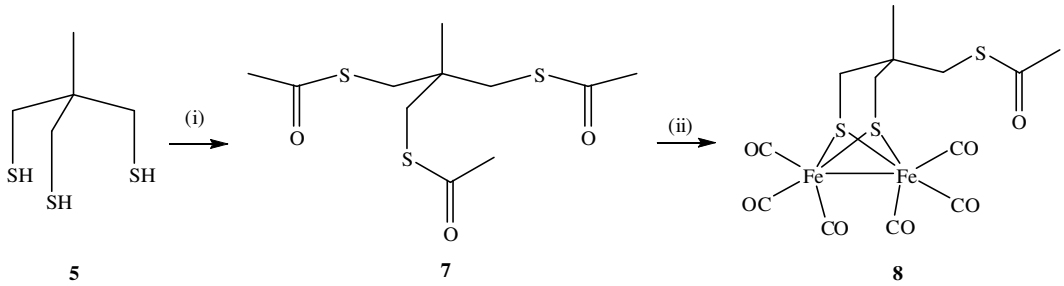

Scheme 3.7. Improved synthesis route of $Fe_2(CO)_6(CH_3C(CH_2S)_2CH_2SCOCH_3)$ (**8**). (i) Acetic anhydride, $NaHCO_3$, diethyl ether, RT; (ii) $[Fe_3(CO)_{12}]$, toluene, 90 °C, 41%.

3.5 $[Fe_2(CO)_5CH_3C(CH_2S)_2CH_2S]^-$: A water soluble anionic diiron sub-site

In order to explore the possibility of constructing a synthetic analogue related to H-cluster *via* reaction between the wild ferredoxin extracted from hyperthermophile *Pyrococcus furiosus* and synthetic {2Fe-3S} complexes (see **Chapter 5**), the synthesis of a water soluble diiron complex was undertaken. Our intention was to react the previous hexacarbonyl complex **8** with the ferredoxin. However, due to the instability of the wild ferredoxin in organic solvents (*e.g.* acetonitrile and dichloromethane) and insolubility of complex **8** in aqueous system, this approach is not possible.

To obtain a water-soluble complex, the thioacetyl arm was converted to a pendant-coordinated thiolate by methylation with sodium thiomethoxide, $NaSCH_3$. After washing with methanol to remove the excess of starting material, complex **9** was screened with FTIR and displayed the three well known characteristics bands for hexacarbonyl complexes with all bands shifting towards lower value (**Figure 3.1**). However, microanalysis was poor and we sought a route to obtain the complex free from contamination with sodium salt. The problem was solved by ion exchange with a bulky tetraphenylphosphonium cation. This enabled the isolation of analytic pure complex **10**, **Scheme 3.8** as described in the experimental section.

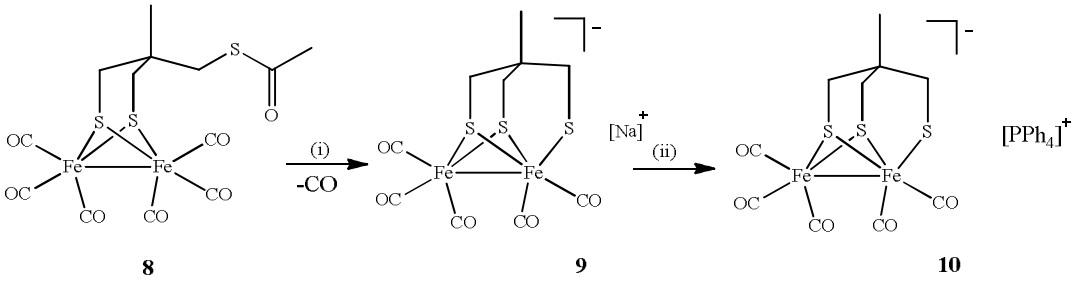

Scheme 3.8. Synthesis of ionic {2Fe-3S} complexes **9** and **10** with different cation. (i) $NaSCH_3$, CH_3CN, RT; (ii) PPh_4Cl, THF, RT (cation exchange between Na and PPh_4).

The infrared pattern of complex **10** in methanol and tetrahydrofuran, THF (**Figure 3.2)** were similar except frequencies in THF were about ten wavenumbers (cm^{-1}) lower. This can be explained by hydrogen bonding in methanol, a more polar solvent reducing the electron density on the metal centre. The frequencies for the sodium salt recorded in methanol (**Figure 3.1**) were almost identical to that of the PPh_4^+ salt in same solvent. Thus, although we were unable to obtain a clean solid sodium salt, the major ionic metal complex is almost certainly the anion **9**.

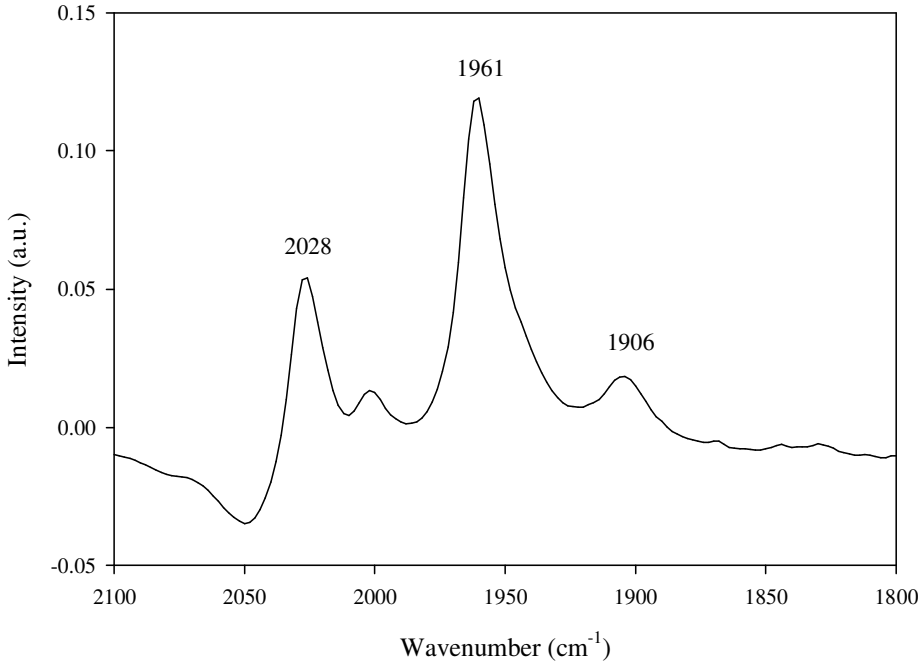

Figure 3.1. FTIR spectra of complex $[Fe_2(CO)_5CH_3C(CH_2S)_2CH_2S][Na]$ (**9**) recorded in methanol.

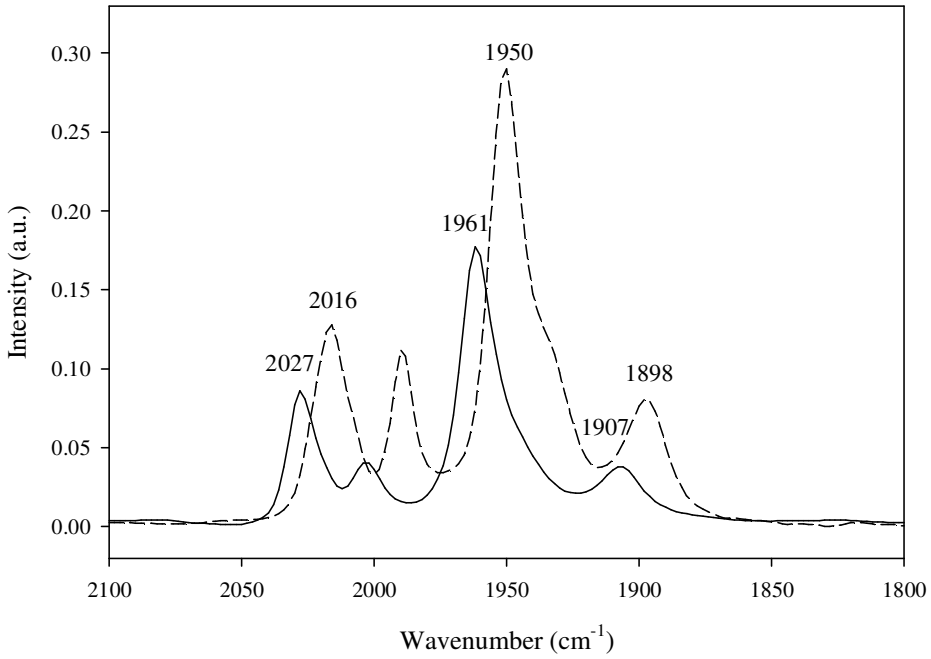

Figure 3.2. FTIR spectra of complex $[Fe_2(CO)_5CH_3C(CH_2S)_2CH_2S][PPh_4]$ (**10**) recorded in methanol (solid line) and tetrahydrofuran (dashed line).

3.6 $[Fe_2(CO)_4(CN)_2(CH_3C(CH_2S)_2CH_2SCOCH_3)][(Et_4N)_2]$: A water-soluble dicyanide complex

As discussed in the Introduction and elsewhere, two cyanide ligands are coordinated to the diiron sub-site of [FeFe]-hydrogenase. The conversion of {2Fe-3S} carbonyls to dicyanide derivatives has been described by Pickett and co-workers and the mechanism of this was investigated by stopped-flow FTIR spectroscopy (**Scheme 3.9**). [140] They were able to show that cyanide attacks occur on the iron distal to the thioether. For our purposes, we have generated dicyanide complex **11** in solution by reacting the starting material **8** with excess of tetraethylammonium cyanide (**Scheme 3.10**). Separating complex **11** from excess of tetraethylammonium cyanide was problematic.

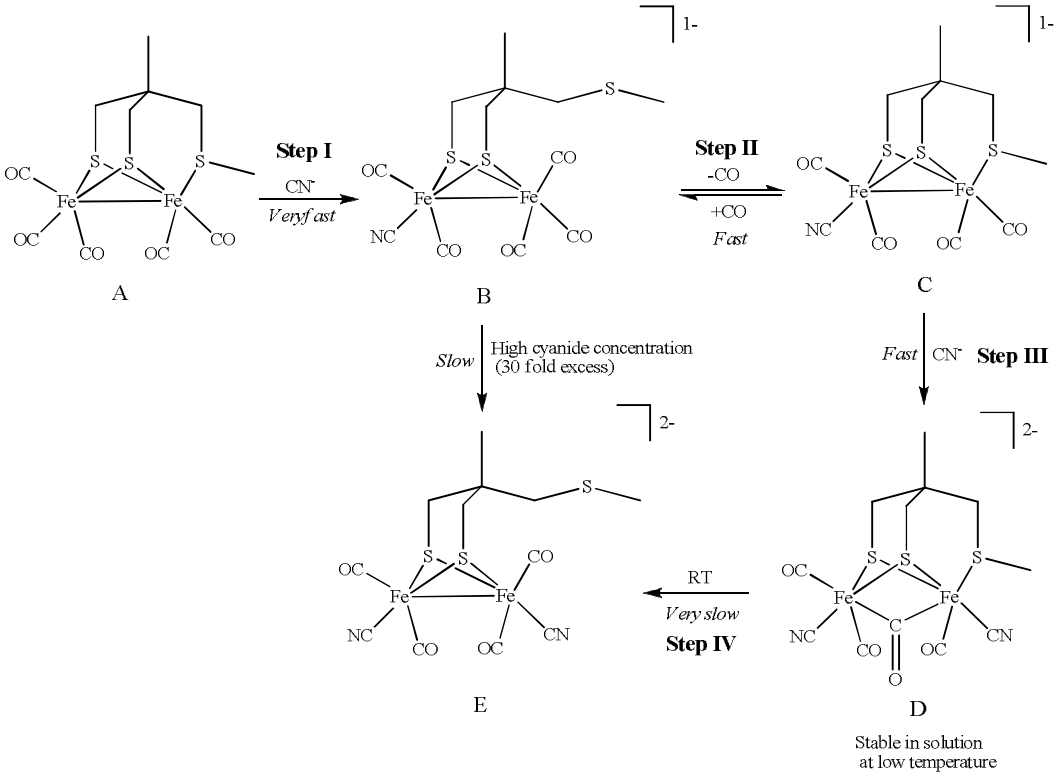

Scheme 3.9. Four steps to cyanation of the {2Fe-3S} carbonyl assembly (taken from reference [140]).

The electrochemical behaviour of the complex in presence of synthetic {4Fe-4S} cluster in solution is described in **Chapter 4**.

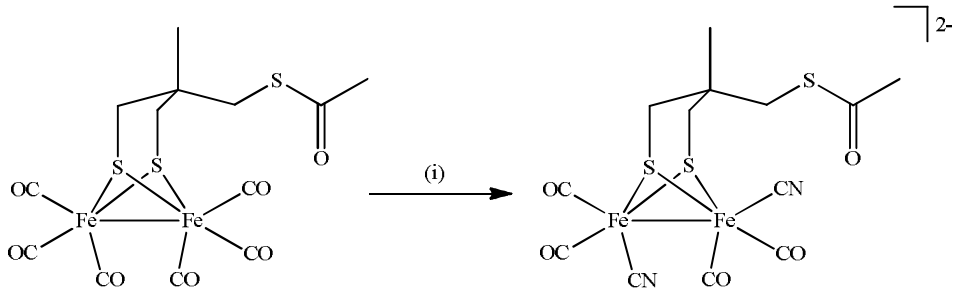

8 **11**

Scheme 3.10. Synthesis of $[Fe_2(CO)_4(CN)_2(CH_3C(CH_2S)_2CH_2SCOCH_3)][(Et_4N)_2]$ (**11**). (i) $(C_2H_5)_4N(CN)$, CH_3CN, 4 ºC.

3.7 $[Fe_2(\mu\text{-}S_2)(CO)_6]$: An unsaturated diiron complex

The synthesis of this compound, $Fe_2(\mu\text{-}S_2)(CO)_6$was first reported by Hieber and Gruber [82] in 1958 and its synthetic chemistry was developed by Seyferth and his co-workers about 30 years ago. [131] The structure of $Fe_2(\mu\text{-}S_2)(CO)_6$**,** where μ denotes as the bridging function of the sulphur atoms presents interesting opportunities for the study of chemical reactivity. Structure solved by Wei and Dahl [141] by X-ray diffraction showed that the complex is butterfly shaped (distorted Fe_2S_2 tetrahedron), with a S_2 ligand symmetrically bridging the two $Fe(CO)_3$ units. These are themselves connected by a bent metal-metal bond. [81] The complex contains potentially reactive S-S and Fe-Fe bonds where the sulphur atoms of the S_2ligand are potential electron-donor sites.

In this course of work, we used the method of Seyferth and his co-workers [131] to synthesise the $Fe_2(\mu\text{-}S_2)(CO)_6$. Iron pentacarbonyl was reacted with sodium polysulphide basic solution which leads to release of CO gas. The mixture was then acidified with diluted hydrochloric acid and H_2S was evolved. Extraction with pentane leads to the mixture of two compounds and final product (**12**) was obtained through sublimation (**Scheme 3.11**).

In this study, $Fe_2(\mu\text{-}S_2)(CO)_6$isused as catalyst bound to indium phosphide nano-crystals which act as photosensitiser for hydrogen evolution as described in **Chapter 6**.

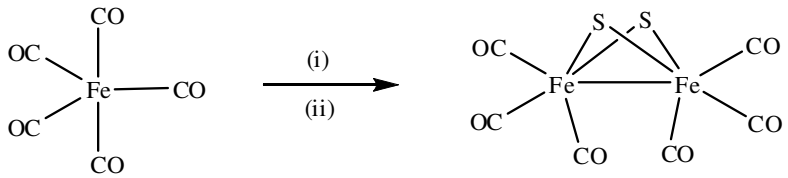

12

Scheme 3.11. Synthesis of $Fe_2(\mu\text{-}S_2)(CO)_6$ **(12)**. (i) Na_2S_5, KOH aqueous, 0 ºC; (ii) diluted HCl, extraction with pentane, sublimation at 40 ºC.

3.8 $[Fe_2(S_2C_3H_6)(CN)_2(CO)_4][(Et_4N)_2]$: A dianion for immobilisation in ionic exchange polymer

We have synthesised the known dicyano anionic complex $[Fe_2(S_2C_3H_6)(CN)_2(CO)_4][(Et_4N)_2]$ **(14)** for immobilisation in an ionic exchange electropolymer which has been synthesised following the established literature procedure. [89] This has enabled us to study the effect of polymer matrix of the reactivity of this complex towards protonation.

Three different research groups have synthesised the dicyano derivative, [89, 93, 142] and reported the structure of what is still a very good structural model for the sub-site of [FeFe]-hydrogenase. $[Fe_2(SC_3H_6S)(CO)_6]$ (**13**) reacts readily with two equivalents of cyanide, preferably Et_4NCN salt, in acetonitrile to yield $[Fe_2(SC_3H_6S)(CN)_2(CO)_4]^{2-}$ (**14**). On a preparative scale, the reaction is completed within an hour (**Scheme 3.12**). Excess cyanide does not afford further substitution. Rauchfuss and his co-workers [89] reported the crystal structure of $[Fe_2(SC_3H_6S)(CN)_2(CO)_4]^{2-}$. This crystal structure confirmed binding of two CO and one CN^- to each iron centre and displayed a peculiar arrangement for the diatomic ligands around metal centres.

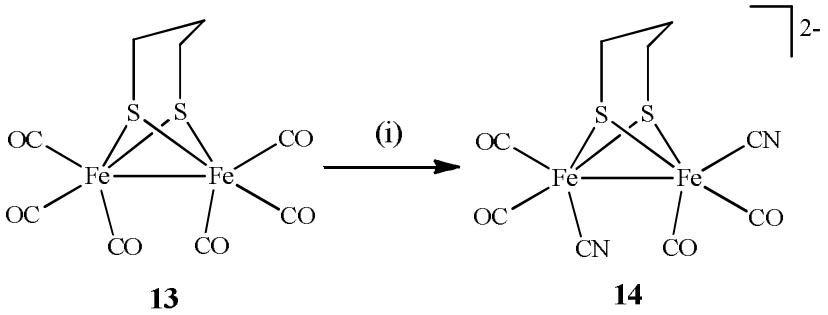

13 **14**

Scheme 3.12. Synthesis of $[Fe_2(SC_3H_6S)(CN)_2(CO)_4][(Et_4N)_2]$ (**14**). (i) Et_4NCN, CH_3CN, 0 ºC.

3.9 Confining sub-site and H-cluster system in electropolymers: Synthesis of functionalised pyrrole monomers

3.9.1 3-(pyrrol-1-yl)propyltriethylammonium tetrafluroborate

The synthesis of 3-(pyrrol-1-yl)propyltriethylammonium tetrafluroborate **(16)** monomer depicted in **Figure 3.3** was carried out by previous method established by Moutet and his co-workers. [143, 144] This monomer features a polymerisable pyrrole unit and a covalently bound unit, NEt_3^+. This monomer is a precursor for an ionic exchange poly(pyrrole) from which electro counter anion can be replaced by redox active anion species. [145]

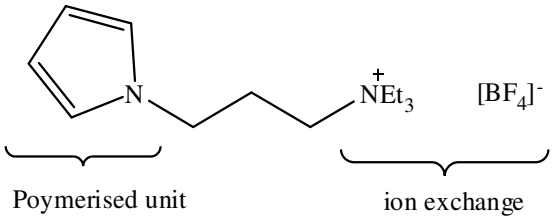

Figure 3.3. Di-functionalised pyrrole derivative monomer (**16**).

The synthetic route is outlined in **Scheme 3.13**. In our case, we are interested in incorporating an ionic sub-site group by ion exchange and specifically the $[Fe_2(SC_3H_6S)(CN)_2(CO)_4][(Et_4N)_2]$ (**14**) sub-site.

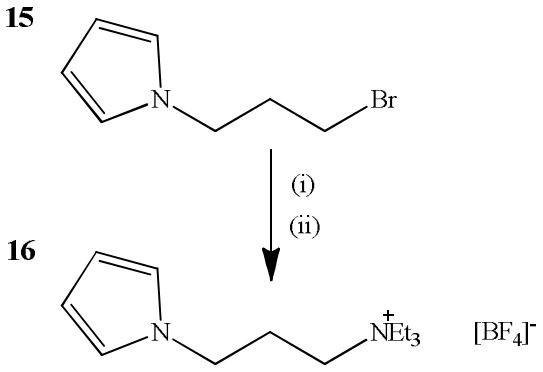

Scheme 3.13. Synthesis of 3-(pyrrol-1-yl)propyltriethylammonium tetrafluroborate (**16**). (i) $N(Et)_3$, H_2O-EtOH, 80 ºC; (ii) Amberlite IRA-BF_4^-, RT. [143, 144]

3.9.2 N,N'-bis[N-3-(pyrrol-1-yl)propanoyl]-L-cystinyl-bis-N",N" trimethylammoniumethylamide tetrafluroborate

The pyrrole-cystine-monomer, N,N'-bis[N-3-(pyrrol-1-yl)propanoyl]-L-cystinyl-bis-N",N" trimethylammoniumethylamide [BF_4] salt (**21**) is a tri-functional monomer that specially designed to assemble the artificial polyferredoxin framework once it is polymerised (**Figure 3.4**). This monomer, with its cystine unit provides S-ligation of the $\{Fe_4S_4\}^{2+}$ cluster cores once it is reduced, cholamide unit on the other hand responsible for the cationic counter ions to the bound clusters and mobile anions in order to kept the neutrality of the film, and pyrrole unit to make it polymerisable on electrode surface.

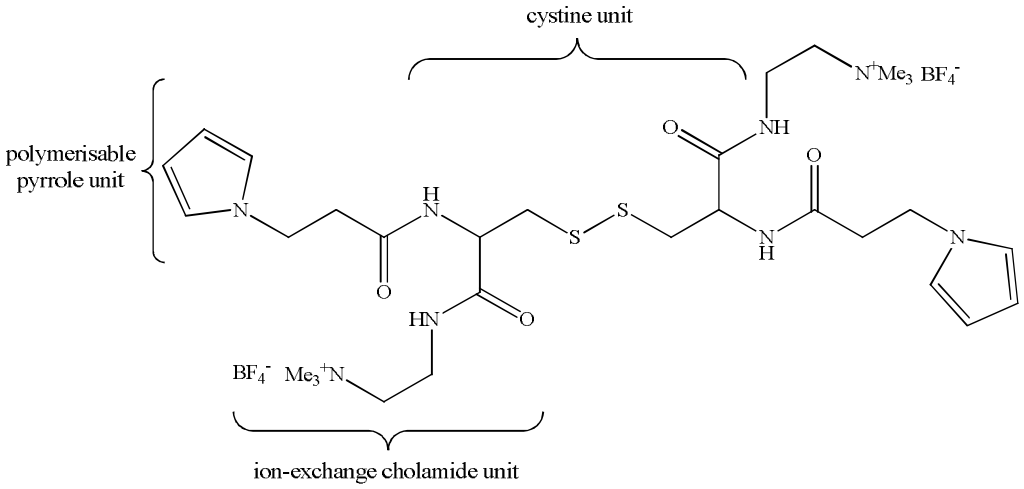

Figure 3.4. Tri-functional pyrrole-cystine-monomer (**21**).

The synthesis of the N,N'-bis[N-3-(pyrrol-1-yl)propanoyl]-L-cystinyl-bis-N",N" trimethylammoniumethylamide tetrafluroborate (**21**) was carried out by an established method and outlined in **Scheme 3.14**. [146] The monomer is synthesised from compound **17** which is a product resulted from coupling of N,N'-bis(tert-butoxycarbonyl)-L-

cysteine with 2-(dimethylamino)ethylamine. After deprotected with trifluroacetic acid, it was coupled with N-3-(pyrrol-1-yl)propanoic acid (**19**) to allow incorporation of polymerisable pyrrole unit forming N,N'-bis[N-3-(pyrrol-1-yl)propanoyl]-L-cystinyl-bis-N",N" dimethylaminoethylamide (**20**). The methylation by trimethyloxonium tetrafluroborate of compound **20** leads to the desired monomer **21**, appeared in light yellow solid. This monomer can be prepared on a multi-gram scale.

Polymerisation and subsequent chemistry of the polymer has been shown to allow the incorporation of $\{Fe_4S_4\}$ cluster in the matrix. [146] In this work, we are concern with subsequent modification of the cluster with sub-site unit specifically thioacetyl activated sub-site (**8**) discussed earlier.

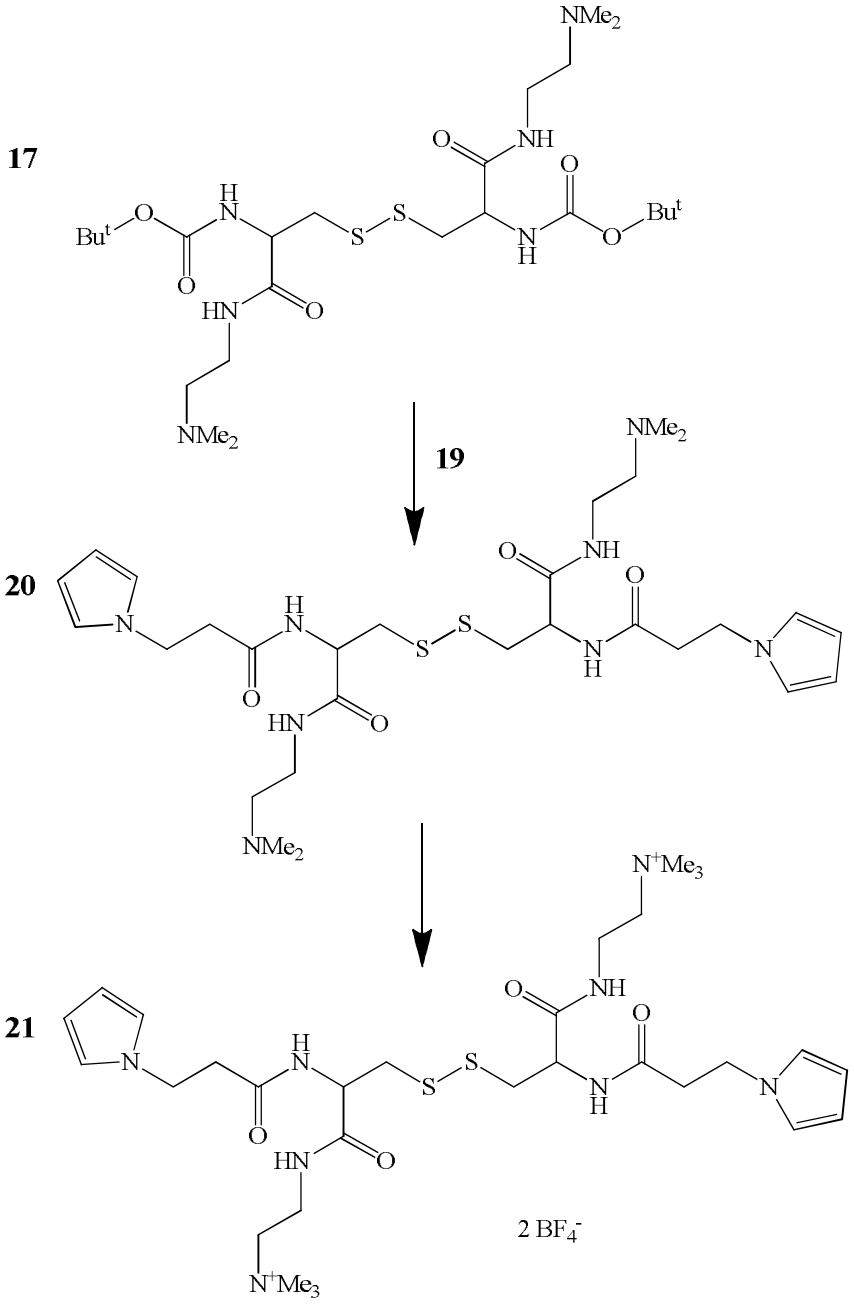

Scheme 3.14. Synthesis of pyrrole-cystine monomer derivatives (adapted from reference [146]).

3.10 General conclusions

This chapter dealt with the synthesis of materials required in subsequent studies. We have described an improved synthesis of $Fe_2(CO)_6(CH_3C(CH_2S)_2CH_2SCOCH_3)$and the synthesis of a new molecule in which a {2Fe-3S} unit is formed with a tris-thiolate coordination geometry. Notably, direct synthesis of this compound from Bosnitch's trithiol ligand has not proved possible as only tetrairon species proved characterisable in earlier work.

3.11 Experimental

$[Fe_4S_4(SPh)_4][(NBu_4)_2]$ (1)

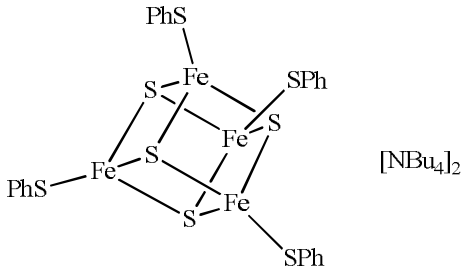

Sodium metal (2.75 g, 120 mmol) was dissolved in freshly distilled methanol (100 mL) under dinitrogen. Thiophenol (17.6 g, 160 mmol) was added and the mixture was stirred for 1 hour. $FeCl_3$(4.86 g, 30.0 mmol) was dissolved in dry methanol (50 mL) and was added into the mixture. The mixture again was stirred for one hour and sulphur (0.96 g, 30 mmol) was added and stirred overnight under dinitrogen gas flow. The reaction mixture was filtered into methanol (50 mL) containing $[NBu_4][I]$ (7.40 g, 40 mmol) and allowed to stir for a further two hours. The solution was filtered again to give fine black crystals which were washed with cold methanol (2x50 mL). The material was recrystallised from a mixture of acetonitrile/methanol (100 mL: 40 mL) which was warmed to dissolve all solid and then allowed to cool in fridge overnight.

Again, the crystal was filtered and washed with cold methanol (50 mL), followed by diethyl ether (2x50 mL) and dried under vacuum.

$CH_3C(CH_2OTs)_3$ (3)

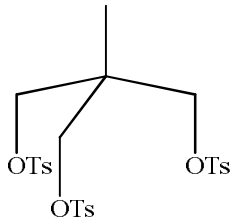

$CH_3C(CH_2OH)_3$ **(2)** (82.2 g, 680 mmol) was dissolved in degassed pyridine (300 mL) and cooled down to 0 °C. Tosyl chloride (429.0 g, 225 mmol) dissolved in degassed pyridine (500 mL) was added drop-wise, and the mixture was stirred at room temperature overnight. The solution was poured into water (2500 mL), sulphuric acid (300 mL) and ice, and the precipitate was filtered, washed with water and methanol until the pink colour disappeared and give a white powder (368 g, 630 mmol, 93%). δ_H (400 MHz; solvent $CDCl_3$; 0.89 (3H, s, CH_3), 2.47 (9H, s, CH_3Ph), 3.76 (6H, s, 3xCH_2), 7.36, (6H, d, *J* 8.6 Hz, Ph), 7.71 (6H, d, *J* 8.3 Hz, Ph).

$CH_3C(CH_2SCN)_3$ (4)

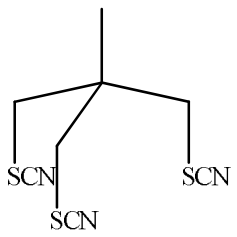

$CH_3C(CH_2OTs)_3$ **(3)** (60.2 g, 103 mmol) and KSCN (125 g, 103 mmol) were stirred in DMF (250 mL) at 140 °C for eight hours. The mixture was poured into ice and left overnight at 4 °C. The yellow precipitate was filtered and washed with water (2x500

mL), ethanol/diethyl ether (1:1) (2x50 mL) and finally with diethyl ether (2x50 mL) to give a yellow powder (18.5 g, 76 mmol, 74%). δ_H (400 MHz; solvent $CDCl_3$; standard $SiMe_4$) 1.41 (3H, s, C*H*$_3$), 3.25 (6H, s, 3xC*H*$_2$).

$CH_3C(CH_2SH)_3$ (5)

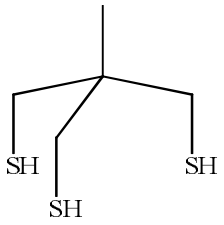

Lithium aluminium hydride (7.5 g, 198 mmol) was dissolved in diethyl ether (160 mL) under dinitrogen. The mixture was cooled in ice bath and $CH_3C(CH_2SCN)_3$ **(4)** (15.4 g, 63 mmol) was added very carefully (violent "fizzing"). The reaction was then stirred under reflux with dinitrogen overnight. The mixture was cooled in ice bath and a degassed water (100 mL) was added, follow by mixture of degassed water and HCl (1: 1) (70 mL). The product was extracted with diethyl ether (3x100 mL), and organic phase was dried with magnesium sulphate, $MgSO_4$ overnight. The solvents were removed to give yellow oil (7.74 g, 46 mmol, 73%). δ_H (400 MHz; solvent $CDCl_3$; standard $SiMe_4$) 1.0 (3H, s, C*H*$_3$), 1.2 (3H, t, *J* 8.8 Hz, S*H*), 2.6 (6H, d, *J* 8.8 Hz, C*H*$_2$).

$CH_3C[(CH_2SH)(CH_2SCOCH_3)_2]$(6) and $CH_3C(CH_2SCOCH_3)_3$ (7)

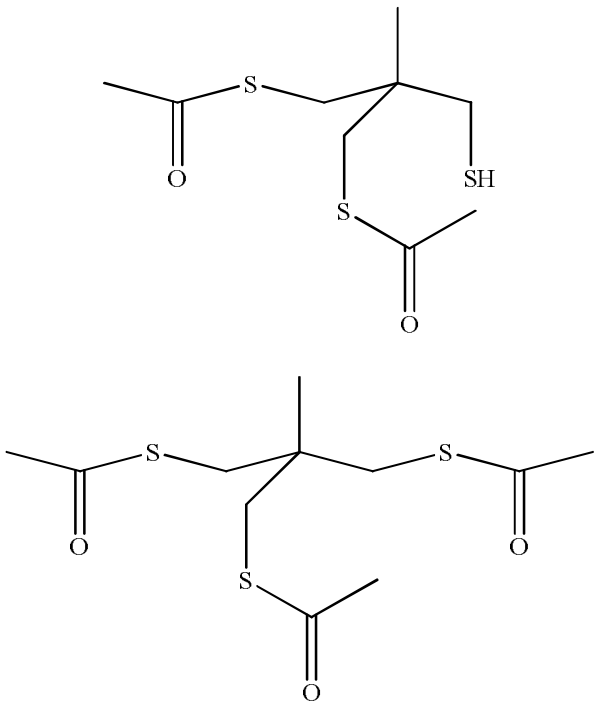

$CH_3C(CH_2SH)_3$ (**5**) (1.0 g, 5.94 mmol) was dissolved in dry diethyl ether (30 mL). Acetic anhydride (3.76 g, 370 mmol) and then sodium hydrogen carbonate (3.29 g, 370 mmol) were added and stirred for 36 hours at room temperature under dinitrogen gas flow. Degassed water (50 mL) with addition of one drop acetic acid (pH 3-4) was added and the product was extracted with diethyl ether (3x50 mL). The organic phase was dried using $MgSO_4$ and then evaporated. Two products were found. $CH_3C[(CH_2SH)(CH_2SCOCH_3)_2]$ (**6**) was purified by column chromatography (hexane/dichloromethane 1:2) to give white oil (0.32 g, 1.27 mmol, 21%). The solvent mixture was gradually changed to dichloromethane allowing $CH_3C(CH_2SCOCH_3)_3$(**7**) to be collected as white oil (0.65 g, 2.21 mmol, 37%) .

$CH_3C[(CH_2SH)(CH_2SCOCH_3)_2]$ (**6**) (Found C, 42.93; H, 6.39. $C_9H_{16}O_2S_3$, requires C, 42.83; H, 6.39%). δ_H (400 MHz; solvent $CDCl_3$; standard $SiMe_4$) 0.98 (3H, s, C*H*$_3$), 1.32 (1H, t, S*H*), 2.32 (6H, s, 2xCOC*H*$_3$), 2.47 (2H, d, C*H*$_2$SH), 3.00 (2H, s, C*H*$_2$SCO),

3.05 (2H, s, CH_2SCO). *m/z* 252 $(M)^+$, 209 $(M\text{-}CH_3CO)^+$, 167 $(M\text{-}2CH_3CO)^+$, 133 $(M\text{-}CH_3COSCH_3CO)^+$, 99 $(M\text{-}2\ CH_3COS)^+$.

$CH_3C(CH_2SCOCH_3)_3$ (**7**) (Found C, 44.96; H, 6.12. $C_{11}H_{18}O_3S_3$, requires C, 44.87; H, 6.16%). δ_H (400 MHz; solvent $CDCl_3$; standard $SiMe_4$) 0.98 (3H, s, CH_3), 2.32 (9H, s, 3xCOCH_3), 2.97 (6H, s, 3xCH_2). *m/z* 294 $(M)^+$, 251 $(M\text{-}CH_3CO)^+$, 209 $(M\text{-}2CH_3CO)^+$, 167 $(M\text{-}3CH_3CO)^+$, 133 $(M\text{-}CH_3COSCH_3COCH_3CO)^+$, 99 $(M\text{-}CH_3COSCH_3COSCH_3CO)^+$.

$Fe_2(CO)_6(CH_3C(CH_2S)_2CH_2SCOCH_3)$ (8)

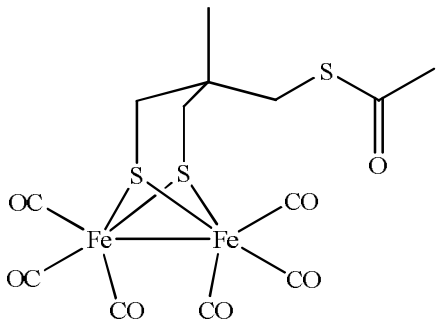

$[Fe_3(CO)_{12}]$ (1.31 g, 2.60 mmol) was dissolved in dry toluene (30 mL). $CH_3C[(CH_2SH)(CH_2SCOCH_3)_2]$ (**6**) (0.54 g, 2.16 mmol) **OR** $CH_3C(CH_2SCOCH_3)_3$ (**7**) (0.64 g, 2.16 mmol) was dissolved in toluene, added to the iron complex and heated at 90 °C for two hours under dinitrogen and condenser. The dark green mixture turns into red colour. Toluene was removed and the compound was purified by flash chromatography under dinitrogen (hexane degassed with carbon monoxide) to remove excess of $[Fe_3(CO)_{12}]$. Solvent in column was changed to hexane/diethyl ether 2:1 (degassed with carbon monoxide) to give a red oil (0.17 g, 0.69 mmol, 32%, based on **6**; 0.26 g, 0.88 mmol, 41%, based on **7**). υ_{max}/cm^{-1} (CO) 2075, 2036, 1998 and 1698

(acetonitrile); δ_H (400 MHz; solvent $CDCl_3$; standard $SiMe_4$) 1.03 (3H, s, C*H*$_3$), 2.12 (4H, br,2xC*H*$_2$SFe), 2.36 (3H, s, C*H*$_3$CO) and 2.88 (2H, s, C*H*$_2$SCO).

[$Fe_2(CO)_5CH_3C(CH_2S)_2CH_2S$][Na] (9)

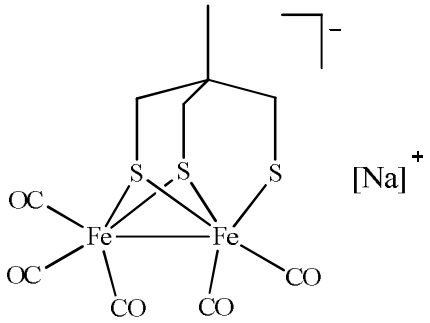

$Fe_2(CO)_6(CH_3C(CH_2S)_2CH_2SCOCH_3)$ (**8**) (12 mg, 0.25 mmol) was dissolved in freshly distilled methanol (10 mL). Sodium thiomethoxide (2.6 mg, 0.37 mmol) was added. The red-brown mixture was stirred in glove box for 90 minutes. CO and excess solvent were removed under vacuum to give a red-brown oil. υ_{max}/cm^{-1} (CO) 2028, 1961, and 1906 (methanol). This material was not further characterised (see below).

[$Fe_2(CO)_5CH_3C(CH_2S)_2CH_2S$][$PPh_4$] (10)

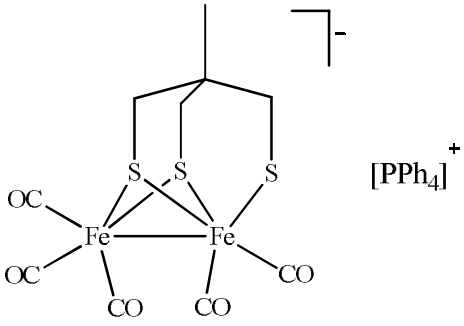

$Fe_2(CO)_6(CH_3C(CH_2S)_2CH_2SCOCH_3)$ (**8**) (30 mg, 0.62 mmol) was dissolved in freshly distilled methanol (10 mL). Sodium thiomethoxide, $NaSCH_3$ (6.5 mg, 0.92 mmol) was

added. The red-brown mixture was stirred in glove box for 90 minutes and tetraphenylphosphonium chloride (23 mg, 0.62 mmol) was added and stirred for further ten minutes. Methanol was removed under vacuum and product was extracted with tetrahydrofuran (10 mL) to give a red-brown oil. (Found C, 54.05; H, 3.93. $C_{34}H_{29}O_5Fe_2PS_3$, requires C, 53.99; H, 3.86%); υ_{max}/cm^{-1} (CO) 2027, 1961, and 1907 (methanol); (CO) 2016, 1950, 1898 (tetrahydrofuran). *m/z* 710 $(M)^+$, 371 $(M\text{-}P(Ph)_4)^+$.

$[Fe_2(CO)_4(CN)_2(CH_3C(CH_2S)_2CH_2SCOCH_3)][(Et_4N)_2]$ (11)

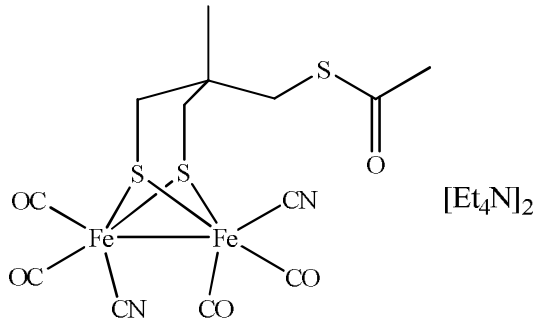

$Fe_2(CO)_6(CH_3C(CH_2S)_2CH_2SCOCH_3)$ (**8**) (56 mg, 0.12 mmol,) was dissolved in freshly distilled acetonitrile (5 mL) and cooled in ice bath. Tetraethylammonium cyanide (45 mg, 0.29 mmol) was added slowly and stirred under dinitrogen overnight. The red-brown mixture was concentrated under vacuum to give a red-brown oil. υ_{max}/cm^{-1} (CN) 2075 and 2038; υ_{max}/cm^{-1} (CO) 1961, 1924, 1884, 1873 and 1686 (acetonitrile). This material was used without further purification.

[$Fe_2(\mu\text{-}S_2)(CO)_6$] (12)

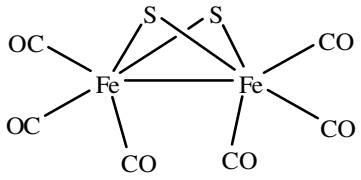

Iron pentacarbonyl (48.48 g, 250 mmol) was dissolved in freshly distilled methanol (200 mL) and cooled to 0 °C. Aqueous potassium hydroxide (50%, 80 mL) was added and solution was stirred under nitrogen flow for one hour. On the other hand, Na_2S_5 solution (416 mmol) was prepared by combining $Na_2S.9H_2O$ (100 g, 416 mmol), sulphur (55 g, 1.72 mol), aqueous KOH (50%, 10 mL) and distilled water (400 mL) and cooled to 0 °C. The deep red Na_2S_5 solution was poured into the vigorously stirred reaction solution. A mildly exothermic reaction resulted, with brisk CO evolution and formation of a dark red solution. The reaction mixture was stirred at 0 °C for 2 hours. A degassed solution of HCl: distilled water (37%, 200 mL: 200 mL) was added and leads to formation of brown precipitates. The brown solid was filtered, washed with distilled water (300 mL) and dried under vacuum overnight. It then was divided into three portions. Each portion was extracted twice by stirring for 15 minutes in pentane (600 mL). After combining the extracts, solvent was removed under vacuum, leaving a red-brown solid. This solid was a mixture of $Fe_2(\mu\text{-}S_2)(CO)_6$ and $Fe_3S_2(CO)_9$. Sublimation at 40 °C (0.1 mm) for 10 hours yielded $Fe_2(\mu\text{-}S_2)(CO)_6$ as a ruby-red solid, (10.33 g, 30 mmol, 24%). υ_{ma}/cm^{-1} (CO) 2074, 2034 and 1995 (toluene).

$[Fe_2(S_2C_3H_6)(CO)_6]$ (13)

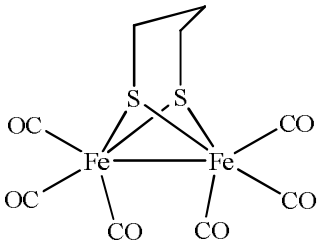

$Fe_3(CO)_{12}$ (1.50 g, 3.00 mmol) was dissolved in toluene (100 mL) under dinitrogen flow. 1,3-propanedithiol (0.35 g, 3.28 mmol) was added and the mixture was stirred at 80 °C for two hours until its colour changed from dark green to dark red. The reaction mixture was allowed to cool to room temperature and filtered. The red filtrate was concentrated under vacuum and was purified through flash chromatography (hexane) to give a red oil (1.05 g, 2.72 mmol, 91%). υ_{max}/cm^{-1} (CO) 2075, 2034 and 1997 (acetonitrile).

$[Fe_2(S_2C_3H_6)(CN)_2(CO)_4]$ $[(Et_4N)_2]$ (14)

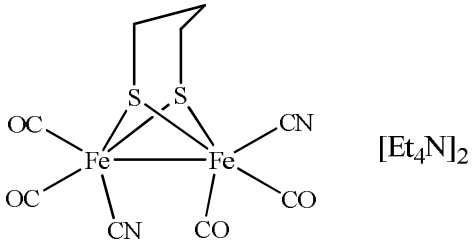

$Fe_2(S_2C_3H_6)(CO)_6$ (**13**) (1.00 g, 2.59 mmol) was dissolved in acetonitrile (20 mL) at 0 °C and was treated with a solution of Et_4NCN (0.80 g, 5.12 mmol) in acetonitrile (10 mL), and then the mixture was allowed to warm to room temperature. After one hour further, the resulting dark red solution was evaporated to dryness and washed with

hexane (2x10 mL) to give red oil (0.92 g, 1.63 mmol, 63%). υ_{max}/cm^{-1} (CO) 1961, 1917, 1880, and 1867; (CN) 2078 2029 (acetonitrile).

3-(pyrrol-1-yl)propyltriethylammonium tetrafluroborate (16)

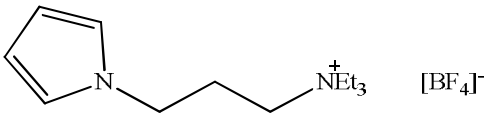

3-(pyrrol-1-yl)propyl bromide (**15**) (10.0 g, 53 mmol) was added to dry vigorously stirred ethanol, C_2H_5OH (10 mL). Triethylamine (7.0 g, 69 mmol) was added drop wise and the mixture was heated at 80 ºC under dinitrogen flow for overnight. Ethanol was removed under vacuum. The solid was dissolved in H_2O: C_2H_5OH (1: 1) and passed through an ion-exchange column in tetrafluroborate, BF_4^- form (Amberlite IRA). The eluate was taken to dryness under vacuum and the product was obtained as a pale-yellow oil (7.2 g, 72%). δ_H (400 MHz; solvent $CDCl_3$; standard $SiMe_4$) 1.02 (9H, m, NCH_2CH_3), 1.90 (2H, q, *J* 6.7, $C_4H_4NCH_2CH_2CH_2$), 2.70 (2H, t, *J* 6.7, CH_2NCH_2), 3.00 (6H, m, NCH_2CH_3), 3.97 (2H, t, *J* 6.7, $C_4H_4NCH_2CH_2$), 6.05 (2H, t, *J* 2.1, C(β)H pyrrole), 6.65 (2H, t, *J* 2.1, C(α)H pyrrole).

N,N'-bis(tert-butoxycarbonyl)-L-cystinyl-bis-N'',N''-dimethylaminoethylamide (17)

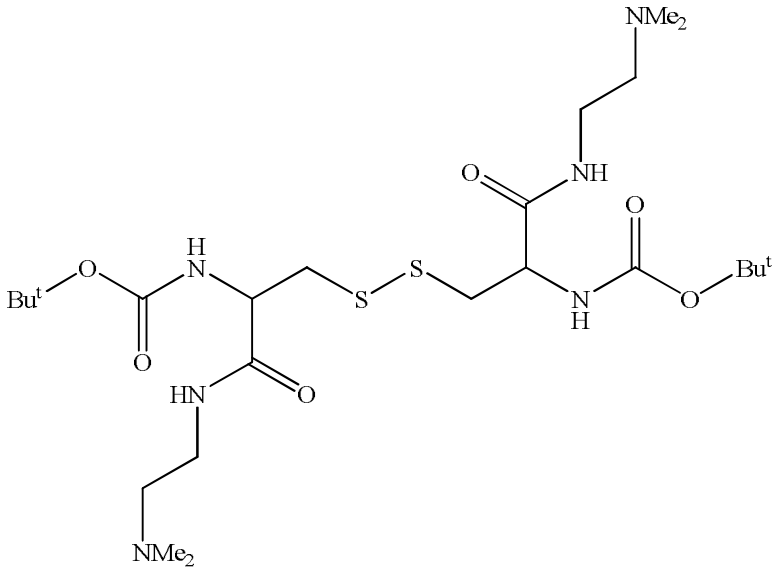

N,N'-bis(tert-butoxycarbonyl)-L-cysteine (3.60 g, 8.17 mmol) was dissolved in tetrahydrofuran (25 mL) under dinitrogen. 1,1-carbonyldiimidazaole (2.92 g, 18.0 mmol) was added portion and stirred for one hour at room temperature. 2-(dimethylamino)ethylamine (1.58 g, 18.0 mmol) was added and the mixture was stirred overnight under dinitrogen at room temperature. The mixture was heated at 60 °C for six hours, cooled to room temperature and concentrated by vacuum. The resultant solid was dissolved in dichloromethane (25 mL), the organic solution was washed with degassed water (2x20 mL) and then dried with $MgSO_4$ overnight. After evaporation of the solvent under vacuum, the resultant yellow solid was washed with diethyl ether (2x20 mL) to yield the pure product as a yellow solid (2.70 g, 75%). υ_{max}/cm^{-1} (N-H) 3348, (C=O urethane) 1705, (C=O amide) 1686 (KBr); δ_H (400 MHz; solvent $CDCl_3$; standard $SiMe_4$) 1.47 (9H, s, $C(CH_3)_3$), 2.24 (6H, s, $N(CH_3)_2$), 2.45 (2H, t,$CH_2CH_2N(CH_3)_2$), 2.70 (1H, d, N*H* urethane), 2.98 (2H, d, $CHCH_2S$), 3.36 (2H, m, $NHCH_2CH_2$), 4.70 (1H, d, $NHCH(CH_2S)CO$), 5.62 (1H, d, N*H* amide).

N-3-(pyrrol-1-yl)propanoic acid (19)

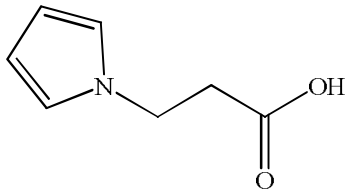

3-(pyrrol-1-yl)propiononitrile (**18**) (7.50 g, 125 mmol) was added to aqueous solution (50 mL) containing NaOH (10.0 g, 500 mmol). The mixture was refluxed for six hours and allowed to cool to room temperature. The flask and contents were placed in an ice bath and sulphuric acid (14.0 mL, 50%, 500 mmol) was added. The mixture separated with the product forming an upper oily phase. The product was extracted with diethyl ether (3x50 mL) and the extracts dried overnight with $MgSO_4$. Ether was removed under vacuum and the product was obtained as a pale yellow waxy solid (6.93 g, 92.4%). υ_{max}/cm^{-1} (O-H) 3267, (C=O) 1742, (C-O) 1286 (nujol); δ_H (400 MHz; solvent $CDCl_3$; standard $SiMe_4$) 2.83 (2H, t, *J* 6.9 Hz, NCH_2CH_2COOH), 4.20 (2H, t, *J* 7.3 Hz, CH_2COOH), 6.15 (2H, t, *J* 2.0, C(β)H pyrrole), 6.67 (2H, t, *J* 2.0, C(α)H pyrrole).

N,N'-bis[N-3-(pyrrol-1-yl)propanoyl]-L-cystinyl-bis-N",N" dimethylaminoethylamide (20)

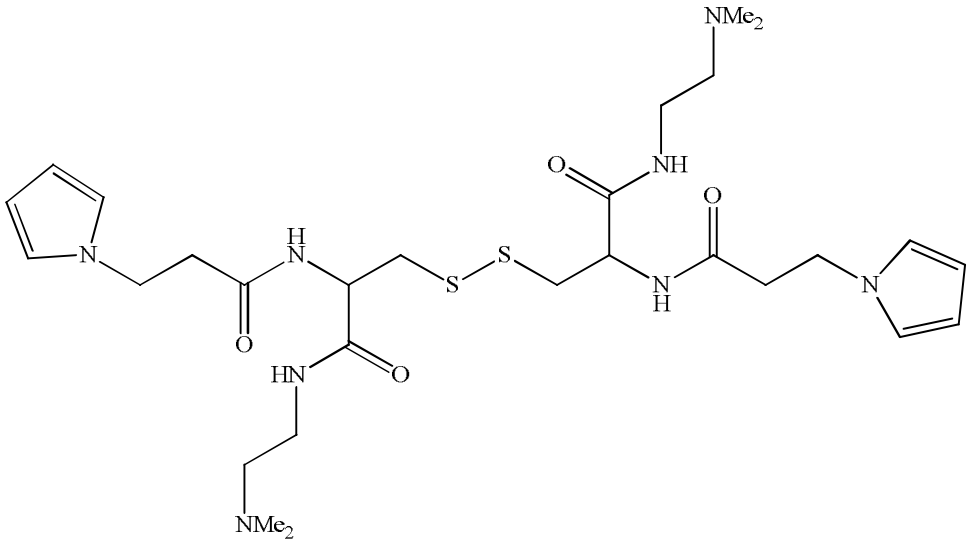

Trifluroacetic acid (37.23 g, 330 mmol) was added to **17** at - 10 °C and stirred for three hours at 0 °C. Solution was taken to dryness and washed with diethyl ether (3x50 mL). N-3-(pyrrol-1-yl) propanoic acid (**19**) (1.00 g, 7.00 mmol) was dissolved in dry tetrahydrofuran (10 mL) under dinitrogen. 1,1-carbonyldiimidazaole (1.30 g, 8.00 mmol) was added in portion and stirred for one hour at room temperature, and added into deprotected compound **17** solution. The mixture was stirred overnight under dinitrogen flow at room temperature and heated at 50 °C for five hours. The reaction mixture was cooled to room temperature and concentrated by vacuum. The resultant oily solid was dissolved in dichloromethane (20 mL), the organic solution washed with degassed water (2x20 mL) and then dried with $MgSO_4$. After evaporation of the solvent under vacuum, the resultant pale yellow solid was washed with diethyl ether (2x20 mL) to yield the pure product as a pale yellow solid (1.22 g, 45%). υ_{max}/cm^{-1} (N-H) 3302, (C=O amide) 1634, (N-H amide) 1525, (C-H pyrrole) 721 (KBr); δ_H (400 MHz; solvent $CDCl_3$; standard $SiMe_4$) 2.24 (6H, s, $N(CH_3)_2$), 2.42 (2H, m,$CH_2CH_2N(CH_3)_2$), 2.69 (2H, t, CH_2CH_2CO), 2.96 (2H, m, $CHCH_2S$), 3.30 (2H, m, $NHCH_2CH_2$), 4.20 (2H, t,

NC*H*$_2$CH$_2$), 4.99 (1H, m, NHC*H*(CH$_2$S)CO), 6.07 (2H, t, *J* 2.1, C(β)H pyrrole), 6.63 (2H, t, *J* 2.1, C(α)H pyrrole), 7.02 (1H, d, N*H*(CO)CH), 7.35 (1H, b, N*H*(CO)CH$_2$).

N,N'-bis[N-3-(pyrrol-1-yl)propanoyl]-L-cystinyl-bis-N'',N'' trimethylammoniumethylamide tetrafluroborate (21)

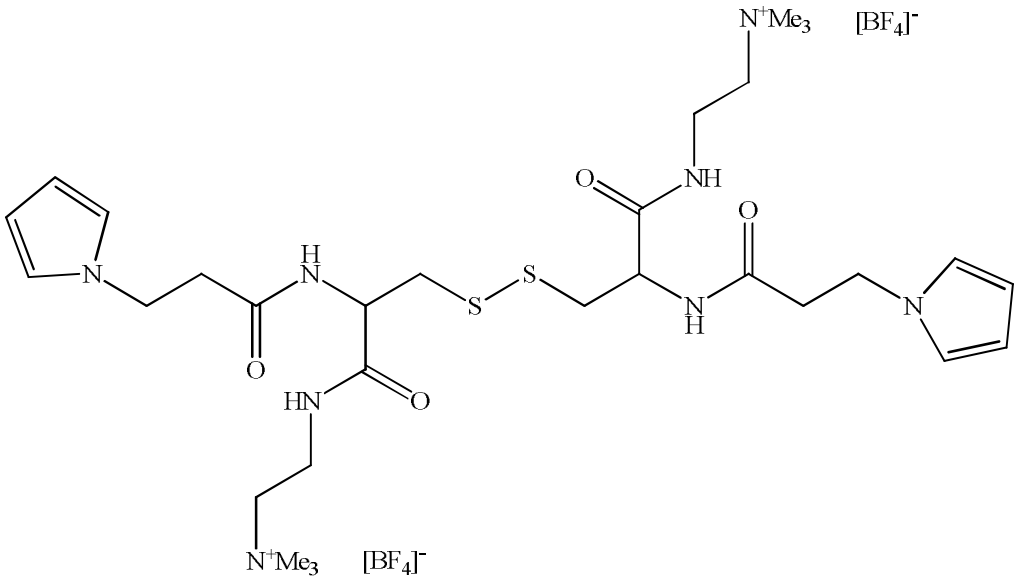

N,N'-bis[N-3-(pyrrol-1-yl)propanoyl]-L-cystinyl-bis-N'',N''-dimethylaminoethylamide (**20**) (0.40 g, 0.64 mmol) was dissolved in dry acetonitrile (20 mL) and cooled to 4°C. Trimethyloxonium tetrafluroborate, [(CH$_3$)$_3$O][BF$_4$] (0.28 g, 193 mmol) was added into the solution and stirred for 90 minutes at room temperature under nitrogen stream. The mixture was concentrated under vacuum and washed with diethyl ether (3x20 mL) to yield the pure product as a pale yellow solid (0.28 g, 70%). υ_{max}/cm^{-1} (N-H) 3300 and 3350, (C=O amide) 1665, (N-H amide) 1530, (B-F) 1070, (C-H pyrrole) 730 (nujol); δ_H (400 MHz; solvent CDCl$_3$; standard SiMe$_4$) 2.69 (2H, t, CH$_2$C*H*$_2$CO), 2.93 (2H, m, CHC*H*$_2$S), 3.03 (9H, s, CH$_2$N$^+$(C*H*$_3$)$_3$), 3.30 (2H, t, C*H*$_2$N$^+$(CH$_3$)$_3$), 3.54 (2H, m, NHC*H*$_2$CH$_2$), 4.16 (2H, t, NC*H*$_2$CH$_2$), 4.55 (1H, m, NHC*H*(CH$_2$S)CO), 6.02 (2H, t, *J*

2.1, C(β)H pyrrole), 6.65 (2H, t, *J* 2.1, C(α)H pyrrole), 7.02 (1H, b, N*H*(CO)CH), 7.15 (1H, b, N*H*(CO)CH_2).

Chapter 4

Electropolymer Materials Possessing Assemblies related to the Active Site of [FeFe]-hydrogenase

Introduction on Hydrogen Fuel Produces Cells and Artificial Hydrogenase System

4.1 Fuel producers cells: Role in hydrogen economy

The concept of the fuel cell can be traced back to 19th century commencing with an independent study by Grove [147] and Schoenbein. [148] The principle of fuel cells is rather similar to batteries, in the sense that electrical energy is generated by conversion of chemical energy through electrochemical reaction at anode and cathode electrodes. [149, 150] Fuel cells are remarkably efficient in converting hydrogen to water and electrical energy, and significant advances have been made in fuel cell technology, particularly the polymer electrolyte membrane (PEM). [151, 152]

Molecular hydrogen is a valuable fuel which can be stored in large quantities in pressurised vessels. With the development of more efficient fuel cells, molecular hydrogen is emerging as a true alternative to fossil fuels and as the energy carrier of the future. The challenge of building of an electrode assembly capable of performing dihydrogen evolution/uptake is particularly attractive in the context of electrocatalysts for hydrogen fuel cells, which are critical to the development of the hydrogen economy. [7] **Scheme 4.1** demonstrates a schematic representation of a H_2/O_2 fuel cell.

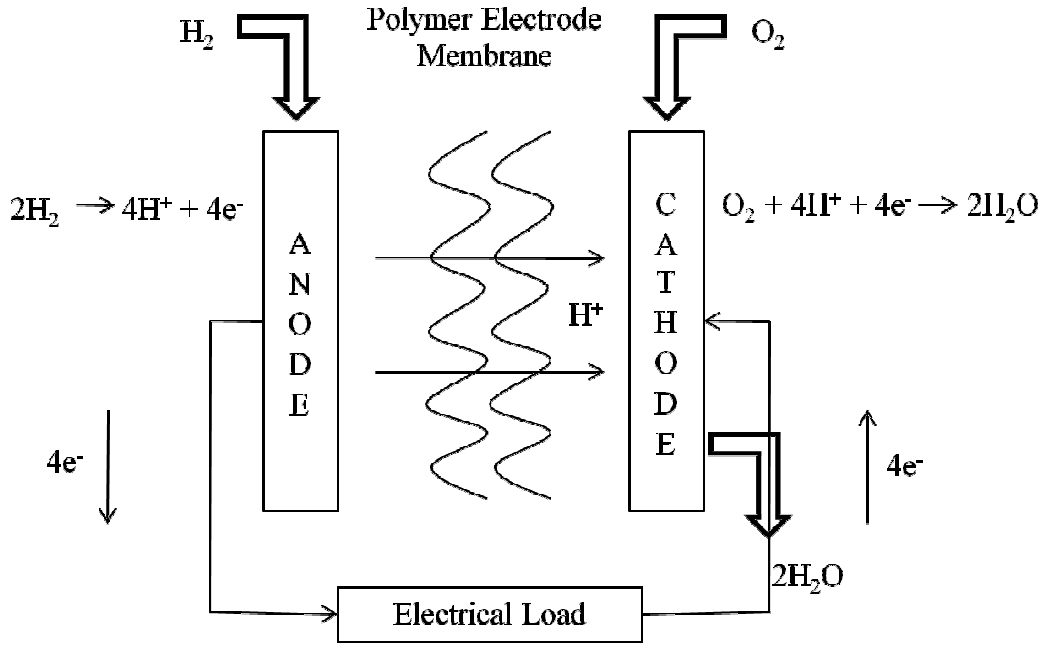

Scheme 4.1. Schematic representation of a H_2/O_2 fuel cell.

Nevertheless, some issues remain as fuel cells are currently expensive, impurities in the gas stream shorten the life of the fuel cells, and they have limited availability and low durability. The commercial potential of fuel cells depends in part on the ability to reduce the cost of expensive catalysts, for example platinum-based materials, which are currently the most favoured electrocatalyst for dihydrogen oxidation and dioxygen reduction. Widespread use and commercialisation will, however, require improvements in fuel cell lifetime and durability, which are also directly related to overall costs.

4.2 Electrocatalysts: Replacing platinum

The basic reaction of a H_2/O_2 fuel cell is described by **Equation4.1**.

$$H_2 + \frac{1}{2}O_2 \rightleftharpoons H_2O \qquad \Delta H^{\circ} = -285.15\ kJ.mol^{-1} \qquad \textbf{Equation 4.1}$$

The chemical energy (H_2 and O_2) is converted into electrical energy by controlled electrochemical reactions at each electrode of the cell. As mentioned earlier, the best catalysts to catalyse the reaction in **Eq. 4.1** is platinum metal. Up to early this year, the price for platinum was USD 1650 per ounce. Thus, the design of material not based on precious metals would be a major step toward the use of dihydrogen as a fuel. Enzyme fuel cells uses an enzyme as the electrocatalysts, either at both cathode and anode, or one of them, would be the key answer to resolve this grand chemistry challenge. Many enzymes are now proven to be extremely good electrocatalysts. [10-12] Along with very high turnover rates driven by minimal overpotential, their specificity renders them suited for miniature, membraneless fuel cells that can produce electrical power from a fuel/oxidant mixture. [153]

[FeFe]-hydrogenase can perform the dihydrogen uptake/evolution reaction as efficiently as platinum but with just iron, inorganic sulphur, thiolates, CO and CN^- ligands. As for noble metals like platinum, the enzyme is able to stabilise the transition state of the catalytic cycle and therefore lowers the energy required to drive that reaction in the desired direction.

Building a surface modified electrode could allow the introduction of our model complexes onto an electrode, providing a reasonably cheap material capable of dihydrogen evolution/uptake by heterogeneous catalysis.

4.3 Bioinspired and bioinorganic electrocatalysts

Nature has developed its own set of catalysts to produce hydrogen or to utilise it as an energy source-the hydrogenases. Many of the catalysts used for anthropogenic production and utilisation of hydrogen involve precious metals such as platinum.

However, the situation continues to improve as new catalysts, including biomimetic systems, are being developed.

Understanding the basic processes of photosynthesis and chemical conversion may enable scientists to create systems that mimic biomolecules and produce energy more efficiently. Much work has been conducted in the development of artificial reaction centres catalysing the formation of molecular hydrogen from protons. Recently, Artero and his co-workers have reported nickel bisdiphospines, which mimic the active site of hydrogenase, were covalently attached to carbon nano tubes and exhibit dihydrogen evolution from aqueous sulphuric acid at a very low overpotential (20 mV). [154]

To date, a vast number of synthetic diiron dithiolate and related systems attributed as models of structural and functional aspects of the active site of the [FeFe]-hydrogenase, have been synthesised and characterised, including the first ever artificial H-cluster. [109] Nevertheless, it was found that all synthetic electrocatalytic assemblies are energetically rather than kinetically inefficient, in that they function at overpotentials far removed from the potential of the H^+/H_2 system on Pt, under the same conditions. [123, 125, 155] Building artificial centres more closely related to the enzyme might overcome this problem. Furthermore, if such assemblies are incorporated in an electropolymer framework, then we may achieve the construction of solid state materials for electrocatalysis of molecular hydrogen evolution or uptake.

Incorporating synthetic analogues of the catalytic machinery of [FeFe]-hydrogenase within an electropolymer presents a greater challenge, but one which might afford new electrode materials for electrocatalysis of dihydrogen uptake/evolution. This is particularly attractive if catalysis can be matched to the conducting regime of the

supporting polymer or fast electron transfer relays are co-incorporated. Presented in this chapter are some first steps in this direction. We first describe the incorporation of a sub-site model within an electropolymeric framework and we show that this can stabilise the hydride intermediate. We then describe the building of an H-cluster within an electropolymer by modification of the {4Fe-4S} cluster site.

4.4 Modification of electrode surfaces

Anchoring organic and organometallic systems to electrodes began some 40 years ago even before Mosses *et al.* introduced the term "chemically modified electrodes" to describe electrodes that had foreign molecules deliberately immobilised on their surfaces, in 1975. [156] Indeed, the first example of surface electrode reaction experiments are the olefinic functional group studies through absorption of different organic compounds on platinum by Lane and Hubbard. [157] Researches on such modified electrodes have been expanding rapidly since then, and these modifications are now being performed by adsorption, as well as by chemical or covalent bonding.

4.5 Poly(pyrroles) and other conducting polymers

A very significant area of research of modified electrode is the electropolymerisation of pyrrole or thiophene monomers on conducting surfaces. These produce polymer film which can be conducting in their oxidised ("doped" state) and the neutral state ("undoped"). Interest in modifying electrodes with polymeric films has recently been reported by many workers. Moutet and his co-workers demonstrated Pd nano-particles can be incorporated onto electrodes pre-modified with poly(pyrrole alkylammonium) matrix. [158]

The work reported here will apply an electropolymerisation technique which produces films containing electronic states. These states are capable of being oxidised and reduced, thereby allowing an electron to hop through the film. The electroactivity of the electrode material is usually not destroyed by these films, although some small hindrances of electron transfer have been noted. Polymer films formed with this procedure have also been observed to retain their own chemical behaviour, such as catalytic properties, when immobilised on the surface. [159]

The functionalisation of poly(pyrrole) has been shown in the lab to be a successful method to introduce iron-sulphur analogues into an electropolymer. [146, 160] Synthesis of cysteinyl-pyrrole derivatives, followed by oxidative polymerisation, led to the formation of an electropolymer with functional thiol groups. Exchange reaction occurs with $\{Fe_4S_4\}$ clusters and incorporation of cubanes into the polymer framework can be characterised by using electrochemical technique.

The study presented here is indeed an extension from this work; we can envisage their modification, using the chemistry we have described, thereby providing a route to advanced electrode materials.

4.6 The poly(pyrrole) framework

Most polymers are unable to carry electricity and their insulating properties have been extensively applied, notably with plastics (*e.g.* the insulating polymer around electrical wire). However, during the past two decades, a new class of organic polymers has been developed and exhibits remarkable conducting properties. Their alternate structures of π-conjugated systems and double bonds along the polymeric chain give them

interesting electrical properties. Polymerisation occurs by electrochemical oxidation at potentials that form free radicals.

Poly(pyrrole) is a conductive polymer due to hopping of electrons through the polymer. Chemical oxidation of pyrroles leads to fine poly(pyrrole) powders, but electrochemical oxidation provides free-standing poly(pyrrole) films (**Scheme 4.2**). These radicals are adsorbed on the electrode surface and multiple rearrangements lead to the polymer network. The growth of this polymer depends on its electrical character, and the growth of conductive polymers is virtually unlimited. The electrode potential and the reaction time allow the control of the thickness of the film and can be generated by cycling the potential or using a fixed potential. [161] Most conducting materials can be coated in this way. In the "doped", that is the oxidised state, the poly(pyrroles) is conducting. In the "undoped" neutral state, it is not insulating. However, the presence of redox group within an "undoped" film can allow rapid charge transport by electron hopping.

Recent works have shown that amino acid or small peptide fragments can be attached to the 1- or 3-positions of pyrrole and from these monomers, electrode bound polymeric films can be produced allowing the possibility of creating electrode structures with oligopeptide chains, that are capable of binding prosthetic groups or metallo-cofactors, offering biocompatible interfaces which can interact with proteins or enzymes. [146, 162-164]

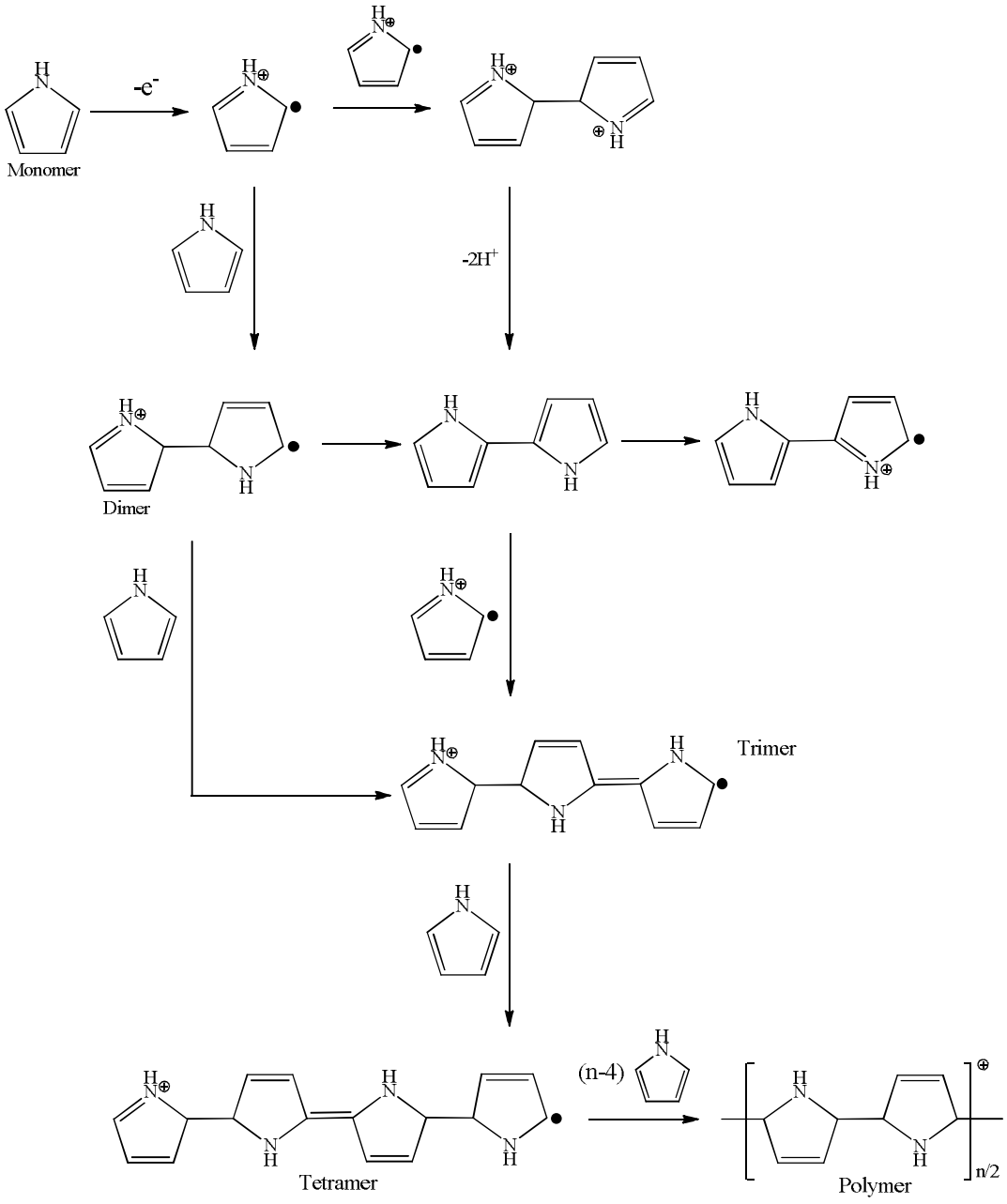

Scheme 4.2. Scheme of the radical polymerisation of a pyrrole monomer (adapted from reference [161]).

4.7 Background work on a protonation of sub-site analogue

As discussed in **Chapter 2**, shortly after the report on the structure of [FeFe]-hydrogenase, [47, 48] three research groups independently reported the synthesis of the propanedithiolate complex $[Fe_2(S_2C_3H_6)(CO)_4(CN)_2]^{2-}$as a CO inhibited model for the diiron sub-site. [89, 90, 93] Pickett and co-workers further noted that this dianion is soluble and stable in water, although it does not catalyse electrochemical proton reduction in aqueous electrolyte ($4.0 < pH < 8.4$). [110] More interestingly, Rauchfuss and co-workers reported that the dicyanide species reacts readily with protons in organic solvent to afford some molecular H_2 and insoluble material, [89] while Darensbourg and co-workers observed a transiently stable bridging hydride species $[(\mu\text{-H})Fe_2(S_2C_3H_6)(CO)_4(CN)_2]^{2-}$ under similar experimental conditions. [122]

No spectroscopic data has established the presence of a hydride species during the catalytic mechanism of dihydrogen evolution/uptake of hydrogenases, but the formation of proton deuterium (HD) during the turnover under hydrogen isotopes, deuterium (D_2) [8] suggests the possibility that formation of a metal-hydride can occur. This proposal is also supported by density functional theory (DFT) studies. [165, 166]

As discussed previously, presence of a hydride intermediates during turnover in either direction, oxidation of H_2 or proton reduction is a fundamental step in molecular hydrogen evolution at the diiron sub-site of [FeFe]-hydrogenase. Attempts to obtain a hydride complex with a {2Fe-2S} core have resulted in the characterisation of many bridging hydride species with CO and phosphine ligands or other donor ligands. [92, 122] A complex with both bridging and terminal hydride has also been synthesised with ruthenium atoms instead of iron by photolytic activation of $Ru_2(CO)_4(PCy_3)_2(pdt)$ under a dihydrogen atmosphere. [167] It has also been shown in that study that dihydrogen

can be generated after reaction with hydrochloric acid, HCl. Rauchfuss has also crystallographically characterised a terminal hydride diiron complex synthesised indirectly. [168]

Most protonation studies have been synthetically driven and protonation conditions chosen to effect reaction and allow spectroscopic and or crystallographic characterisation. Such protonation could take place in a terminal fashion at a single Fe or by bridging between two Fe centres, the apical bridgehead NH or cyanide ligands. [92] In synthetic complexes, all these types of interaction have been recognised, singly or in combination.

Studies on the reactivity of the $[Fe_2(S_2C_3H_6)(CO)_4(CN)_2]^{2-}$complex is hindered by the degradation of the protonation products, which have a limited lifetime. [122, 169, 170] The formation of insoluble oligomers may contribute to these degradations. The presence of cyanide ligands in the natural sub-site suggest that these pathways must be inhibited either by the exact nature of the sub-site itself or by the surrounding enzyme scaffold. Immobilisation of sub-site centres in a polymer matrix might be expected to stabilise protonated species by preventing bimolecular metal centre interactions, somewhat akin to the protection of the natural sub-site in its protein scaffold. [163] Here we describe how incorporation of this dianion within a polymer matrix allows stabilisation of the hydride intermediate.

4.8 Results and Discussion

4.8.1 Formation of an ionic exchange polymer: Electropolymerisation of 3-(pyrrol-1-yl)propyltriethylammonium tetrafluroborate

3-(pyrrol-1-yl)propyltriethylammonium tetrafluroborate (**16**) was polymerised on surface electrode at ambient temperature by cycling the potential between -0.10 V to +1.20 V *versus* SCE at 50 $mV.s^{-1}$. Thin-films were grown on the polished platinum disc and were in golden-yellow colour (**Figure 4.1**).

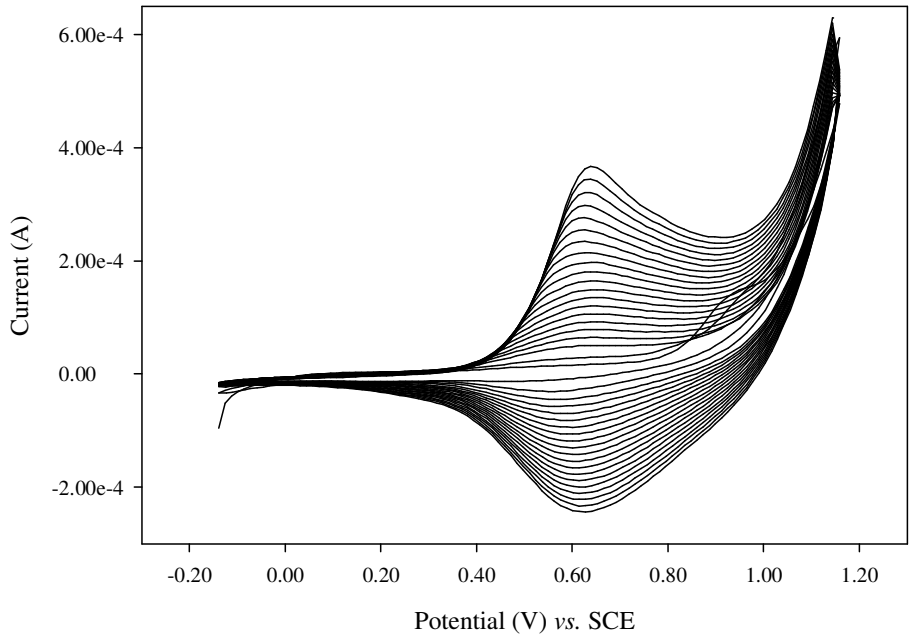

Figure 4.1. Film growth of poly (**16**) (10 mM, 0.2 M $[NBu_4][BF_4]$ in acetonitrile, 50 $mV.s^{-1}$) on Pt disc electrode by repetitive scanning (20 cycles).

4.8.2 Stabilisation of a protonated sub-site: Trapping a dicyanide sub-site within an electropolymer matrix by ion exchange

The synthesis of $[Fe_2(S_2C_3H_6)(CO)_4(CN)_2][Et_4N]_2$ (**14**) diiron complex which matches the major geometrical features of the available [FeFe]-hydrogenase active site structures and demonstrates Fe(I)-Fe(I) oxidation states has been discussed previously (see **Chapter 3**). The modified electrode was taken into glove box ($O_2 < 0.1$ ppm) and soaked into a prepared solution of $[Fe_2(S_2C_3H_6)(CO)_4(CN)_2]^{2-}$ (5 mM-CH_3CN) for 15 minutes to allow the dicyanide sub-site to exchange with the BF_4^- within the polymer framework. The electrode was washed with acetonitrile, and examined by FTIR in inert atmosphere as the sub-site is highly sensitive to air.

Figure 4.2 displays the corresponding spectra which confirmed with the presence of $Fe_2(S_2C_3H_6)(CO)_4(CN)_2]^{2-}$ on the polymer framework where 2074 cm^{-1} is assigned to CN^- band, and 1960, 1917, 1878 and 1865 cm^{-1} arise from the terminal CO bands.

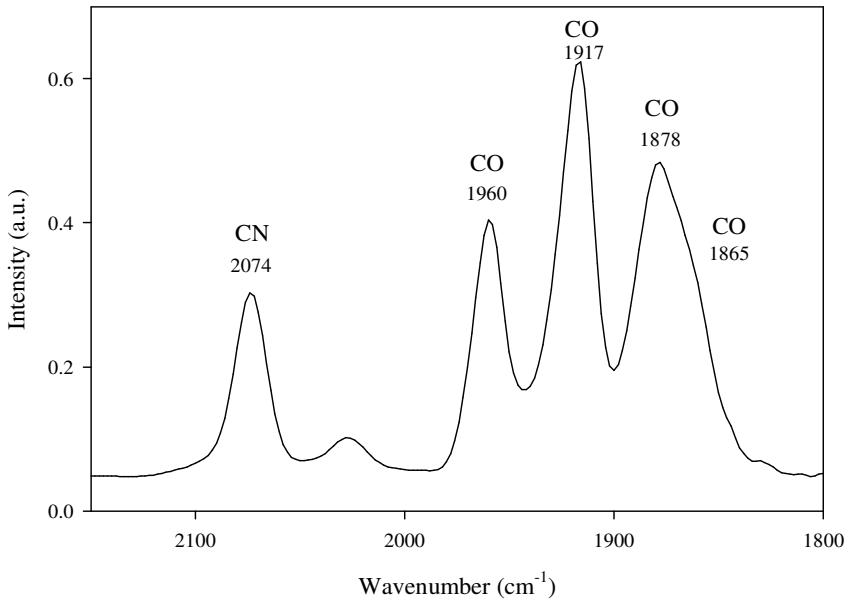

Figure 4.2. FTIR spectrum of $[Fe_2(S_2C_3H_6)(CO)_4(CN)_2]^{2-}$ (**14**) bound within poly (**16**).

To compare the behaviour of complex **14** in solid state and in solution, the infrared spectra of complex **14** itself in acetonitrile was taken **(Figure 4.3)**. It was noticed that both the spectrum recorded either *via* solid state or in solution share the same spectra patterns. However, there are slight difference in the υ(CO) and υ(CN) bands which differs about two to four cm^{-1}, respectively.

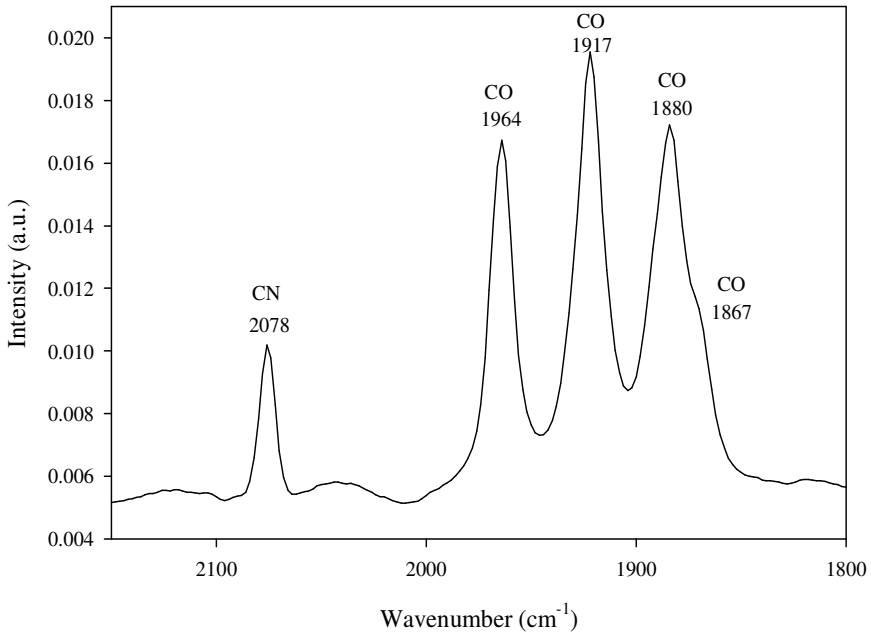

Figure 4.3. FTIR spectra recorded for $[Fe_2(S_2C_3H_6)(CO)_4(CN)_2]^{2-}$(**14**) in acetonitrile solution.

After the spectra was recorded, the modified electrode was taken back into glove box and was exposed to the vapour above a vessel containing concentrated hydrochloric acid for ten seconds period. After each exposure, a reflectance FTIR was taken of the surface. No further change was observed after the fourth exposure (40 seconds total time). **Figure 4.4** displays the infrared spectra of the complex **14** as it is transformed by the gaseous acid. Significant changes were monitored when the film was exposed for a second time to HCl vapour. Thus the parent complex peaks assigned to υ(CN) and

υ(CO) are diminished, and the formation of new peaks at more positive frequency range are observed. Thus there is a positive shift of υ(CO) from 1878, 1917 and 1960 cm^{-1} to 1980, 2021 and 2045 cm^{-1}, respectively while υ(CN) value shifts from 2074 cm^{-1} to 2105 cm^{-1}, consistent with the formation of an hydride.

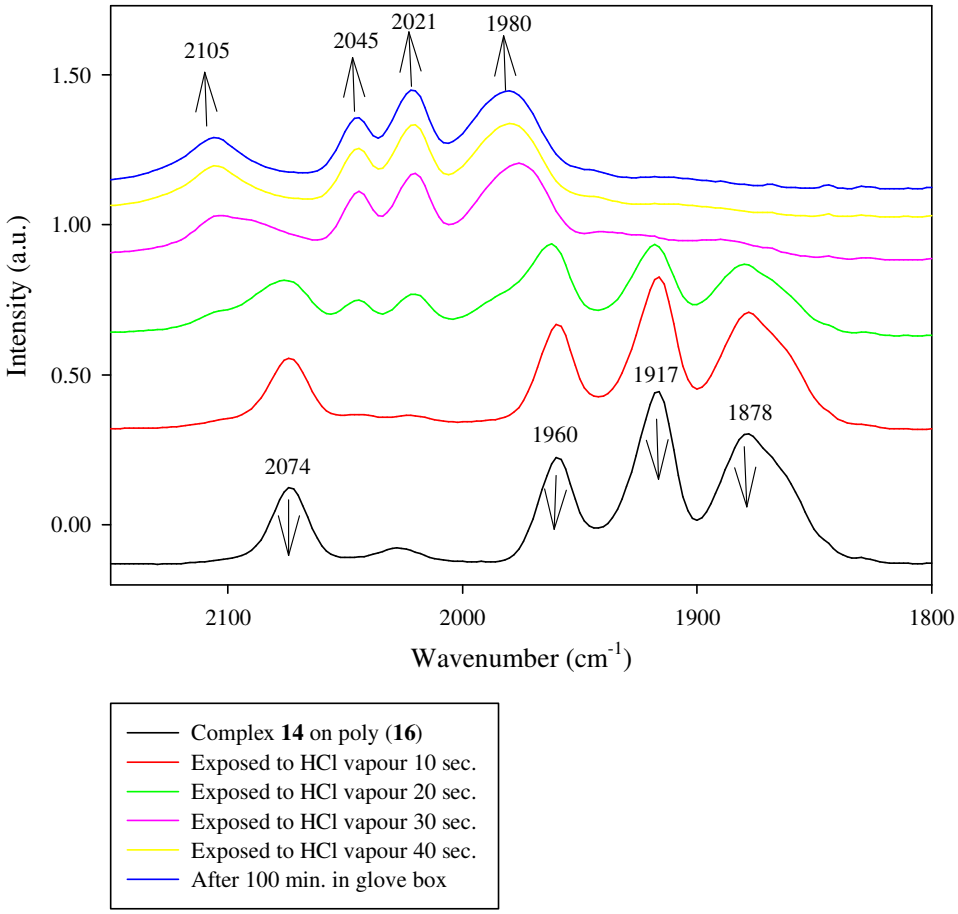

Figure 4.4. FTIR spectrum indicates changes of IR bands for complex $[Fe_2(S_2C_3H_6)(CO)_4(CN)_2]^{2-}$ (**14**) during protonation.

Based on the work recently reported by the group, [169, 170] which use a combination of stopped-flow spectroscopies and NMR measurements to study the protonation mechanism of the same dicyanide complex (**14**) in solution, we suggest that in the polymer, protonation occurs at the metal-metal bond. Comparison to the spectrum for

the reaction of complex (**14**) with $HBF_4{\cdot}Et_2O$ as proton source in acetonitrile solution with our findings clearly showed that the same product had formed (**Figure 4.5**), which is the bridging hydride as displayed in **Scheme 4.3**.

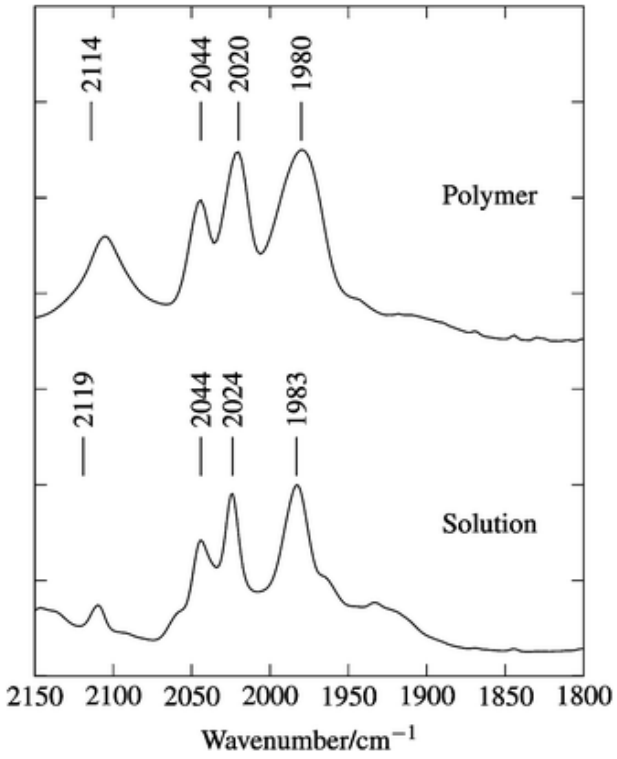

Figure 4.5. Spectra for products of protonation of $[Fe_2(S_2C_3H_6)(CO)_4(CN)_2]^{2-}$ (**14**) by $HBF_4{\cdot}Et_2O$ in acetonitrile solution (bottom, $[(\mathbf{14})]_0$ = 0.50 mM, $[HBF_4{\cdot}Et_2O]_0$ = 1.13 mM) and by HCl vapour in the polymer (top).

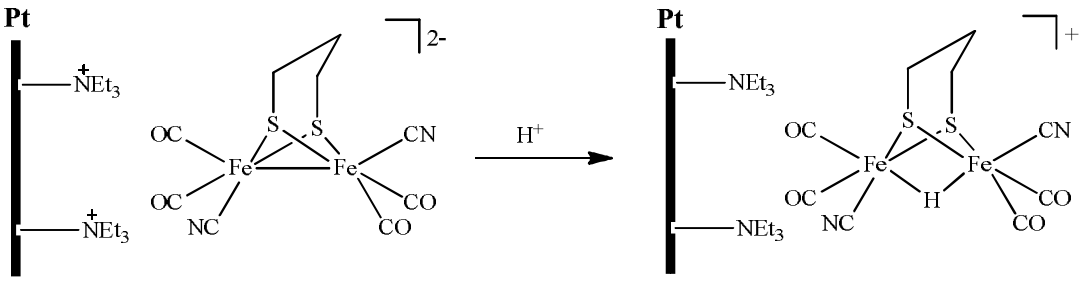

Scheme 4.3. Schematic diagram on protonation process of $Fe_2(S_2C_3H_6)(CO)_4(CN)_2]^{2-}$ (**14**) bounded within poly (**16**).

Continued exposure of the surface film to acid vapours led to no further change in the observed spectrum, which was stable for several hours. This is in marked contrast to the solution reaction, where rapid degradation of the product is seen with excess acid and after standing for minutes. [122] In contrast to the solution reaction, there was no evidence for an intermediate in the protonation reaction when carried out in the polymer. The lack of degradation of the protonated product on exposure to additional HCl, and the overall clean nature of the product spectrum suggest that the reaction in the polymer is more controlled than that in solution. While a pathway involving a cyanide protonation cannot be ruled out, the presence of the polymer scaffold clearly contributes to the stability of the protonated sub-site.

4.9 Assembling of an H-cluster analogue on an electrode surface

Studies of electropolymerisation and the generation of an H-cluster type assembly in an electropolymers are now described. It is worth noting that, up to now, very few detailed electrochemical studies of diiron dithiolate systems on surface of electrodes have been developed. One of the most important challenges, which would allow new insights into mechanisms of production of H_2 by hydrogenase, is now to study new generations of solid state materials in which the key features of the sub-site of all-iron hydrogenase or of the H-cluster have been retained in an artificial matrix. [86]

4.9.1 Results and Discussion

4.9.1.1 Constructing inorganic polyferredoxin on electrode:

Electropolymerisation of N,N'-bis[N-3-(pyrrol-1-yl)propanoyl]-L-cystinyl-bis-N",N"-trimethylammoniumethylamide [BF_4] salt (21)

Monomer N,N'-bis[N-3-(pyrrol-1-yl)propanoyl]-L-cystinyl-bis-N",N"-trimethylammoniumethylamide [BF_4] salt (**21**) was polymerised on surface electrode at ambient temperature, by cycling the potential between -0.10 V to +1.20 V *vs.* SCE at 50 $mV.s^{-1}$ to give conducting films, which are golden yellow in the reduced state. **Figure 4.6** depicts the growth of the film formed by monomer **21** after repetitive cycling on the applied potential. As we acknowledged, when the pyrrole-cystine monomer (**21**) is oxidised, the radical cation of this monomer is formed and reacts with other monomers present in solution to form oligomeric products and then the polymer. The anion, [BF_4^-] is incorporated into the polymer to ensure the electrical neutrality of the film and, at the end of the reaction, a polymeric film of controllable thickness is formed. The characteristic of the film was monitored with reflectance FTIR, where the spectra shows bands at υ_{max}/cm^{-1} (N-H) 3300 and 3350, (C=O amide) 1665, (N-H amide) 1530, (B-F) 1070, (C-H pyrrole) 730, indicating the presence of the film (**Figure 4.7**).

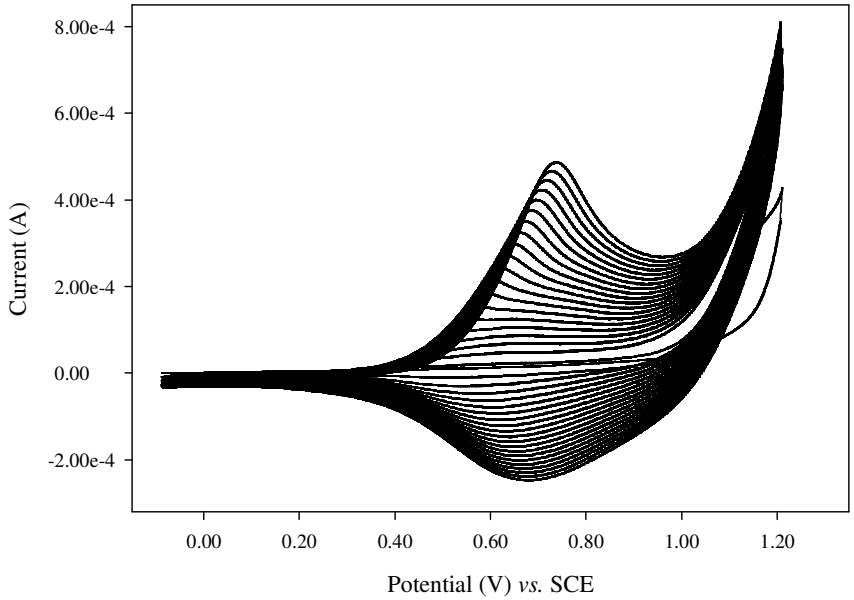

Figure 4.6. Film growth of poly (**21**) (8 mM, 0.2 M $[NBu_4][BF_4]$ in acetonitrile, 50 $mV.s^{-1}$) on Pt disc electrode by repetitive scanning (20 cycles).

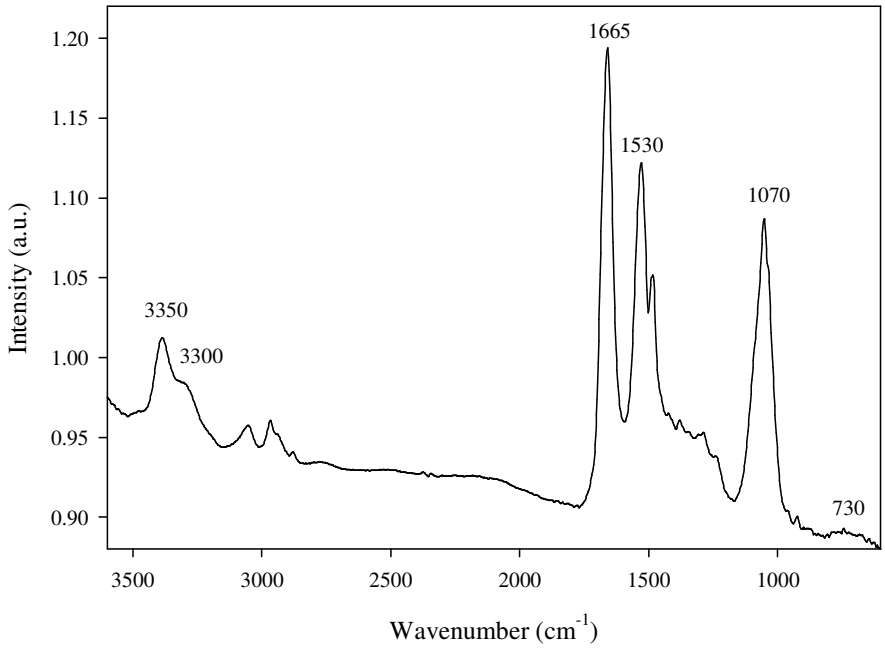

Figure 4.7. FTIR spectra of poly (**21**).

The resulted pyrrole-cystine films are readily converted to cysteinyl states which ligate $\{Fe_4S_4\}^{2+}$ cluster centres. The cluster synthesis, $[Fe_4S_4(SPh)_4][NBu_4]_2$ (**1**) is described previously (see **Chapter 3**).

4.9.1.2 Incorporation $\{Fe_4S_4\}$ cluster in the polymer

The S-S bonds in thin-films produced by electropolymerisation of monomer **21** were reduced to give a cysteinyl apo-polymer (**22**) by soaking the electrode into Cleland's reagent which contains potassium *tert*-butoxide (*t*-BuOK) and DL-dithiothreitol (DTT). This apo-polymer incorporates cluster centres by thiolate ligand-exchange on exposure to solutions of $[Fe_4S_4(SPh)_4]^{2-}$ (**1**) (5 mM-CH_3CN). Each Fe atom of the cluster is ligated by a thiolate ligand from the polymer (**21**). Details of this process are shown in **Scheme 4.4**.

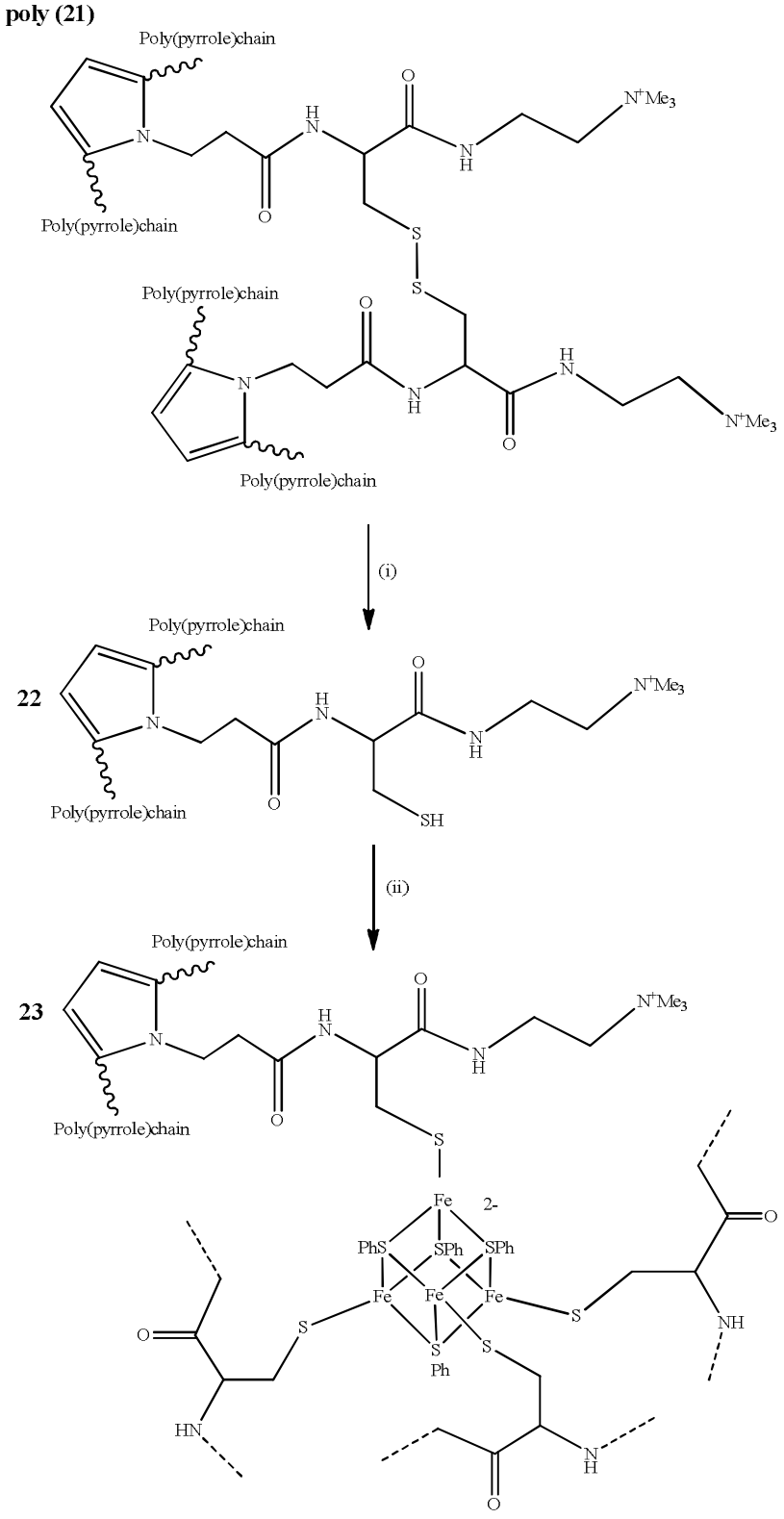

Scheme 4.4. Incorporation of $\{Fe_4S_4\}^{2+}$ cluster centres onto poly (**21**, cysteinyl form) film on Pt disc electrode. (i) DTT, *t*-BuOK, CH_3OH, CH_3CN; (ii) 5 mM $[Fe_4S_4(SPh)_4][NBu_4]_2$, CH_3CN.

Figure 4.8 displays the well defined and stable redox response for the reversible reduction of the bound $\{Fe_4S_4\}^{2+}$ cluster in poly (**21**, cysteinyl form). The voltammogram at this stage was recorded in a glove box (O_2< 0.1 ppm), using an Autolab PGSTAT 30 with GPES version 4.9 software. The one-electron reversible reduction for the bound cluster occurs at $E_{1/2}$ = -0.96 V *vs.* SCE and corresponds to the $\{Fe_4S_4\}^{2+}/\{Fe_4S_4\}^{+}$ couple with peaks separation being nearly zero. It is always preferable to scan at lower scan rates, in order to allow more time for the electron hopping process along the polyferredoxin framework with the cluster.

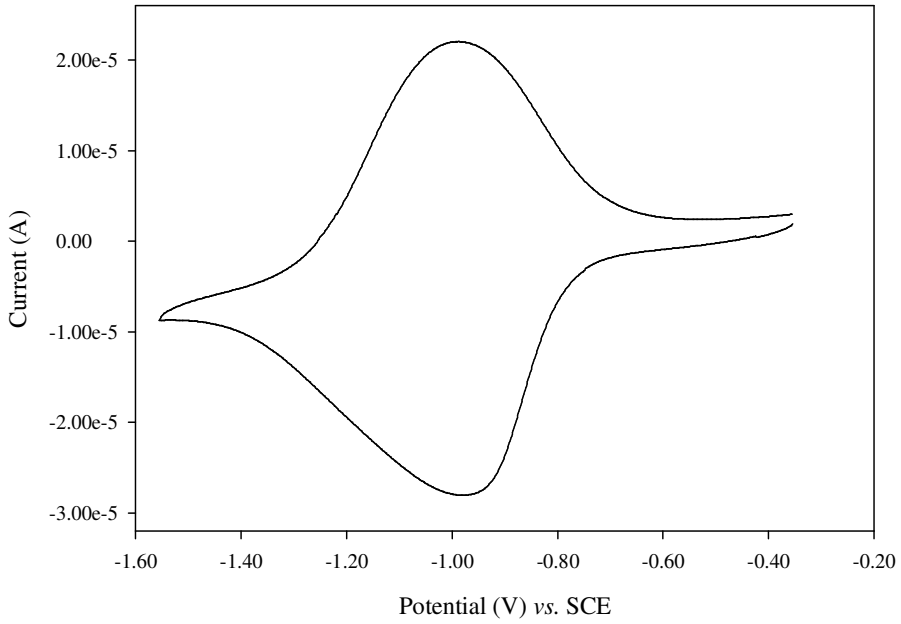

Figure 4.8. Cyclic voltammogram of $\{Fe_4S_4\}^{2+/1+}$ couple confined in poly (**21,** cysteinyl form) film on Pt disc electrode (0.2 M $[NBu_4][BF_4]$ in acetonitrile, 5 $mV.s^{-1}$).

From **Figure 4.9**, there is a linear relationship between the peak current and potential scan rate which is consistent with a polymer confined couple. The small potential difference, ΔE (less than 10 mV) at lower scan rates, is also consistent.

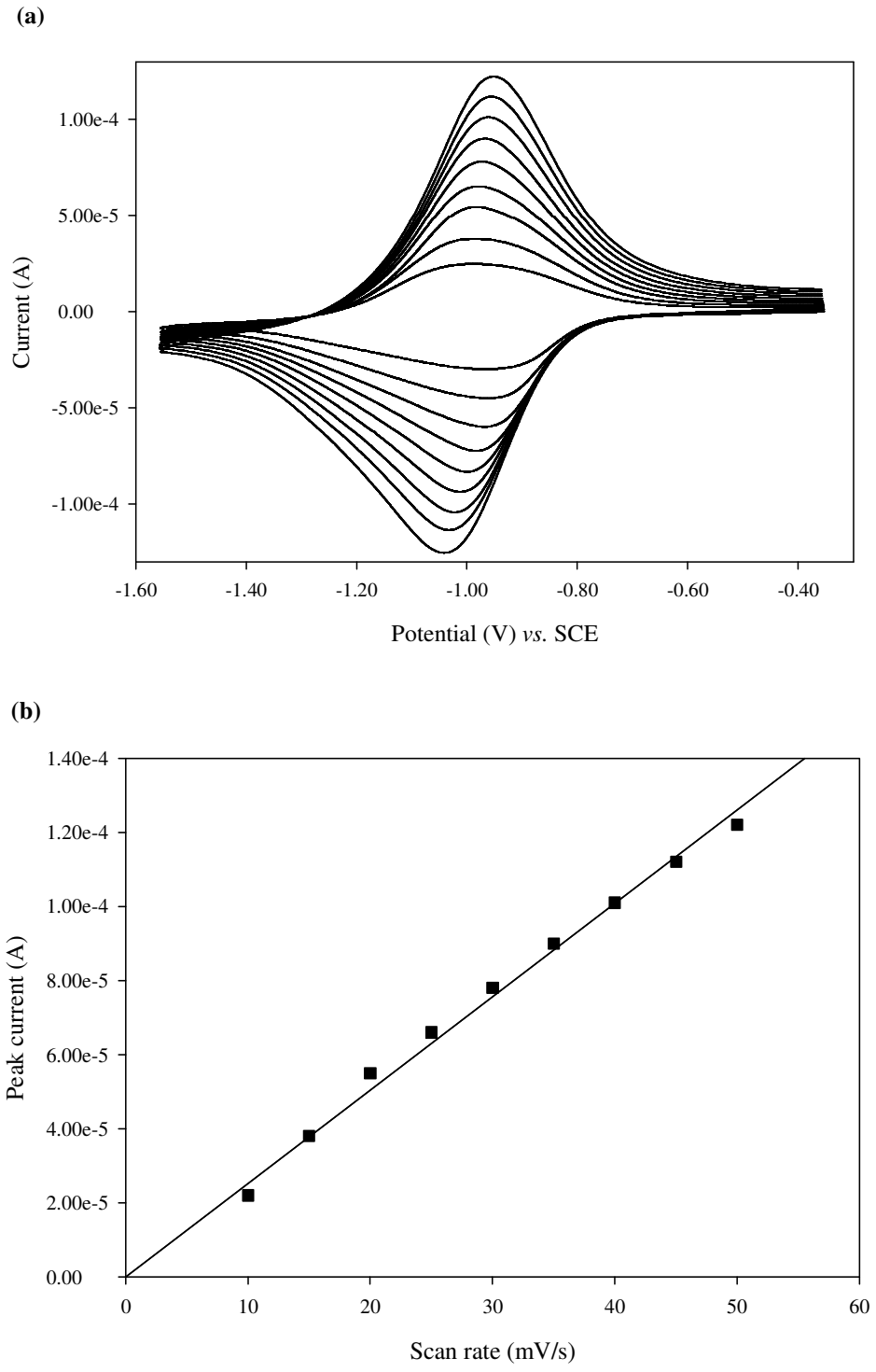

Figure 4.9. (a) Cyclic voltammogram of $\{Fe_4S_4\}^{2+/1+}$ couple confined in poly (**21,** cysteinyl form) film on Pt disc electrode at scan rates varied from 10 to 50 $mV.s^{-1}$ (0.2 M $[NBu_4][BF_4]$ in acetonitrile); (b) Relationship between peak current and potential of different scan rates.

It can be seen from **Figure 4.10**, that neither repetitive CV scanning nor prolonged exposure to electrolyte extensively diminishes the $\{Fe_4S_4\}^{2+}/\{Fe_4S_4\}^{+}$ redox response, which is consistent with cysteinyl ligation to the cluster centres, rather than ionic binding; in the latter case, repetitive cycling and long exposure to solvent would be expected to leach the cluster from the polymer, thereby diminishing the current response.

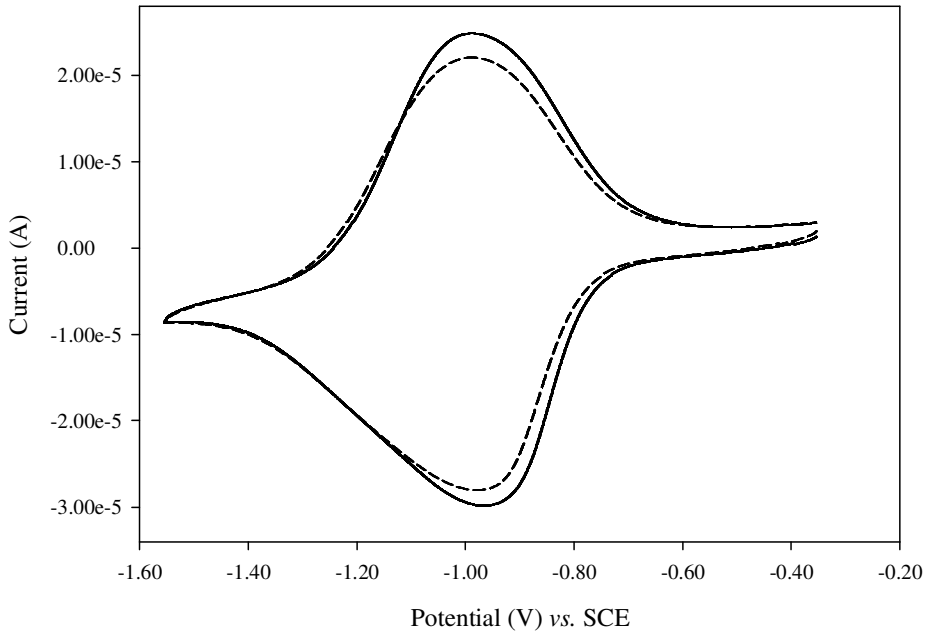

Figure 4.10. Cyclic voltammogram of $\{Fe_4S_4\}^{2+/1+}$ couple confined in poly (**21,** cysteinyl form) film on Pt disc electrode at fifth (solid line) and 55th (dashed line) scans (0.2 M $[NBu_4][BF_4]$ in acetonitrile, 5 mV.s^{-1}).

4.9.1.3 Modification with the sub-site complex

Once we have the $\{Fe_4S_4\}^{2+/1+}$ couple confined in this inorganic polyferredoxin, the next stage was the incorporation of the diiron sub-site, $Fe_2(CO)_6(CH_3C(CH_2S)_2CH_2SCOCH_3)$ **(8)** into the film. The synthesis and characterisation of this complex has been described elsewhere (see **Chapter 3**). The

electrochemical behaviour of complex **8** itself in 0.2 M $[NBu_4][BF_4]$-acetonitrile was recorded as depicted in **Figure 4.11**. This complex shows a partially reversible one-electron reduction occurring at E_p = -1.18 V *vs.* SCE. Notably, most of the {2Fe-3S} complexes essentially share this common electrochemical response feature. [27] The detection of a small reduction wave at lower potential is due to absorption at the surface electrode which no longer is seen at the second scan or at the higher scan rate.

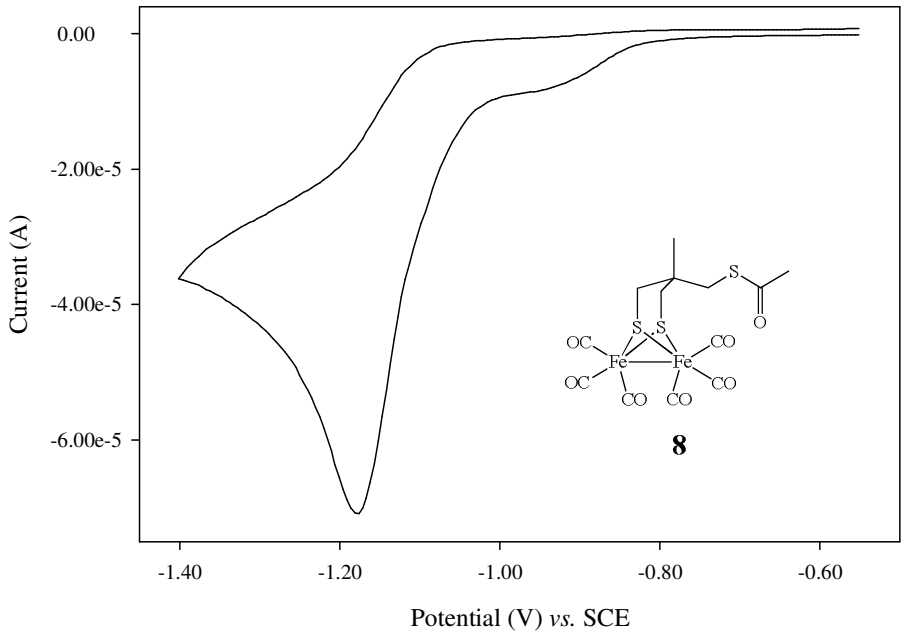

Figure 4.11. Cyclic voltammogram of $Fe_2(CO)_6(CH_3C(CH_2S)_2CH_2SCOCH_3)$ **(8)**(2 mM, 0.2 M $[NBu_4][BF_4]$ in acetonitrile, 50 $mV.s^{-1}$).

As previously reported by the UEA group, synthetic $\{Fe_4S_4\}$ clusters can be modified in solution by attaching diiron units using the thioacetyl activated complex **8**. [109] With clusters of the type $[Fe_4S_4(SR)_4]^{2-}$ (R = Et or Ph), multiple substitution of the thiolate ligands by the sub-site analogue can occur, giving a distribution of species $[Fe_4S_4(SR)_4]_{4-x}(sub\text{-}site)_x]^{2-}$ (x = 0 to 4, sub-site = $Fe_2(CO)_5(CH_3C(CH_2S)_2CH_2S\sim$).

Importantly, CO elimination leads to bridging thiolate formation with each progressive substitution shifting the reduction potential of the $\{Fe_4S_4\}$ cluster about 120 mV more positive, due to the electron withdrawing influence of each of the diiron pentacarbonyl units is additively engaged. To study the reaction of $Fe_2(CO)_6(CH_3C(CH_2S)_2CH_2SCOCH_3)$ (**8**) with the cluster-bound polymer, the modified electrode is immersed into the complex **8** solution in a glove box (3 mM, 0.2 M $[NBu_4][BF_4]$, CH_3CN).

Cyclic voltammetry is used to monitor the electrochemical changes which could provide an insight into the interplay between the $\{Fe_4S_4\}$ cubane cluster and the {2Fe-3S} sub-site. **Scheme 4.5** illustrates the schematic reaction and displays the recorded electrochemical behaviour for each process. Cyclic voltammogram **A** indicates the response of the electrode before contact with complex **8**, which corresponds to the redox response of scan 55^{th} as shown in **Fig. 4.10** previously. After 18 hours, the response of the unmodified cluster is replaced by a new couple **I** with a reduction potential E^o shifted 110 mV positive of that for the parent cluster (refers to voltammogram **D**). In parallel with the earlier reported solution data, this shift is indicative of mono substitution of the cluster by a sub-site unit as depicted in voltammogram **D** in the scheme. This interpretation is strongly supported by FTIR spectroscopy of the film (**Figure 4.12**), which reveals new CO bands at 2035(m), 1971(s) and 1911(w) cm^{-1} with a pattern and frequency close to those observed in solution for an isolated synthetic H-cluster, where $\upsilon(CO)/cm^{-1}$ are 2035(m), 1970(s) and 1912(w). The FTIR recorded on complex **8** independently (**Figure 4.13**) also suggested a rearrangement of sub-site has occurred when it bound in polymer matrix.

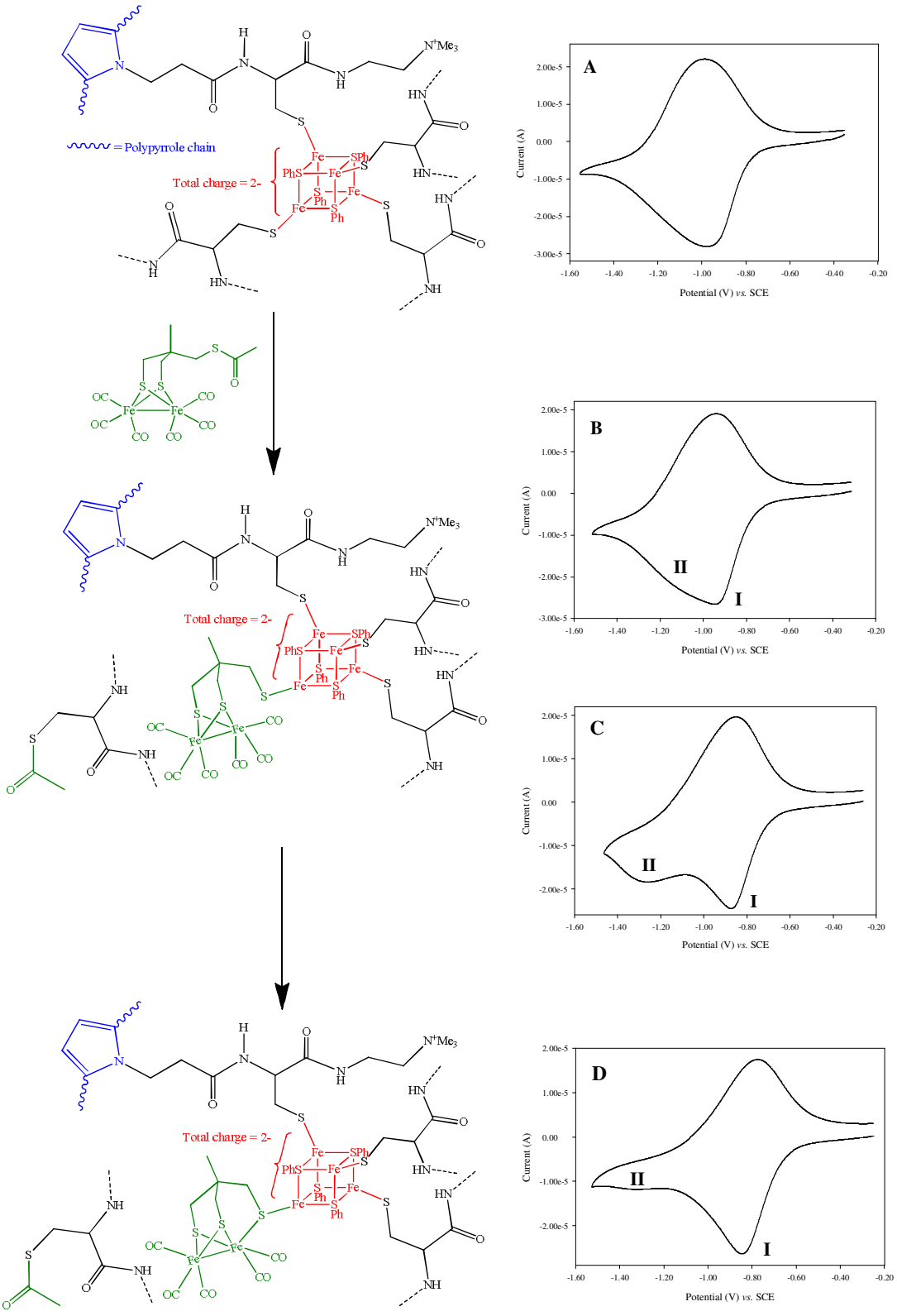

Scheme 4.5. Schematic representation for the reaction and electrochemical behaviour for each process.

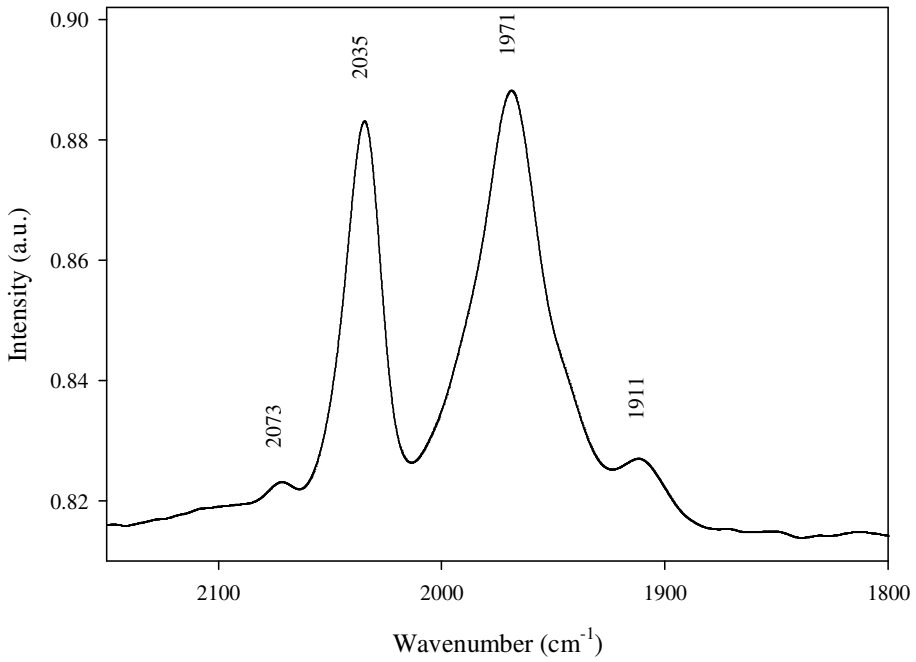

Figure 4.12. FTIR spectra of modified electrode after exposing to the diiron thioacetyl sub-site (**8**) for 18 hours.

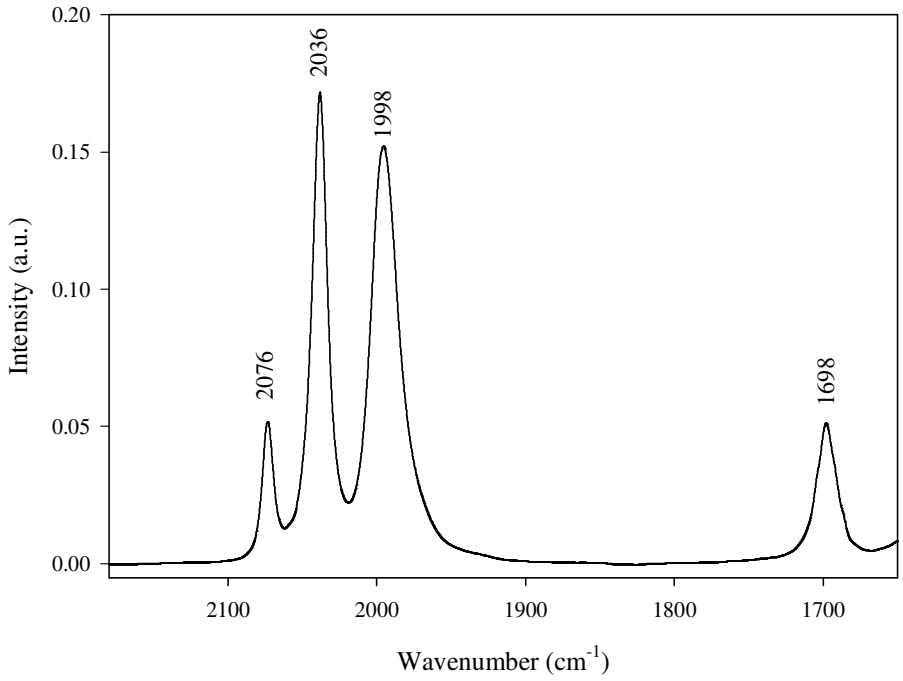

Figure 4.13. FTIR spectra of $Fe_2(CO)_6(CH_3C(CH_2S)_2CH_2SCOCH_3)$ (**8**) in acetonitrile.

If we take a closer look on the development of the electrochemical response at the shorter times of 90 minutes (**B**) and four hours (**C**) at the same scheme (**Scheme 4.5**), it is clear that a redox active intermediate **II** emerges and subsequently decays. **II** has a reduction potential substantially negative of the parent cluster, $\{Fe_4S_4\}^{2+}/\{Fe_4S_4\}^{+}$. FTIR examination of the film after four hours has displayed a well separated band at 2073 cm^{-1} (not shown here) and overlapping bands consistent with the formation of the hexacarbonyl derivative (**Figure 4.13**). The reduction potential is shifted negative is fully consistent with the substitution of a cysteinyl thiol by a more donating "alkyl" thiol *viz.* the cluster does not experience the electron withdrawing influence of the carbonyl unit until the Fe-S-Fe bridge is formed by CO loss.

Further electron transfer from the reduced cluster to the bound sub-site has been observed for an analogous assembly in solution, and this has been suggested to be coupled to the dissociation of the $S^{thioether}$-$Fe^{sub\text{-}site}$bridge as previously reported. [109] For the assembly within the polymer, this further electron transfer is absent, possibly because dissociation is less favoured or BF_4^- counter ion diffusion from the film to maintain charge neutrality is restricted. [163]

The charge associated with the reversible one electron reduction was measured by integration of the current-time for the cyclic voltammetric responses before and after the modification. Overall, sub-site attachment occurs without significant loss of the cluster core from the film as is evident from the charge integration before and after conversion, which we find to be 85 and 70 μC respectively, corresponding to a conversion of more than 80%.

From the point of view of the H-cluster framework, the mono substituted complex $[Fe_4S_4(SCH_2\text{-electropolymer})_4\{Fe_2(CO)_5(CH_3C(CH_2S)_3\}]^{2-}$ is very interesting as the environment around the $\{Fe_4S_4\}$ core is rather similar to the H-cluster in the enzyme with its three cysteines from the protein backbone and the {2Fe-2S} sub-site on the fourth iron. Synthesising the synthetic H-cluster on the surface of an electrode within the polymer framework appears to restrict the problem of di-, tri- and tetra substitution by diiron sub-site as occurs in solution. We are not clear why this should be the case but suggest that the steric crowding in the polymer restricts multiple substitutions by the bulky activated sub-site.

4.10 Comparison studies between solid state and solution electrochemistry of H-cluster

This section explores the electrochemical behaviour of H-cluster in solution. It is an electrochemistry comparison study of H-cluster constructed in solid state and in solution. $\{Fe_4S_4\}$ clusters with mercaptan ligands on irons of the cubane are easily synthesisable, and introduction of new ligands is just done by exchanging present ligands with other organic thiols. [73, 171]

Because of the high coordinating power of mercaptans with $\{Fe_4S_4\}$ clusters, with the presence of diiron sub-site directly, we expect possibility of multiple substitutions and polymerisation. Based on previous literature, $[Fe_4S_4(SPh)_4]^{n-}$ (n = 1 to 4) can exist in mono-, di-, tri- and tetra-anion forms under different potential. [172] The primary redox chemistry of $[Fe_4S_4(SPh)_4]^{2-}$ under inert atmosphere (N_2 or Ar) is reasonably well established; under suitable conditions a four-membered electron transfer series can be observed by cyclic voltammetry of which the parent di-anion [171] and the tri-anion [173] are stable and isolable members, as depicted in **Scheme 4.6**.

$$[Fe_4S_4(SPh)_4]^{4-} \underset{+e}{\overset{-2.26\ V,\ -e}{\rightleftharpoons}} [Fe_4S_4(SPh)_4]^{3-} \underset{+e}{\overset{-1.49\ V,\ -e}{\rightleftharpoons}} [Fe_4S_4(SPh)_4]^{2-} \underset{+e}{\overset{-0.29\ V,\ -e}{\rightleftharpoons}} [Fe_4S_4(SPh)_4]^{-}$$

Scheme 4.6. Reduction potential of $[Fe_4S_4(SPh)_4]$ anion species in 0.2 M $[NBu_4][BF_4]$-THF, potentials are relative to ferrocenium-ferrocene (adapted from reference [172]).

Figure 4.14 describes the electrochemistry of $[Fe_4S_4(SPh)_4][NBu_4]_2$ (**1**) in 0.2 M $[NBu_4][BF_4]$-acetonitrile, which shows two successive one-electron processes. The first reversible reduction at $E_{1/2}$ = -0.97 V (acetonitrile, *vs*. SCE) corresponds to the $\{Fe_4S_4\}^{2+}/\{Fe_4S_4\}^{+}$ couple, and the second partially reversible reduction at E_p = -1.72 V corresponds to $\{Fe_4S_4\}^{+}/\{Fe_4S_4\}^{0}$ couple. As is well established, the cubane electrochemistry is sensitive to the nature of the thiolate substituent. [174]

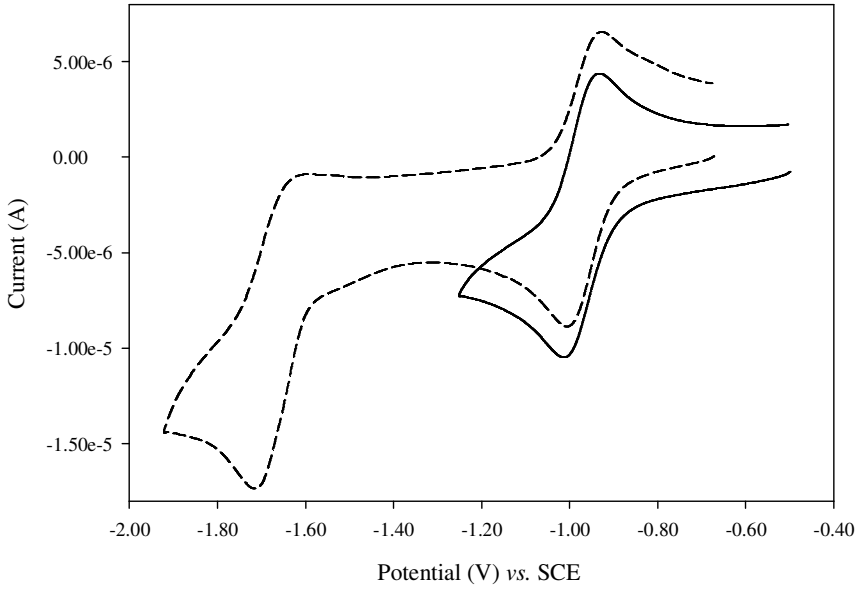

Figure 4.14. Cyclic voltammogram of $[Fe_4S_4(SPh)_4][NBu_4]_2$ (**1**) (0.2 M $[NBu_4][BF_4]$ in acetonitrile, 5 $mV.s^{-1}$), both scans recorded separately.

For the case when $[Fe_4S_4(SPh)_4][NBu_4]_2$ (**1**) is incorporated in the poly (**21**, cysteinyl form), the electrochemical response due to $\{Fe_4S_4\}^+/\{Fe_4S_4\}^0$ couple is very weak (**Figure 4.15-I**). This has been discussed elsewhere and is attributable to much slower electron self exchange between $\{Fe_4S_4\}^+/\{Fe_4S_4\}^0$ centre. [172]

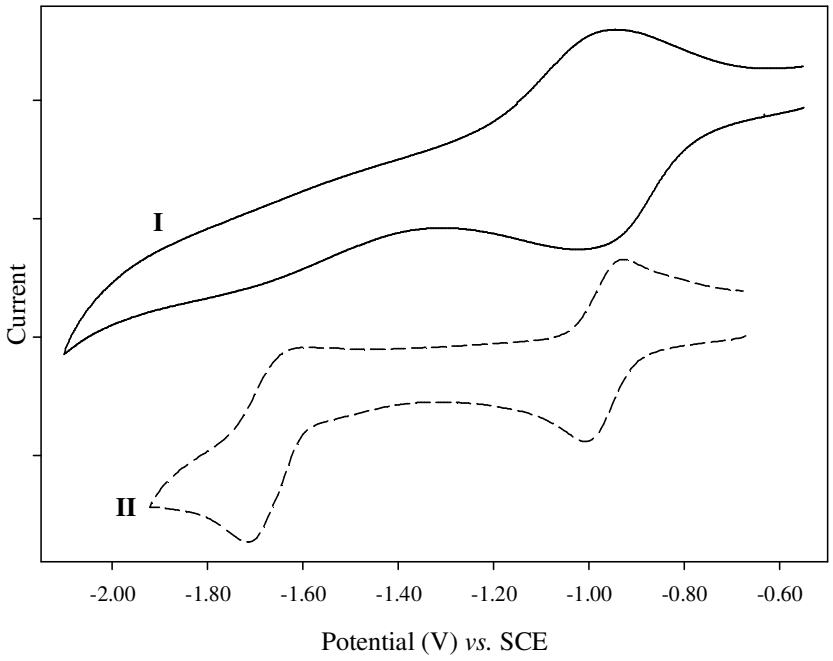

Figure 4.15. Comparison of cyclic voltammogram of cluster behaviour (**1**) recorded in solid state (**I**) and solution electrochemistry (**II**).

Subsequently, in the cell with $[Fe_4S_4(SPh)_4]^{2-}$ solution, one equivalent of complex **8** was added and CV was recorded (**Figure 4.16**). At the beginning, it gives a similar response with what we observed in the solid state earlier (refer to **Scheme 4.5**), a primary reversible one-electron reduction couple at -1.00 V (*versus* SCE) corresponding to $\{Fe_4S_4\}^{2+/+}$ core, and a multi-electron reduction at -1.15 V which encompasses the irreversible reduction of the sub-site (dashed line). Nevertheless, after three hours, the voltammogram becomes complicated, as in the solution, although just

one equivalent of diiron sub-site presents, it is not obligatory mono substitution will occur, it might goes to di- or tri-substitution, which most probably is the case here (dotted line). Notably, the solution process is very broad, the I_p^{ox} and I_p^{red} are smaller than observed after the immediate reaction. In the polymer framework, it appears that we obtained well define electrochemistry because substitution of the backbone cysteinyl ligands are restricted to a single sub-site unit.

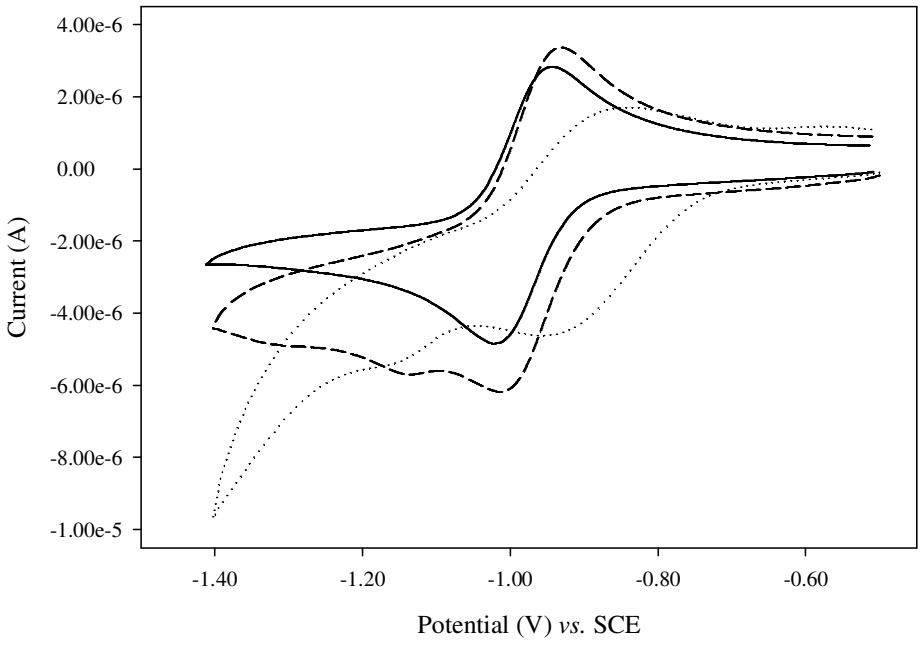

Figure 4.16. Cyclic voltammogram of $[Fe_4S_4(SPh)_4][NBu_4]_2$ (**1**) reacts with one equivalent of $Fe_2(CO)_6(CH_3C(CH_2S)_2CH_2SCOCH_3)$ (**8**) at different duration (0.2 M-$[NBu_4][BF_4]$ in acetonitrile, 5 $mV.s^{-1}$), (---) 5 min; (···) 3 hours.

The clear limitation of the present H-cluster model is the absence of the cyanide ligand. Unfortunately, generation of the cyanide derivative in solid state using the same approach on what we done for complex **8** has not been successful, despite numerous attempts. A clear restriction is that bringing in a di-anionic centre to the polymer

requires charge compensation by cationic group has been problematic, and new strategies have to be designed.

Given the difficulty of introducing the dicyanide sub-site onto the cluster within the polymer framework, we have explored the solution electrochemistry of $[Fe_4S_4(SPh)_4][NBu_4]_2$ (**1**) with the dicyanide sub-site, $[Fe_2(CO)_4(CN)_2(CH_3C(CH_2S)_2CH_2SCOCH_3)][(Et_4N)_2]$ (**11**).

Cyclic voltammetry in **Figure 4.17** shows the effect of adding one equivalent of complex **11** to $[Fe_4S_4(SPh)_4][NBu_4]_2$ (**1**), the reduction process corresponding to the $\{Fe_4S_4\}^{2+}/\{Fe_4S_4\}^{+}$ couple is shifted slightly more negative. This might be attributable to replacing an -SPh ligand by an essentially alkyl thiolate ligand. However, we would expect a substantially more negative shift of about 200 mV rather than the observed shift of 20 mV. It is possible that open (hexacarbonyl) and close (pentacarbonyl) diiron sub-site are bound as a single cluster with compensating effect producing only a small shift. Nevertheless, we have yet to explore further detail on this matter.

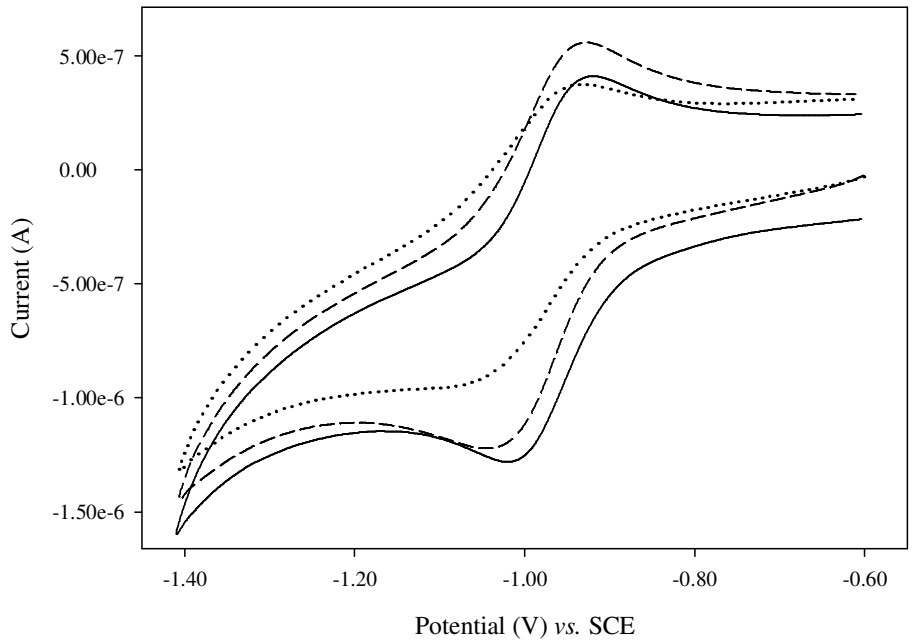

Figure 4.17. Cyclic voltammogram of $[Fe_4S_4(SPh)_4][NBu_4]_2$ (**1**) reacts with one equivalent of $[Fe_2(CO)_4(CN)_2(CH_3C(CH_2S)_2CH_2SCOCH_3]^{2-}$ (**11**) at different duration (0.2 M-$[NBu_4][BF_4]$ in acetonitrile, 5 $mV.s^{-1}$), (---) 1 hour; (···) 24 hours.

4.11 General conclusion

An approach for incorporating H-cluster into surface bound electropolymers has been successfully established. However, work on cyanation of the model H-cluster which would provide a closer analogue of the natural site, and allow further studies of the electronic interactions between sub-site and cluster, and the potential for electrocatalysis is still undergoing (**Scheme 4.7**).

The assembly of new solid state materials for electrocatalysis of this cyanide derivative H-cluster is likely to require the synthesis of new ligands/polymers possessing both functionality for covalent binding of sub-sites, electron transfer relays, proton transfer relays and possibly hemi-labile ligands.

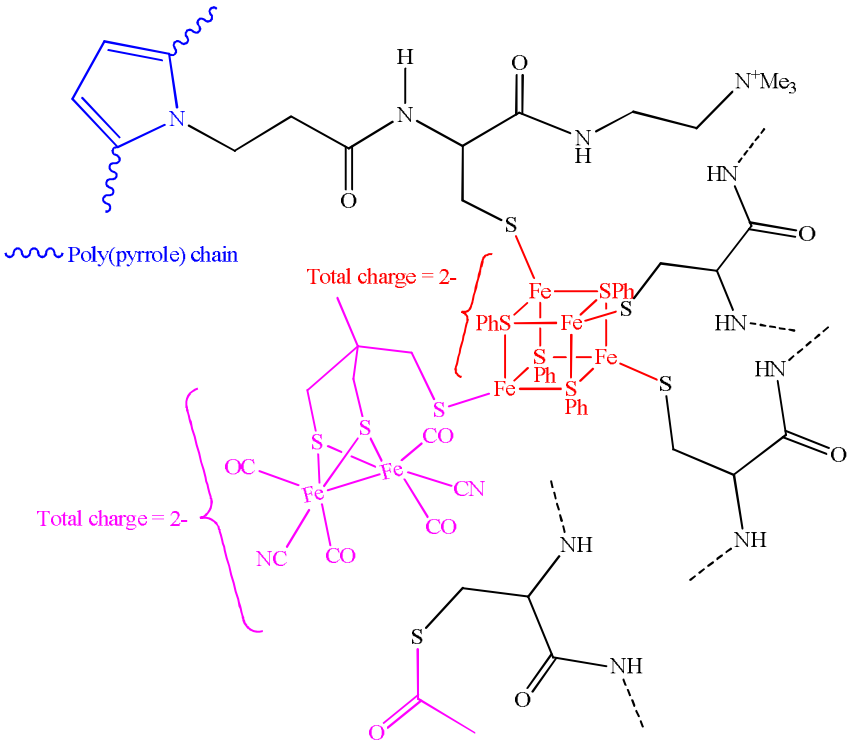

Scheme 4.7. Schematic diagram of cyanation model complex for H-cluster embedded within polymer framework.

4.12 Experimental

Electropolymerisation of monomers **16** and **21**, respectively are recorded using a Hi-Tek Instruments (England) potentiostat type DT2101.The electropolymerisation was done in a three-compartment glass cell, platinum (Pt) disc was used as the working electrode (electrode area = 0.28 cm^2), Pt gauze as the secondary electrode and saturated calomel (SCE), Hg/Hg_2Cl_2-3 M LiCl was used as the reference electrode. All electrodes were cleaned before use and the working electrode was polished with 1 µm diamond paste on a polishing cloth. The cell was charged with 5-10 mM of monomer in 0.2 M $[NBu_4][BF_4]$-acetonitrile.

Cyclic voltammetry and other measurements were made using an Autolab PGSTAT 30 with GPES version 4.9 software. Refectance FTIR was recorded on a Bruker Vertex 80 spectrometer.

Chapter 5

Voltammetric Studies of *Pyrococcus furiosus* {4Fe-4S} ferredoxin: Towards new assembly related to H-cluster

This chapter explores the possibility of building a new assembly related to H-cluster by combining a mutant ferredoxin with synthetic diiron sub-site of [FeFe]-hydrogenase. To our knowledge, this is the first attempt on such experiment which involves the natural and synthetic systems in the same reaction. Protein film voltammetry and bulk voltammetry methods have been employed to follow the reactions between these two different systems.

5.1 Introduction

As described earlier in **Chapter 2**, iron-sulphur proteins which possess inorganic sulphur are commonly designated as ferredoxins which can be classified into three categories based on its nature. The idea of this word come from Mortenson *et al*. who defined ferredoxin to a non-*heme*, iron-containing protein with a low redox potential isolated from the anaerobic bacterium, *Clostridium pasteurianum.*[175]Ferredoxins are found in living systems such as green plants (including algae), photosynthetic bacteria, protozoa and some fermentative anaerobic bacteria. They play key roles as electron

carriers in processes such as nitrogen fixation, dihydrogen evolution-consumption and photosynthesis. [176, 177]

5.1.1 *Pyrococcus furiosus* ferredoxin (*Pf* Fd)

Pyrococcus furiosus ferredoxin (*Pf*Fd) is one of the most thermostable ferredoxins. This hyperthermophile *Pf*Fd D14C which grows optimally at temperatures above 80 ºC, contains a single cluster which can undergo reversible cluster conversion between the {4Fe-4S} and {3Fe-4S} forms under anaerobic condition. [178-180] Previous studies have shown that there is a well-established tendency to coordinate a fourth metal, resulting in the formation of {M3Fe-4S} cubanes (M = fourth metal atom) such as the familiar {4Fe-4S} cluster (**Scheme 5.1**). [181-187]

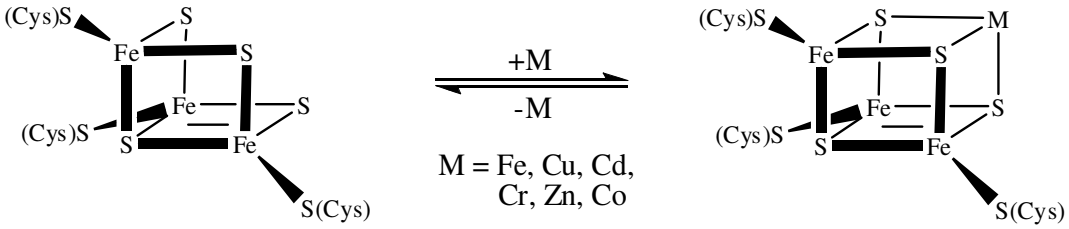

Scheme 5.1. Interconversion between cuboidal {3Fe-4S} and cubane {M3Fe-4S} clusters.

In most cases, the {4Fe-4S} cluster undergoes an one-electron redox couple ({4Fe-4S}$^{2+/1+}$) at low potential, typically near -400 mV, although high potential clusters are present in some small redox proteins known as high-potential iron proteins (HiPiP) where the reduction potential are much higher, near to -750 mV *versus* SHE (see **Chapter 2**). In the {4Fe-4S}$^{2+/1+}$ form of the ferredoxin, the *Pf* Fd cubane is coordinated by three cysteinate (Cys) and one aspartate (Asp) residue, rather than by

the typical four Cys residues. There isspectroscopic evidence that the labile Fe is coordinated by the aspartate in both oxidised and reduced forms. [188] As far as can be deduced, aspartate ligation has several consequences: (i) it labilises the cluster towards release of the O-bound Fe and binding of exogenous ligands, [189-191] (ii) reduced {4Fe-4S}$^{+}$ clusters exist completely (*Desulfovibrio africanus* Fd III) or partly (*Pf* Fd) in the unusual S = 3/2 spin state as determined by low-temperature electron paramagnetic resonance (EPR), [179, 192] which is in contrast to the pure S = 1/2 ground state for reduced four-Fe clusters in most of the proteins with complete Cys ligation [179] and (iii) the O-ligation (RCO_2^-) does not markedly alter the reduction potential relative to the conventional all-cysteinate (RS^-) ligated clusters. [193, 194]

Like most of the ferredoxin, *Pf* Fd has a key role in mainstream electron transfer. It acts as the electron acceptor for two glycolytic redox enzymes, glyceraldehyde-3-phosphate oxidoreductase and pyruvate oxidoreductase as well as the electron donor for a membrane-bound multi sub-unit hydrogenase complex. [195] Apart from that, *Pf* Fd is also presumed as redox partner of several other oxidoreductases, which involved in aldehyde activation and oxoacid. [196] Hence, there are a variety of enzymes available which utilise *Pf* Fd as their physiological electron carrier.

In this study, we have used a mutant form of an enzyme in which the cluster coordinated Asp has been replaced by Cys (D14C). This material was supplied by Francis E. Jenny. This mutant was chosen because it provides a very stable "conventional" ferredoxin platform for exploring its chemistry. It will be referred to subsequently as *Pf* Fd D14C.

5.1.2 History of the protein film voltammetry method

Given all the attention to the surface redox reactions, the application of voltammetry for probing the chemistry of redox proteins has recently emerged as an easy and powerful method of investigating biologically relevant redox-active compounds. [197-201] By simple adsorption of the redox protein sample onto the surface of some suitable lipophilic electrode, insights into the processes of electron transfer and protein-protein interactions can be obtained from experiments performed in common voltammetric setup. Methods of studying about the internal and external electron transfer of protein molecules are few, because electrochemical active groups are often wrapped by polypeptide chain and far from electrode surface, which resulted in the difficulties in electron transfer. In addition, there are still some obstacles introduced by the existence and location of electron transfer channel and the distribution uniformity of surface charges.

Therefore, it is very critical in the electrochemical research on protein adsorbed onto electrode surface to have a good orientation and retain its native structure and properties in an appropriate way. In such a kind of research, protein film voltammetry (PFV), which was founded by Armstrong and his co-workers in University of Oxford in the late 1990s, is perhaps the answer for it. [182, 185, 202-207]

The overall concept and various aspects of PFV are represented in **Figure 5.1**. For chemists, the beauty of being able to control the catalytic action of enzymes, literally at the touch of a switch, is inspiring ingenious ways of attaching enzymes to electrodes and studying the structures and dynamics of the resulting interface, as well as the efforts to explain and simulate the different forms of electrocatalytic response. [203]

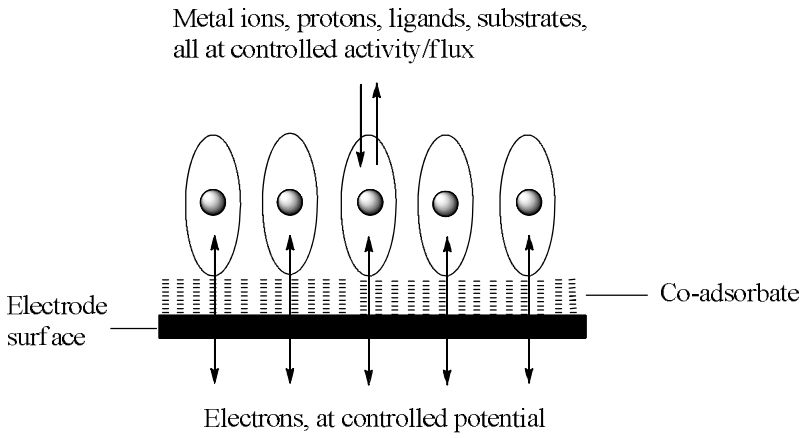

Figure 5.1. An idealised configuration for protein film voltammetry. The protein molecules are arranged as a perfect monolayer, each behaving independently. They interact non-covalently with functionalities on the electrode surface to produce orientations allowing facile interfacial electron exchange and interaction with agents in the contacting electrolyte (adapted from reference [203]).

Ideally, in PFV, protein molecules are induced to absorb on an innocuous electrode surface that acts as an electron donor or acceptor, which makes electron transfer into/out of/within protein. These protein molecules come under the control of the applied electrode potential, and redox-active sites became visible through their voltammetric signals. A great deal of information could be found, such as the mechanism and rate of internal electron transfer, interfacial electrochemistry between protein and electrode, coupled proton transfer, electron transfer between the enzyme and the substrate, active site and ion channel of protein and so on. [208, 209] In the simplest case, the redox active sites of protein molecules are a pair of oxidation and reduction peaks centred at the formal reduction potential. Rapid redox-coupled reactions can be detected with ease and quantified. It can also be ascertained whether, by comparison with studies carried out in solution, the film (electrode-bound) environment offers protection (resistance) to these reactions.

In this study, graphite edge is chosen as the electrode. Compared with the basal plane of metal and carbon nano tube electrodes, [205, 210] the edge plane of pyrolytic graphite offers a better conductivity, higher hydrophilicity and more oxides content. Thus, the electron transfer ability of protein molecule is stronger and electrode kinetics procedure is faster. This pyrolytic graphite edge electrode can be easily fabricated by cutting a piece of highly ordered pyrolytic graphite suitably in sequence to make the graphite layers perpendicular to the electrode surface. [203]

5.2 Results and Discussion

5.2.1 Electrochemcial behaviour of mutant *Pyrococcus furiosus* ferredoxin, *Pf*Fd D14C

The voltammetric signals obtained from PFV method can be used as electrochemical markers for identifying and quantifying the status of centres present within the protein. All voltammograms were recorded at temperature thermostated at 4 ºC in order to optimise the stability of the protein itself. **Figure 5.2** displays the response of *Pf* Fd D14C in PFV. Although the recorded signal of *Pf* Fd D14C is not very distinctive, it is considered a good response in protein film voltammetry. We can see there is a pair of redox signals at reduction potential, E_p = -678 ± 5 mV *vs.* SCE.

It is also possible to observe directly the electrochemical behaviour of *Pf* Fd D14C itself in solution.

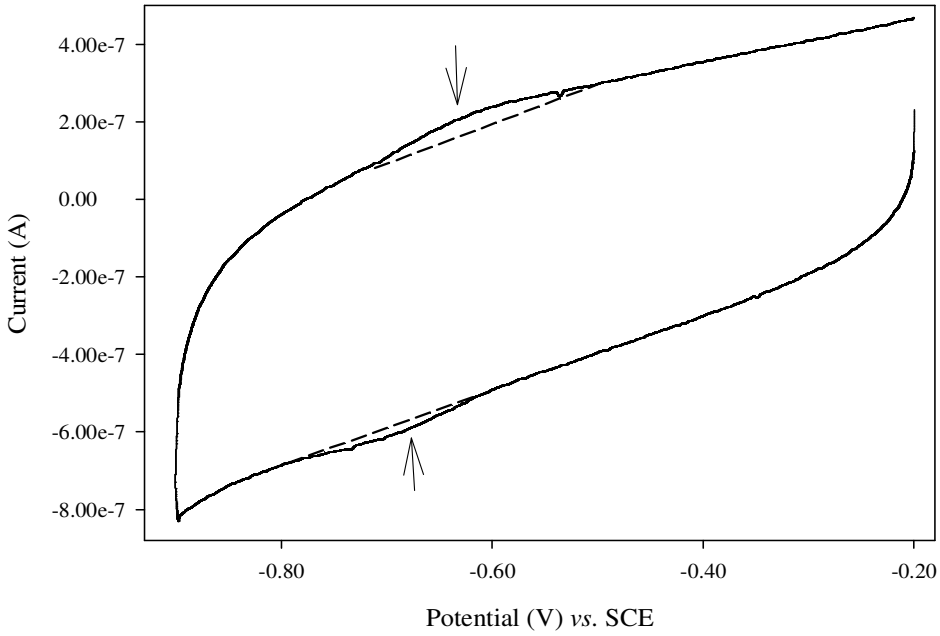

Figure 5.2. Film voltammogram of {4Fe-4S} ferredoxin extracts from *Pyrococcus furiosus* (100 μM), pH 7.0 in 20 mM mixed buffer-0.1 M NaCl with 200 μM of polymyxin as co-adsorbate. Temperature 4 ºC, scan rate 5 mV.s^{-1}.

Well defined, reversible and reproducible bulk voltammogram of *Pf* Fd D14C at temperature 4 ºC is shown in **Figure 5.3**. Under this slow scan rate of v = 5 mV.s^{-1}, the reduction potential for the {4Fe-4S} cluster of *Pf* Fd D14C was found to be -680 ± 5 mV *vs.* SCE, whereas the peak separation, ΔE_p was *ca*. 60 mV which is in accordance to the expected value for a diffusion controlled response. Currents of the anodic and cathodic peaks were similar to each other. These two observations indicate a fully reversible electron exchange system. The redox couple which corresponding to the signal is $\{Fe_4S_4\}^{2+}/\{Fe_4S_4\}^{+}$.

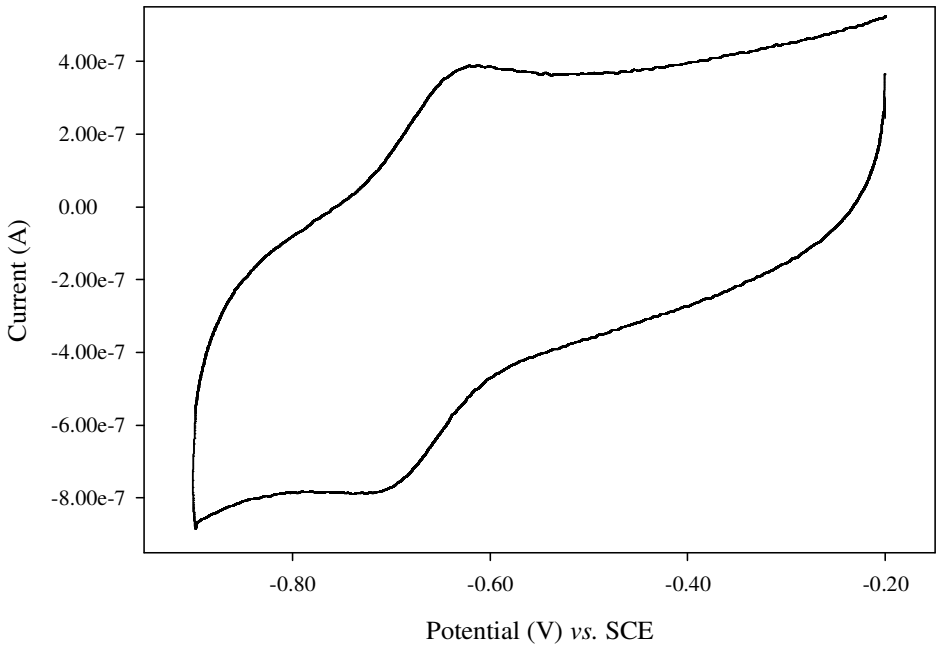

Figure 5.3. Bulk solution voltammogram of {4Fe-4S} ferredoxin extracts from *Pyrococcus furiosus* (100 μM), pH 7.0 in 20 mM mixed buffer-0.1 M NaCl with 200 μM of polymyxin as co-adsorbate. Temperature 4 ºC, scan rate 5 $mV.s^{-1}$.

5.2.2 Reaction of *Pyrococcus furiosus* ferredoxin mutant with synthetic ionic sub-site $[Fe_2(CO)_5CH_3C(CH_2S)_2CH_2S][Na]$ (9)

To build an artificial assembly structure related to the active site of [FeFe]-hydrogenase, the H-cluster, {4Fe-4S} of *Pf* Fd D14C have to be modified/reacted with a synthetic {2Fe-3S} diiron sub-site. Here we have synthesised a new ionic iron sub-site $[Fe_2(CO)_5CH_3C(CH_2S)_2CH_2S][Na]$(**9**) from the targeted hexacarbonyl iron complex, $[Fe_2(CO)_6(CH_3C(CH_2S)_2CH_2SCOCH_3)]$ (**8**) by reacting it with sodium thiomethoxide. The detail of this synthesis is described in **Chapter 3**. In this aqueous electrochemistry system, all the substrates must be able to dissolve in the mixed buffer electrolyte, this is where the speciality of complex **9** plays the role as with its ionic properties, it can easily dissolved in the electrolyte.

In order to have clear signals of the reaction between *Pf* Fd D14C and complex **9**, the bulk cyclic voltammetry was performed (**Figure 5.4**). Despite the presence of carbonyl groups on the iron complex, no shift in potential is observed, only lowering the signal intensity, indicative of damage or extrusion of the protein. From this, we concluded that the ionic iron sub-site is not reactive to bind with the ferredoxin or that sterically cannot access the protein cluster.

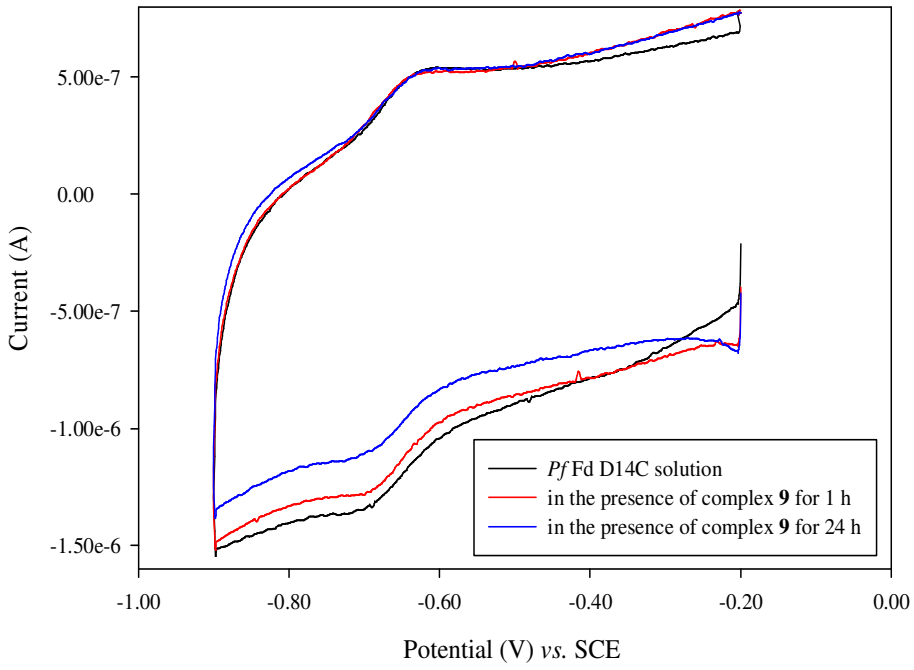

Figure 5.4. Bulk solution voltammetry of {4Fe-4S} ferredoxin extracts from *Pyrococcus furiosus* (100 μM) reacts with $[Fe_2(CO)_5(CH_3C(CH_2S)_2CH_2SNa]$ (**9**), pH 7.0, 20 mM mixed buffer-0.1 M NaCl with 200 μM of polymyxin as co-adsorbate. Temperature 4 ºC, scan rate 5 $mV.s^{-1}$.

5.2.3 Reaction of *Pyrococcus furiosus* ferredoxin mutant with thiophenol

In order to test whether the protein bound cluster were accessible to simple substitution, the effect of thiophenol (PhSH or C_6H_5SH) on the ferredoxin electrochemistry is examined.

Thiophenol is known to remove iron-sulphur cluster from *Pf* Fd D14C protein by extruding the cluster as the tetraphenyl thiolate di-anion. **Figure 5.5** shows the effect of addition of thiophenol. It also might be expected to perturb the cluster potential on partial replacement of cysteine ligand. In practice, the addition of thiophenol is found to have little effect on the cluster voltammetric response as evidence from the **Fig. 5.5**. This suggests that the cluster is not very accessible. Therefore the unfolding of the protein is investigated.

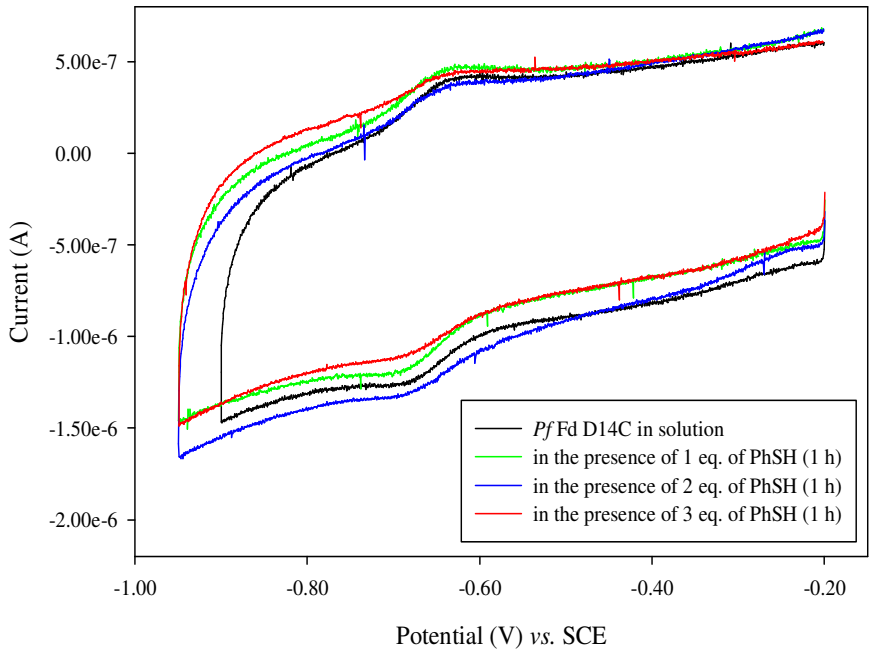

Figure 5.5. Bulk solution voltammetry of {4Fe-4S} ferredoxin extracts from *Pyrococcus furiosus* (100 µM) reacts with PhSH, pH 7.0 in 20 mM mixed buffer-0.1 M NaCl with 200 μM of polymyxin as co-adsorbate. Temperature 4 ºC, scan rate 5 $mV.s^{-1}$.

5.2.4 The effect of the unfolding reagent on the electrochemistry of *Pyrococcus furiosus* ferredoxin mutant

As acknowledged, a protein must gain a stable and precisely ordered conformation to perform its biological function properly. Protein molecules normally comprised both hydrophobic and hydrophilic amino acid residues. When the protein folded into tertiary structure form, some of the hydrophobic residues get buried in the interior, while others are exposed to the surface or located in crevices. These hydrophobic interactions responsible in the dictating conformation, solubility, ligand binding and aggregating properties in proteins. During unfolding, the hydrophobicity is destroyed and through refolding, it can be regenerated. The unfolding of a protein can be probed by magnetic circular dichroism, MCD. Based on literature, guanidine hydrochloride, GdnHCl ($NH_2C(=NH)NH_2$•HCl) was chosen as the unfolding agent in this study. This organic compound is one of the most effective denaturants in many protein studies which play a major role in unfolding proteins and altering their three-dimensional structure. Consequently, some proteins will be irreversibly altered upon interaction with guanidine solutions and may lose their binding function. Almost all proteins with an ordered structure lose their structure and become randomly coiled in the presence of six molar (6 M) GdnHCl. [211-215]

In order to have the unfolding effect on *Pf* Fd, 6 M of GdnHCl was added into 100 μM of *Pf* Fd D14C and CV was recorded in buffer solution (**Figure 5.6**). It can be seen that a clear shifting of the protein signals toward positive potential were observed in the presence of the unfolding agent. This indicates changes have happen to the protein structure. However, little is known about their structures and intermediate states that are generated during a protein unfolding process.

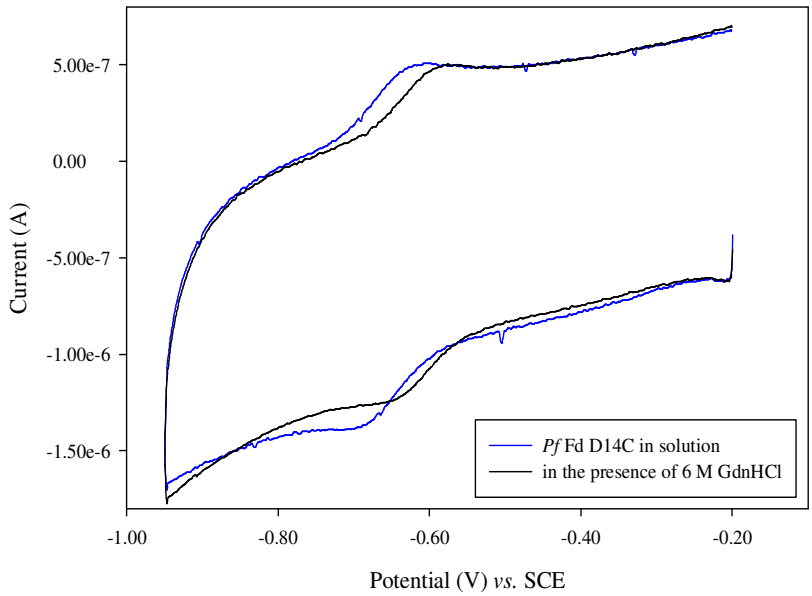

Figure 5.6. Bulk solution voltammetry of {4Fe-4S} ferredoxin extracts from *Pyrococcus furiosus* (100 μM) in presence with 6 M GdnHCl, pH 7.0, 20 mM mixed buffer-0.1 M NaCl with 200 μM of polymyxin as co-adsorbate. Temperature 4 ºC, scan rate 5 mV.s^{-1}.

5.2.5 Magnetic circular dichroism studies of *Pyrococcus furiosus* ferredoxin mutant with unfolding agent

To further probe the structure of *Pf* Fd D14C after addition of GdnHCl, a MCD spectra of *Pf* Fd D14C with the same concentration of GdnHCl was measured (**Figure 5.7**). MCD spectroscopy is the only way to find out whether the structure in presence of unfolding agent is similar to the native state of the proteins, and that would prove whether the protein is unfolded. From **Fig. 5.7**, the spectra in red colour belong to native *Pf* Fd D14C and acts as control whereas the blue colour spectra indicates behaviour of *Pf* Fd D14C in 6 M GdnHCl. It was observed that both absorbance of two spectra are almost identical and having significant signal at the near-UV range. This can be a sign that both proteins are still folded in structure. Apparently, the

guanidine is not doing the unfolding job as it should be since it only alters the protein conformation a little bit. It can be concluded that this unfolding intermediate state during the denaturation of the protein may be referred to as the molten globular state as it retains its native like structure. The small perturbations are probably consistent with the effect of the guanidine on the electrochemistry. The potential shifted by about 50 mV to a more positive potential with little loss in intensity.

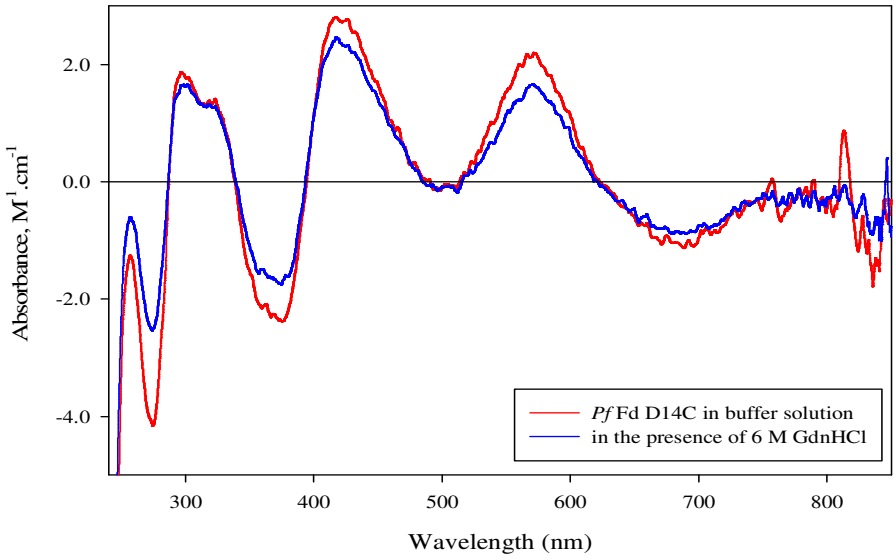

Figure 5.7. MCD spectra for native {4Fe-4S} *Pf* Fd D14C (210 μM) and {4Fe-4S} *Pf* Fd D14C in 6 M guanidine hydrochloride.

5.2.6 Behaviour of *Pyrococcus furiosus* ferredoxin mutant to pH variation: An electrochemical study

The inability of guanidine hydrochloride to unfold the protein significantly prompted an examination for the pH dependence of the system. We sought to answer the question whether the stability of native *Pf* Fd D14C molecular nature restrains it from interacting with any ligand in the system. Several claims in the literature regarding hyperthermophilic redox proteins response in different pH have suggested that we

should initiate an examination of this effect. [216-218] *Pf* Fd D14C was examined by cyclic voltammetry at various pH values using hydrochloric acid as the proton source. The voltammetric response is shown in **Figure 5.8**. It is apparent that increasing the pH, shifts the reduction potential to more positive value and leads to an increase in the peak current.

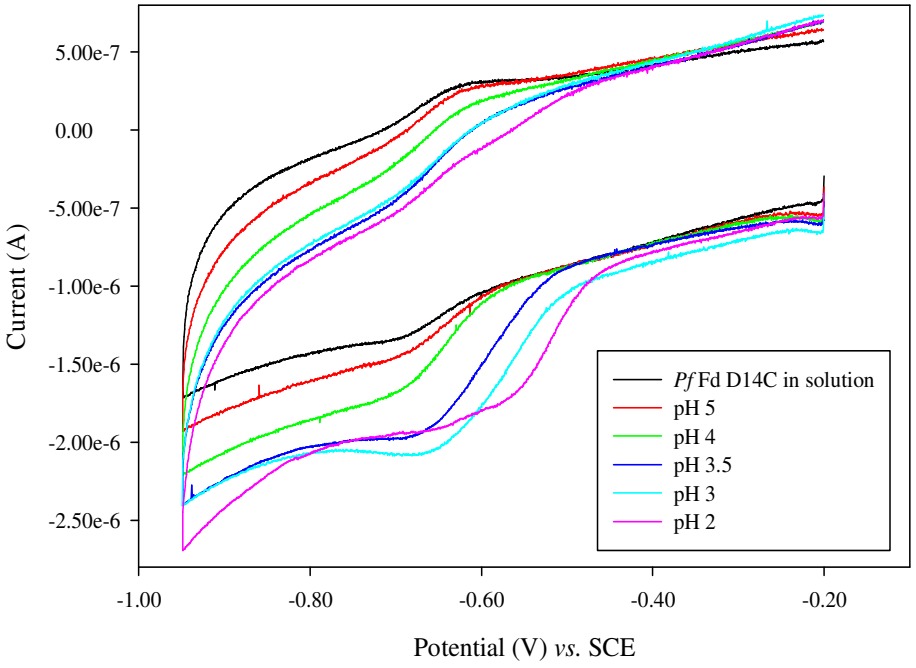

Figure 5.8. Bulk solution voltammetry of {4Fe-4S} ferredoxin extracts from *Pyrococcus furiosus* (100 μM) at different pH values adjusting with HCl (2 M) in 20 mM mixed buffer-0.1 M NaCl with 200 μM of polymyxin as co-adsorbate. Temperature 4 ºC, scan rate 5 mV.s^{-1}.

Above pH 4, there is not a significant shift in the redox potential, although the peak current for the redox process increases. Below pH 4, a shift in the peak potential becomes more apparent and further enhancement of the peak current for reduction is observed. At pH 2, there is an abrupt change in the shape of voltammogram indicative of the response of a new solution species.

A plot of $E_{1/2}$ *versus* pH is shown in **Figure 5.9**. As previously reported, the redox potential of *Pf* Fd D14C is virtually independent of pH at range 4.0-7.0. [219] However, when the pH of the solution is adjusted to 3 and below, the redox potential shows a dependence on pH. In the region of pH 4 to 2.5, the slope of the response is around 30 mV/pH, whereas in the region below pH 2.5, the pH decay is 180 mV/pH. The latter response may indicate formations of a fully protonated redox centre.

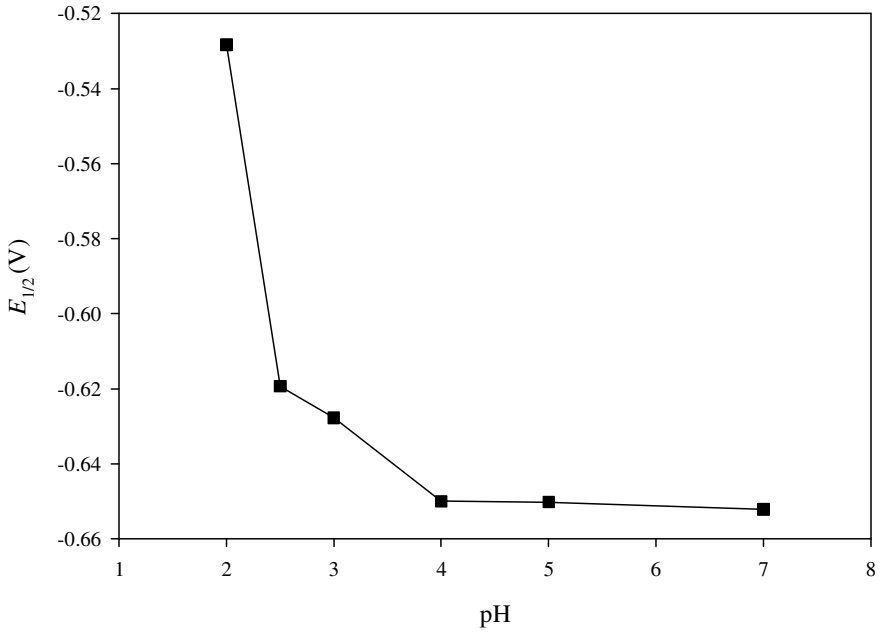

Figure 5.9. pH dependency studies of {4Fe-4S} ferredoxin extracts from *Pyrococcus furiosus* (100 μM) by HCl (2 M) in 20 mM mixed buffer-0.1 M NaCl with 200 μM of polymyxin as co-adsorbate. Temperature 4 ºC, scan rate 5 mV.s^{-1}.

Figure 5.10 displays the voltammogram of *Pf* Fd D14C at pH 2. At this pH, there is a dramatic shift in the redox process with a new peak appearing near -500 ± 5 mV *vs.* SCE. Thus, fully a 120 mV positive shift of the "parent" couple and with the peak current about twice that of the height of the modest pH form.

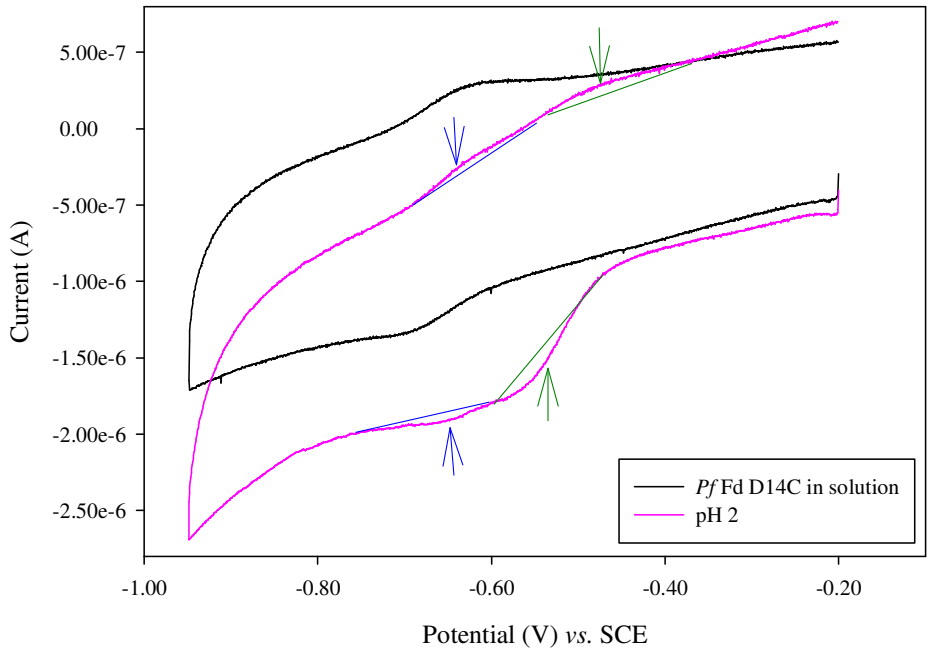

Figure 5.10. Bulk solution voltammetry of {4Fe-4S} ferredoxin extracts from *Pyrococcus furiosus* (100 μM) adjusted to pH 2 with HCl (2 M) in 20 mM mixed buffer-0.1 M NaCl with polymyxin as co-adsorbate. Temperature 4 ºC, scan rate 5 $mV.s^{-1}$.

It is known that one Fe can be removed from the native form of the protein to give a {3Fe-4S} system. It is possible that at low pH, protonation at the cysteinyl group leads to the loss of an Fe atom. However, what is remarkable is that addition of base to take the pH back to 7 fully restores the original redox response observed at pH 7 (see **Fig. 5.11**). It seems unlikely that Fe removed at low pH is quantitatively replaced upon restoring the pH to 7. If on the other hand, the protonation is association with a group at or close to the cubane core, full reversibility might be expected.

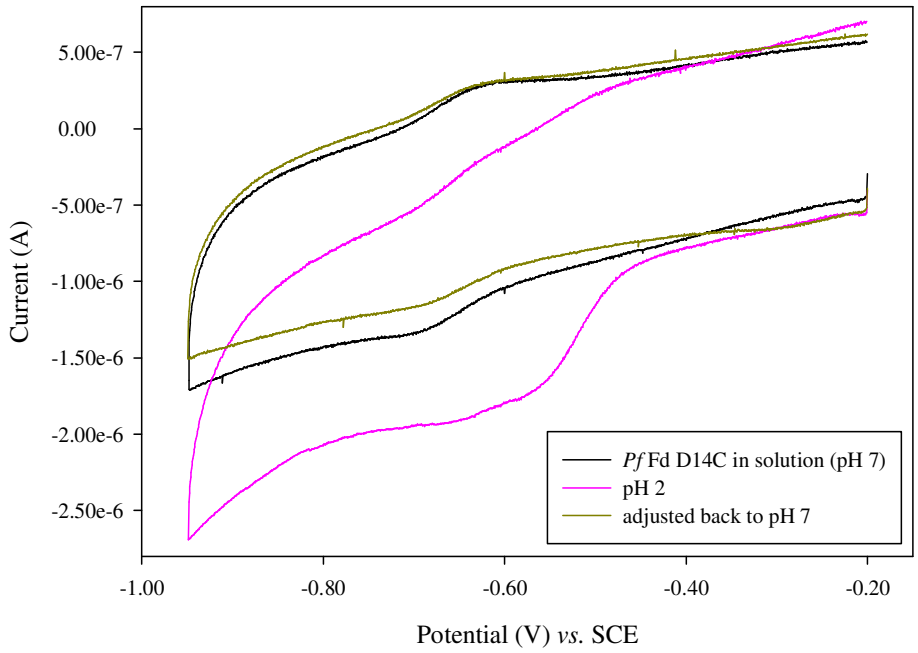

Figure 5.11. Bulk solution voltammetry of {4Fe-4S} ferredoxin extracts from *Pyrococcus furiosus* (100 μM) adjusted to pH 2 with HCl (2 M), re-adjusted back to pH 7 with NaOH (10 M) in 20 mM mixed buffer-0.1 M NaCl with 200 μM of polymyxin as co-adsorbate. Temperature 4 ºC, scan rate 5 mV.s^{-1}.

We have examined the effect of thiophenolate addition on the protein cyclic voltammetry at pH 2 *i.e.* when it is in the low pH form. The obtained voltammetry is shown in **Figure 5.12**. What is striking is that the thiophenol (PhSH) addition has a similar effect to that of addition of base. Thus, the redox response is similar to that observed at pH 7, although it is slightly shifted positive.

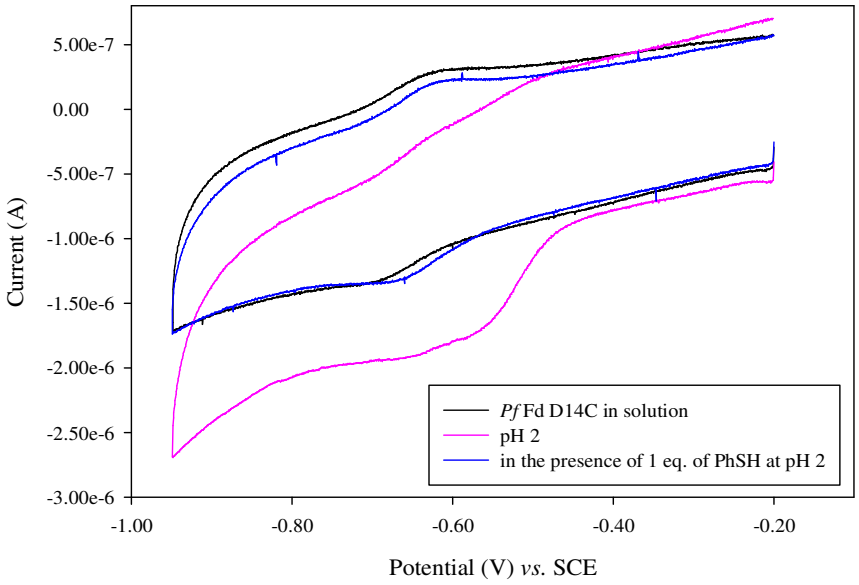

Figure 5.12. Bulk solution voltammetry of {4Fe-4S} ferredoxin extracts from *Pyrococcus furiosus* (100 μM) adjusted to pH 2 with HCl (2 M), follow by addition of thiophenol (20 mM) in 20 mM mixed buffer-0.1 M NaCl with 200 μM of polymyxin as co-adsorbate. Temperature 4 ºC, scan rate 5 mV.s^{-1}.

Taken together the reversible pH response and the thiolate response suggest the following chemistry taking place on the {Fe_4S_4} centre (summarised in **Scheme 5.2**):

i. There is a region where the effect of lowering the pH is to protonate a group near the complex and this has a small effect on the redox potential (pH 4 to 3).

ii. Under more acidic condition, pH 2, we suggest that a coordinated cysteine ligand is protonated at sulphur and is replaced as a ligand by water or a buffer anion.

iii. Addition of thiolate to a pH 2 form of protein leads to thiophenolate coordination of the iron by displacement of the solvent/buffer ligand with the

thiophenolate ligand. With similar electron donor effect of cysteine/cysteinyl (S^-) and thiophenolate ligand, there is little difference in the E^o value of the two forms at pH 7 (cysteine) and pH 2 (thiophenolate).

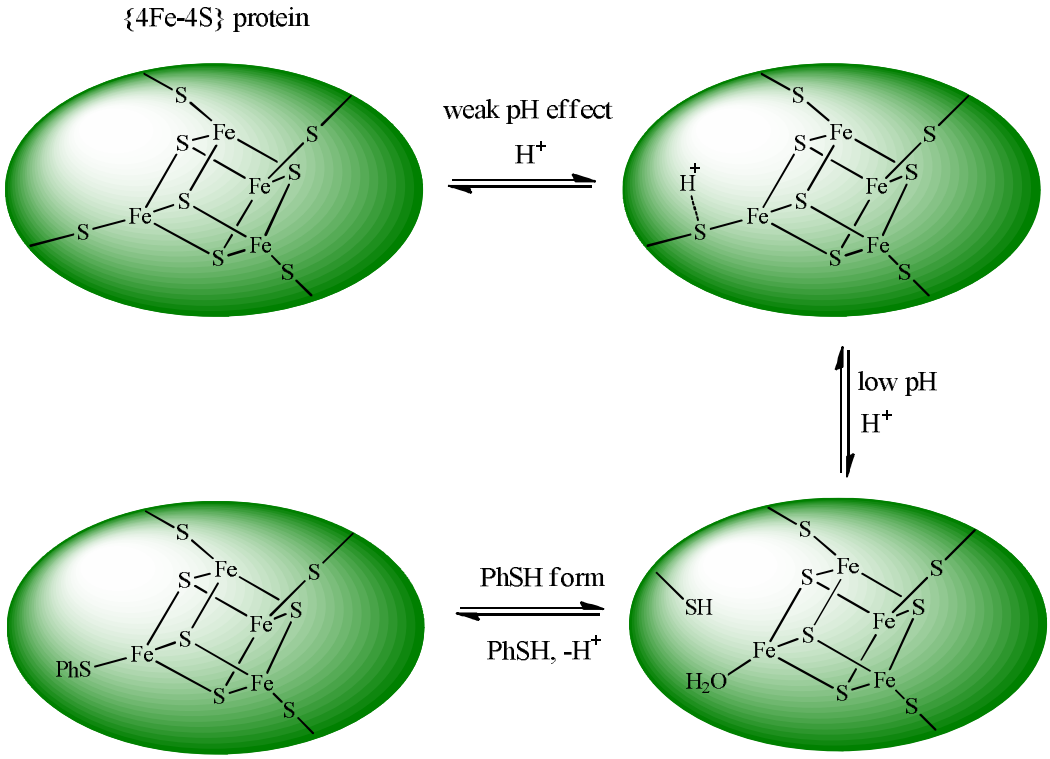

Scheme 5.2. Summary on chemistry taking place on the $\{Fe_4S_4\}$ centre based on reversible pH and the thiolate response.

We conclude from all the experiments on the mutant Pf Fd, that the Pf Fd is very robust but at low pH, it may well be possible to open up an iron site for sub-site binding, this remains to be explored. One limitation maybe the stability of the "ligating' complex at low pH. It might well be appropriate to explore the native three cysteine-one aspartate like the nature cluster with the synthetic sub-site.

5.2.7 Alternative reaction route based on *Desulfuricans africanus* ferredoxin

The seven-Fe ferredoxin from *Desulfuricans africanus* contains two clusters, one {3Fe-4S} and one {4Fe-4S}. Previous work by Armstrong and colleagues [192]have revealed three redox couples from the cyclic voltammogram obtained on the solutions for this ferredoxin. Two were assigned in each case to the $\{3Fe\text{-}4S\}^{1+/0}$ and $\{4Fe\text{-}4S\}^{2+/+}$ systems while the additional feature at lower potential was not characterised further. The {3Fe-4S} cluster in *Da* Fd contains seven Cys, the remaining four ligating a comparatively inert {4Fe-4S} cluster in the conventional way. An Asp is found in the central position that would normally be occupied by one of the four Cys ligating a $\{4Fe\text{-}4S\}^{2+/+}$ cluster. Thus, this protein, which is ready available in the laboratory has some similarity to the native form of *Pf* Fd. We have therefore looked at the properties of this material with the sub-site unit, $[Fe_2(CO)_5CH_3C(CH_2S)_2CH_2S][Na]$ (**9**).

Protein film voltammetry has been known for its ability to afford a rapid and precise way to induce and monitor interconversion between 3Fe ↔ 4Fe clusters, because the protein molecules under investigation are confined to the electrode surface and are therefore under tight potential control. The binding of an extra Fe metal to {3Fe-4S} cluster can be ascertained immediately from the appearance of a characteristic pair of redox signals through changes in the film voltammogram occurring, as the protein molecules attached to the electrode react with trace levels of Fe metal ion in the electrolyte. [207, 220] Voltammetry experiments now described explore further aspects to this chemistry. **Figure 5.13** shows the cyclic voltammetry of the {3Fe-4S} (refer as *Da* Fd(III))-{4Fe-4S} (refer as *Da* Fd(IV)) centre of the native protein. Two peaks are observed. **A** and **B** which have been attributable to oxidation of one electron reduction of the $\{3Fe\text{-}4S\}^{+1}$ system and one reduction of electron $\{4Fe\text{-}4S\}^{+1}$. [221, 222] Addition of ferrous ammonium sulphate, Fe(II) to the system results in loss of the $\{3Fe\text{-}4S\}^{+1/0}$

couple and formation of a new couple which overlaps with that of **B**. This is a sign to the conversion of the {3Fe-4S} system and additional {4Fe-4S} couple whose reduction occurs at potential slightly positive of **B**.

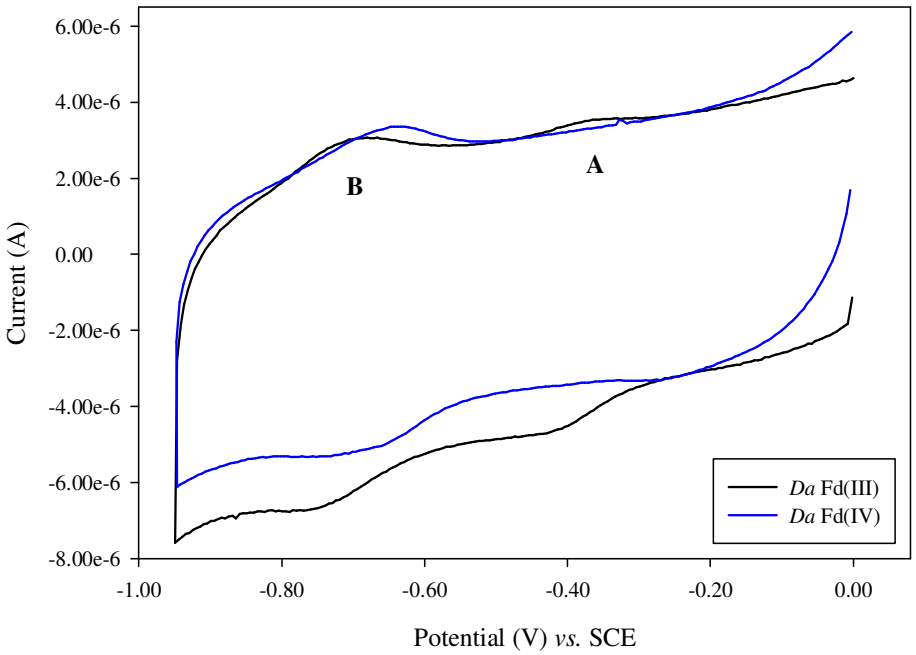

Figure 5.13. Protein film voltammogram for conversion of *Da* Fd(III) to *Da* Fd (IV), pH 7.0 in 20 mM mixed buffer-0.1 M NaCl with 200 μM of polymyxin as co-adsorbate. Temperature 4 ºC, scan rate 50 mV.s^{-1}. Ferrous ammonium sulphate (300 μM) is used as iron source.

In the doublet {4Fe-4S} cluster state of the protein from *Da* Fd formed by iron addition to the native sample, we added the complex **9**. **Figure 5.14** shows the response before and after addition of the sub-site. It appears that redox response of both cubane clusters in the protein is affected by the addition. A broad, ill-defined response is observed between -350 and -80 mV *vs*. SCE. A rather more defined signal is observed near -200 mV *vs*. SCE.

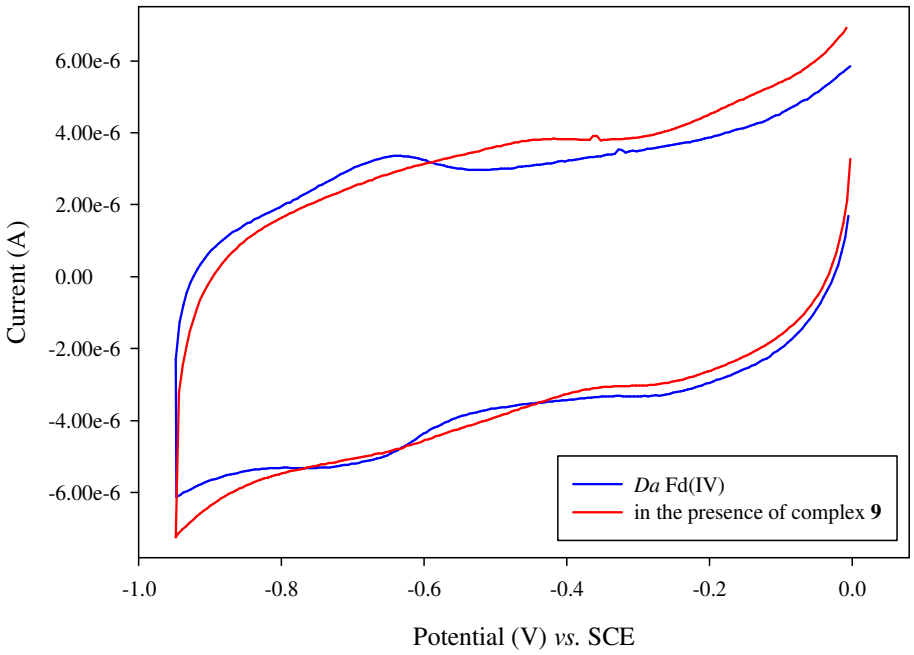

Figure 5.14. Protein film voltammogram of *Da* Fd (IV) (100 μM) react with $[Fe_2(CO)_5(CH_3C(CH_2S)_2CH_2S][Na]$ (**9**), pH 7.0 in 20 mM mixed buffer-0.1 M NaCl with 200 μM of polymyxin as co-adsorbate. Temperature 4 ºC, scan rate 50 $mV.s^{-1}$.

5.3 Final remarks

In this study, our attempt was to convert a protein bound $\{Fe_4S_4\}$ centre into H-cluster by addition of a synthetic sub-site. We have found that the mutant *Pf* Fd D14C containing {4Fe-4S} is very robust. It is not easily unfolded with GdnHCl but at low pH, it seems possible that chemistry at one of the irons can be carried out. The evidence of this is limited to an experiment which shows that thiophenolate at pH 2 restores the redox response of the cubane cluster to that observed at pH 7. We have pursued the possibility of adding a sub-site to a ferredoxin by utilising the ferredoxin from *Desulfuricans africanus*. We found that the doublet {4Fe-4S} protein appears to react with a synthetic sub-site but the protein film voltammetry is ill-defined. Nevertheless,

this looks as an attractive avenue to explore, particularly if we can couple this to FTIR spectroscopy.

5.4 Experimental

5.4.1 Bulk voltammetry and protein film voltammetry

All electrochemical operations were carried out using deionised water (Milipore, 18 $M\Omega.cm^{-1}$). Preparation and purification of the recombinant, reduced, {4Fe-4S} *Pyrococcus furiosus* ferredoxin (*Pf* Fd) mutant D14C was by Francis E. Jenney from Department of Biochemistry and Molecular Biology, University of Georgia, United States. Another type of {3Fe-4S} ferredoxin isolated from *Desulfovibrio desulfuricans* (*Da*Fd) was provided by Julea N. Butt from School of Chemistry, University of East Anglia, England.

A 20 mM mixed buffer system consisting of 5 mM of each acetate (acetic acid), Mes (2-[N-Morpholino]ethanesulfonic acid), Hepes (4-(2-Hydroxyethyl)piperazine-1-ethanesulfonic acid) and Taps (N-[Tris(hydroxymethyl)methyl]-3-aminopropanesulfonic acid) with 0.10 M NaCl as the electrolyte. Solutions were adjusted to the required pH with either NaOH (10 M) or HCl (2 M). Polymyxin B sulphate acts as co-adsorbate, was added to the buffers to give a final concentration of 200 $\mu g.mL^{-1}$. For bulk-solution electrochemistry, protein concentrations were typically 80-100 µM in 20 mM of mixed buffer system with 200 μM polymyxin to promote and stabilise the electrochemical response. All the experiments were carried out in a glove box (Belle Technology, Dorset, England) with O_2< 2 ppm. Cyclic voltammetry was carried out with an Eco-Chemie Autolab electrochemical analyser. Experiments were carried out in multipot cell which consisted of three individual pots readily connected to a central reference compartment, platinum counter electrode and working electrode.

The temperature of the cell was thermostated at 4 °C to optimise stability. The reference was an aqueous saturated calomel electrode (SCE) and was held at 20 °C. The pyrolytic graphite edge (PGE) electrode (area 0.10 cm^2) was prepared for protein application by polishing with aqueous alumina slurry (Buehler Micropolish, 3.0 µm) and sonicating extensively in water to remove traces of Al_2O_3. To prepare the films, a ~1 µL aliquot of ice-cold ferredoxin solution (typically 100 µM in 50 mM Tris (Tris(hydroxymethyl)methylamine), pH 7.6, 0.1 M NaCl with 200 $\mu g.mL^{-1}$ polymyxin as co-adsorbate) was applied to the surface of the electrode with a microsyringe (Hamilton). With this, protein film is built by electrostatic adsorption on the graphite edge working electrode.

5.4.2 Magnetic circular dichroism spectroscopy

Magnetic circular dichroism (MCD) spectroscopy is a well-established technique for the study of proteins. MCD spectroscopy measures the differences in the absorption of left-handed polarised light *versus* right-handed polarised light, which arise due to structural asymmetry when a strong magnetic field is induced in the sample. It is particularly used to gain information about the stoichiometrically measuring the tryptophan content of proteins and determining whether a protein is folded or unfolded. Ultra-violet (UV) MCD measurement was performed on a Jasco J-810 spectropolarimeter using a 1 mm path length cell. The nitrogen flow was fixed at 10 $L.min^{-1}$. The MCD spectrum was monitored over a variable wavelength scan (250-900 nm). The spectra was recorded in buffer solution at concentrations of about 200 μM of *Pf* Fd with the presence of unfolding agent guanidine hydrochloride. The MCD in milidegree (m.deg) obtained over the wavelength range is converted to molar ellipticity coefficients, M_θ and were calculated using equation shown in **Equation 5.1** where the ellipticity, θ is given in deg, concentration, c in $mol.L^{-1}$ and path length, *l* in cm, thus

giving deg.L.mol^{-1}cm^{-1} for M_θ. [223, 224] Ellipticity maxima, λ_{max} and ellipticity minima, λ_{min} are given in nm.

$$M_\theta = \frac{100 \times \theta}{c \times l}$$

Equation 5.1

Chapter 6

Visible light driven water splitting: A nano-photocathode for hydrogen production

This chapter concerns on the building of a photocatalysis system responsible for water splitting towards molecular hydrogen production. Herein we describe the construction of a nano-photocathode for dihydrogen production, which is based on a multi-layer array of indium phosphide quantum dots activated with a synthetic diiron catalyst related to the sub-site of [FeFe]-hydrogenase.

6.1 Background on light driven dihydrogen production

Consequences of the affects of fossil fuel shortage are already being felt economically and socio-politically. The global energy demand will continue to increase in the coming decades with the rise of world's population and its economic growth. [225-228] Thus, it is high time to find alternative, sustainable energy resources. Environmental concerns have provided additional motivation for scientists to move the world towards renewable, alternative forms of energy. The capture of sunlight and its conversion into readily available forms of energy may be able to satisfy mankind's energy demands of the future. Apart from solar heating where sunlight is used directly, sunlight is usually converted to electricity, a form of energy which is difficult to store and is best

consumed instantly when it is produced. Conversion of solar energy into dihydrogen, on the other hand, provides a solution to this problem. [151, 229-232]

To date, the production of molecular hydrogen has relied mainly on fossil fuels, a fact which makes the idea of its use as a clean fuel highly debatable. Reverse of **Equation 6.1** indicates the ideal route of dihydrogen production which is *via* the splitting of water, provided that the reaction could be driven directly by the action of light, dihydrogen could be produced and combusted in a truly cyclic process, with no waste product ever being formed. This dihydrogen production route remains as the ultimate model due to two advantages. Firstly is the raw material used, *i.e.* water is abundant and cheap; secondly, the overall process is non-polluting.

$$2H_2 + O_2 \leftrightarrow 2H_2O \qquad \textbf{Equation 6.1}$$

Since water does not absorb visible light, intermediates are needed to achieve the water photocleavage through a cyclic pathway. This perspective provides the motivation for the development of supramolecular systems capable of catalysing the light driven splitting of water, in which the illumination of a coloured compound acting as a photosensitiser can give rise to photoinduced redox processes. One of the main difficulties in achieving the splitting of water by light-induced charge transfer events is that the two half reactions are multi-electron processes. The generation of molecular hydrogen (**Eq. 6.2**) requires two and the oxidation of water (**Eq. 6.3**) releases four electrons. [233]

$$2H_2O + 2e^- \rightarrow H_2 + 2OH^- \qquad \textbf{Equation 6.2}$$

$$2H_2O \rightarrow O_2 + 4H^+ + 4e^- \qquad \textbf{Equation 6.3}$$

With the standard potential for **Equation 6.2** being -0.41 V *versus* saturated hydrogen electrode (SHE) and that for **Equation 6.3** being +0.81 V at pH 7, [234-236] this number of charges correspond to the most favourable thermodynamic conditions for the reaction in **Eq. 6.1**. In other words, photons with a minimum energy of 1.23 eV, which corresponds to wavelength, $\lambda < 1008$ nm could theoretically induce the cleavage of water. A promising way for light driven water splitting would be to mimic the molecular and supramolecular organisation of the natural photosynthetic system. The aim of these approaches is to develop catalytic systems that split water with sunlight and produce molecular hydrogen and oxygen, have high efficiency and long term stability. If such a system either biological, biomimetic or bioinspired can be developed, there is hope to use it on a larger scale to produce solar fuel.

6.2 Photocatalysis model systems

In driving any closed molecular hydrogen photogeneration cycle, new approaches should be considered that differ from the typical photochemical strategy of the last 30 years, [237] namely, the design of an excited state that efficiently performs both solar capture and catalysis. Not only are the issues of multielectron redox chemistry coupled to proton transport daunting catalyst design problems in their own right, but this chemistry must simultaneously be performed within an absorption manifold that matches the solar spectrum. [238]

The most prevalent approach to dihydrogen producing photocatalysis is the construction of a three-component system, supramolecular system which comprising a sensitiser to absorb light, a proton reduction catalyst and an electron relay to transport reducing equivalents from the sensitiser to the catalysts. The electron relay can potentially be eliminated if the photosensitiser is directly attached to the proton

reduction catalyst. The role of photosensitiser is to harvest the incoming light and to transfer the reduction/oxidation equivalent to a suitable catalyst, which has to be capable to store two electrons for the reduction and four electron holes for the oxidation reaction.

A common approach in the construction of such devices is the utilisation of new class of metals dyads designed to promote the light driven production of molecular hydrogen. [239-241] Ruthenium polypyridine complexes have been successfully used as a light harvesting unit in many light driven dihydrogen production systems. [242-245] Bipyridines, lanthanoid ions or transition metal complexes are used as electron mediators, amines and methoxybenzenes as sacrificial donors and noble metal complexes as proton reduction catalysts. [246-248] More recently, heterogeneous systems based on doped titanium dioxide, TiO_2 semiconductors have attracted a lot of attention in this field. To build intramolecular photoinduced catalysts, several biomimetic models of the [FeFe]-hydrogenases active site were covalently linked to the ruthenium photosensitiser or to the porphyrin derivatives.[249, 250] Of these photosystems, the first to demonstrably produce dihydrogen did not employ the linking of the photosensitiser to the diiron unit. The system designed by Sun and his co-workers [241] employed ruthenium tris-bipyridine, $Ru(bpy)_3^{2+}$ as a photosensitiser, which was reductively quenched by a thiocarbamate, to generate the highly reducing ruthenium mono cation, $Ru(bpy)_3^{+}$. This species in turn reduced a synthetic diiron sub-site, leadings to the electrocatalytic evolution of dihydrogen.

Beyond cost, all such systems suffer from having limited lifetimes, which may be, at least in part, attributed to the intrinsic reactivity of the organic N-ligands in the radical

anion form of the photoexcited state, and photodegradation pathways, which lead to photodestruction of the complexes. [251, 252]

6.3 Indium phosphide nano-crystals as photosensitiser

Over the past 25 years, colloidal III-V semiconductor nano-crystals have drawing much attention from the researchers, credited to their less ionic lattice, larger exciton diameters and reduced toxicity compared to other groups of semiconductor such as II-VI and IV-VI. [253, 254] Within the III-V groups, indium phosphide, InP is the most extensively studied semiconductor material, due to its bulk band gap of 1.35 eV, which enables nano-crystals to have photoluminescence emission wavelengths ranging from blue to the near infrared. In other word, electrons in InP can jump from valence band (VB) to conduction band (CB) after absorbing the photon from the light source. The band gap in semiconductor, which serves as a measure of the excitability of molecule is referring to the energy difference between the HOMO and LUMO. This large band gap characteristic also makes this type of semiconductor known as quantum dots, where the sizes of the crystals control the band gap or the energy level of the material itself. These nano-crystals are promising alternatives to the frequently used CdSe-based nano-crystals for applications such as bio-labelling, light emitting devices (LEDs), photovoltaic cells and quantum dot lasers. [255, 256]

In context of our interest in photoelectrochemical dihydrogen production, we became intrigued by the possibility to covalently link the indium phosphide nano-crystals to a biomimetic model of the [FeFe]-hydrogenase active site in an attempt to afford dihydrogen production by light.

Iron-sulphur carbonyl assemblies related to the sub-site of [FeFe]-hydrogenase have been shown to electrocatalyse the reduction of protons to dihydrogen under dark conditions at potentials between -0.7 and -1.4 V *versus* the standard calomel electrode (SCE) in non-aqueous electrolytes. [5, 257] Of these assemblies, $Fe_2(\mu\text{-}S_2)(CO)_6$ is chosen owing to the presents of sulphide bridges that are potentially capable of binding to indium phosphide as a catalyst for photoelectrochemical reduction of protons in a solid-state assembly, and a modest reduction potential of -0.90 V *versus* SCE. Furthermore, it is worth mentioning that catalysis of H_2 production upon electrochemical reduction of $[Fe_2(\mu\text{-}S_2R)(CO)_4L_2]$ (L = CO or PMe_3) complexes in weak acid solution takes place at potentials negative to −2.00 V *versus* $Fc^{+/0}$, which preclude these systems from any applications even in light driven cycles.[86, 258]

6.4 Results and Discussion

Solar hydrogen from water is clearly attractive as a clean energy vector and there have been many attempts to construct viable molecular and biomolecular devices for photohydrogen production. [259] Here we show that an inexpensive and environmentally benign inorganic light harvesting nano-array can be combined with an inexpensive and element abundant electrocatalyst. This provides a stable photoelectrochemical platform for dihydrogen production. The device is constructed by first building-up, layer-by-layer, a cross-linked indium phosphide nano-crystal array and incorporating $Fe_2(\mu\text{-}S_2)(CO)_6$ (**12**) which has sulphide bridges capable of binding to InP.

6.4.1 Photolysis of $Fe_2(\mu\text{-}S_2)(CO)_6$

The synthesis of $Fe_2(\mu\text{-}S_2)(CO)_6$ (**12**) has been described in **Chapter 3**, whereas InP nano-crystals were prepared by Professor Thomas Naan's research group according to their previous publication procedure as 5 nm particles with an emission band at 600 nm,

and full width at half maximum (FWHM) of about 80 nm. [260, 261] These nano-crystals were dispersed in toluene using hexadecylamine (HDA) and the zinc salts of long chain fatty acid (stearic and undecanoic acid) as surface ligands.

The photolysis of $Fe_2(\mu\text{-}S_2)(CO)_6$ itself has been studied previously. [262, 263] It was found that in the absence of a substrate to trap the anion form of $Fe_2(\mu\text{-}S_2)(CO)_6$, dimerisation of the complex will lead to $Fe_4S_4(CO)_{12}$, a black air-stable crystalline solid (**Scheme 6.1**).

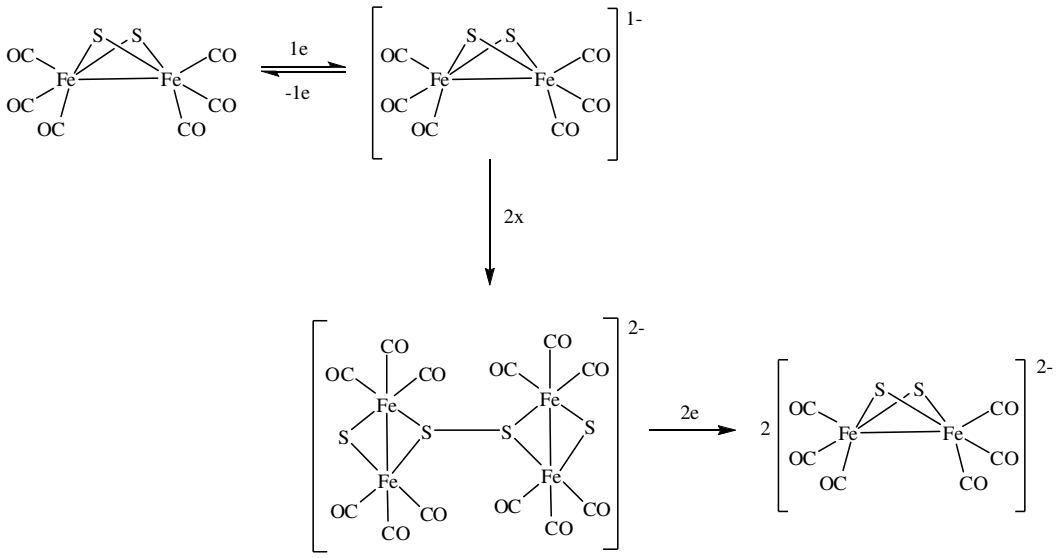

Scheme 6.1. Behaviour of $Fe_2(\mu\text{-}S_2)(CO)_6$ (**12**) in bulk electrochemistry leads to dimerisation.

It is also had been reported that photolysis of $Fe_2(\mu\text{-}S_2)(CO)_6$ at about 450 nm wavelength in the absence of potential ligands [264] cleanly forms the cubane cluster $Fe_4S_4(CO)_{12}$. [265] For our experiment, we used a home built high-power light emitting diode array with wavelength 395 nm to perform the irradiation. Photolysis study of

$Fe_2(\mu\text{-}S_2)(CO)_6$ (**12**) was carried out in toluene under the illumination of light source (λ = 395 nm) and the changes is monitored with FTIR (**Figure 6.1**). Each spectrum was recorded at two to five minutes interval for two hours. As the experiment time passed, the parent peaks for complex **12** at υ(CO)/cm^{-1} 2081, 2040 and 2002 were slowly depleted and shifted ~ 20 cm^{-1} to lower frequencies which lead to new peaks at 2062, 2019 and 1983 cm^{-1}, respectively. Nevertheless, the shifting process is gradually which indicates dimerisation of $Fe_2(\mu\text{-}S_2)(CO)_6$ to $Fe_4S_4(CO)_{12}$ is happening at a slow pace. It can be concluded that light source at lower wavelength contributes to dimerisation of the complex **12** as well, but the rate is very slow.

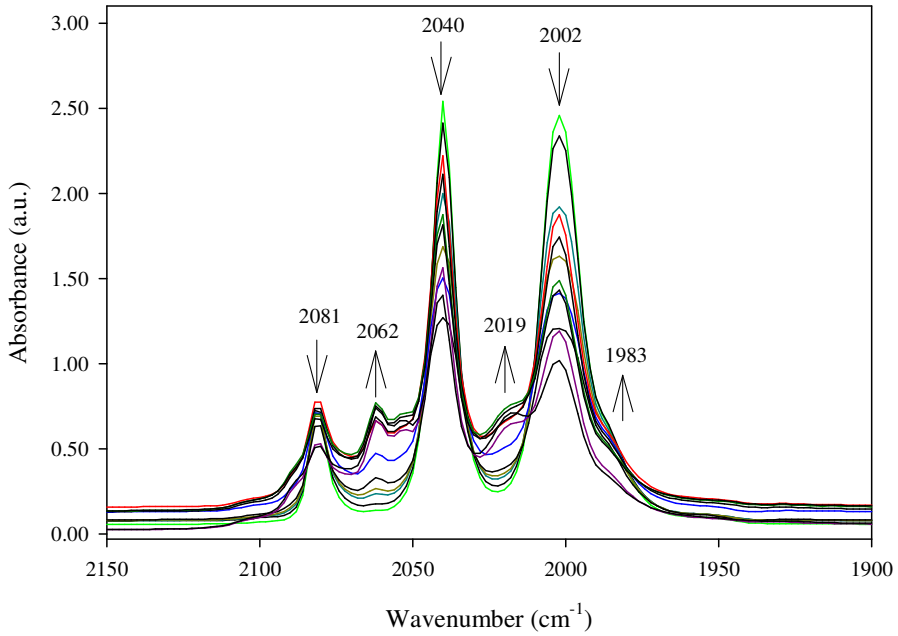

Figure 6.1. FTIR spectra of $Fe_2(\mu\text{-}S_2)(CO)_6$ (**12**) in toluene, continuously exposed to light emitting diode at 395 nm.

6.4.2 Protonation studies on $Fe_2(\mu\text{-}S_2)(CO)_6$

A cyclic voltammogram of $Fe_2(\mu\text{-}S_2)(CO)_6$ in a acetonitrile electrolyte is shown in **Figure 6.2**. One quasi irreversible reduction step is observed which corresponds to ½$[Fe_4S_4(CO)_{12}]^{2-}$. The same results have been reported by Al-Ani and Pickett [172] where they identified the present of the dimer complex as the primary product in the cyclic voltammetry. The IR spectra taken after electrolysis which carried out at a potential just negative of the reduction potential gives an IR spectrum corresponding to the formation of $[Fe_4S_4(CO)_{12}]$.

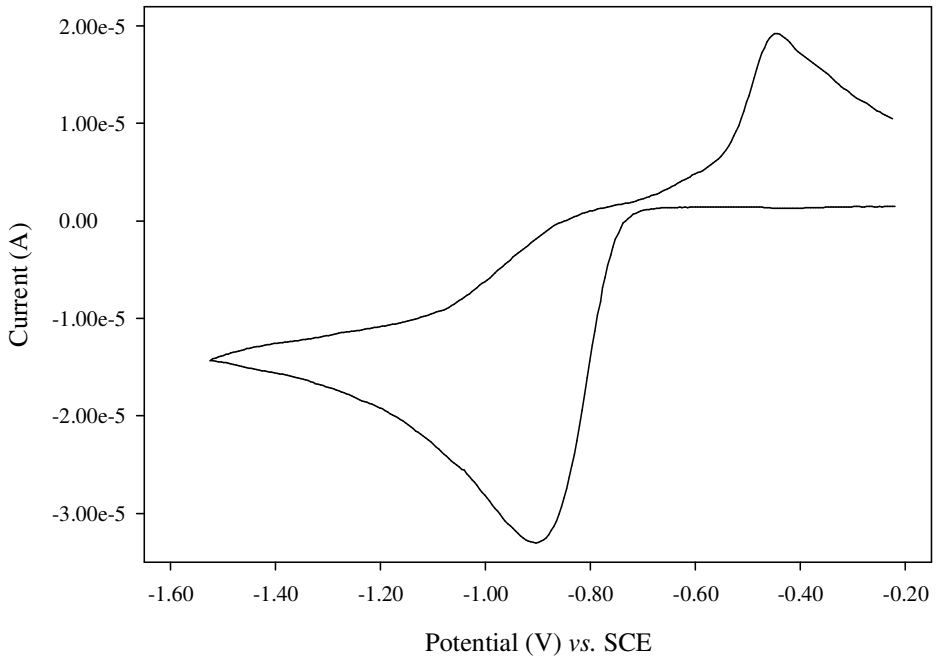

Figure 6.2. Cyclic voltammogram of $Fe_2(\mu\text{-}S_2)(CO)_6$ (**12**) (3 mM, 0.2 M $[NBu_4][BF_4]$ in acetonitrile, 50 $mV.s^{-1}$).

Figure 6.3 displays the behaviour of $Fe_2(\mu\text{-}S_2)(CO)_6$ in the presence of *p*-toluenesulfonic acid (TsOH) at different concentrations and its changes is monitored with cyclic voltammogram. With the existence of proton source in the system, two

phenomenon were expected to be occurred, either proton reduction or protonation of the iron complex. The proton reduction mechanism catalysed by chemical complexes is either an electron transfer, which increases the electron density at the metal core so that a subsequent proton transfer can occur, or a protonation step which causes a positive shift of the redox potential of the compound, thus facilitating a subsequent electron transfer. In order to protonate (usually at the Fe-Fe bond), the diiron complexes must be sufficiently electron-rich, which can be achieved by the substitution of donor ligands (*e.g.* CN^-, PMe_3, CNR) for carbonyls in the coordination sphere. The inevitable consequence of this is that the complexes become difficult to reduce, so that the positive potential shift resulting from protonation is (partly or totally) consumed to compensate for the negative potential shift, due to the presence of the electron releasing ligands. [86]

Under acidic conditions, the CV illustrates a characteristic increases in the current as the concentration of acid is increasing, confirming the catalytic behaviour of the $Fe_2(\mu\text{-}S_2)(CO)_6$ complex for dihydrogen evolution. The current response as a function of the acid concentration reaches a limit of about 2-3 times the peak current in the absence of acid. Upon addition of high equivalents acid, the primary reduction of $Fe_2(\mu\text{-}S_2)(CO)_6$ becomes chemically irreversible indicating that the reduced form of these complexes react with protons on the voltammetric time scale. And again, the reduction wave increases with increasing acid concentration, suggesting a catalytic proton reduction. Nonetheless, no improvement toward more positive potentials is observed and the reduction signal splits into two, indicating that the complex has to be reduced first to accept a proton, and this protonated complex can then be reduced a second time to evolve dihydrogen. Focusing on the $\{Fe_2S_2\}$ core, the S-S and the bent Fe-Fe bonds of

the molecule, it was not at all clear at which site a given reagent would be expected to attack (**Scheme 6.2**).

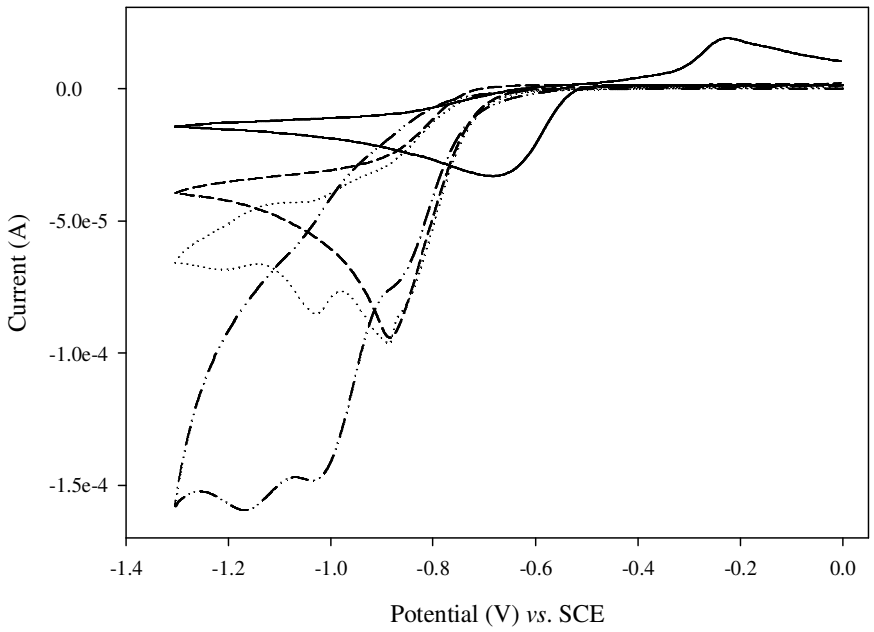

Figure 6.3. Cyclic voltammogram of $Fe_2(\mu\text{-}S_2)(CO)_6$ (**12**) (3 mM, 0.2 M $[NBu_4][BF_4]$ in acetonitrile, 50 $mV.s^{-1}$) in the absence (—) and in the presence of TsOH: (---) 1 equivalent; (···) 2 equivalents; (–··–) 8 equivalents.

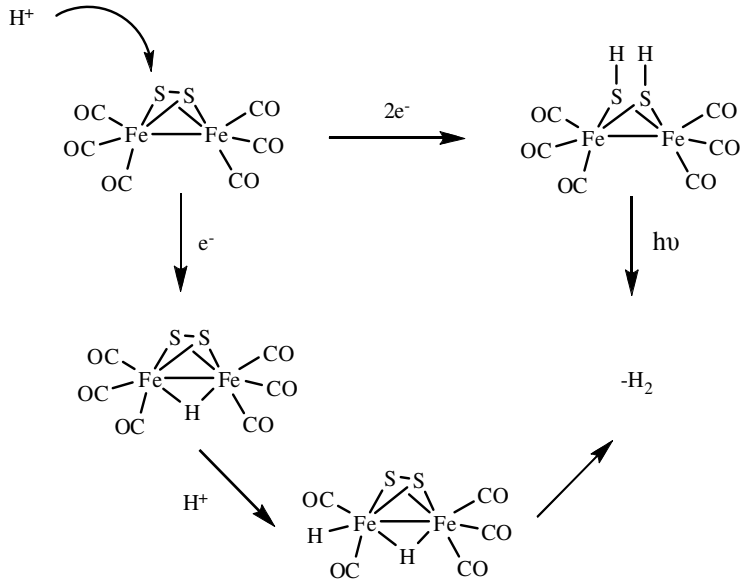

Scheme 6.2. Schematic diagram on protonation mechanism for $Fe_2(\mu\text{-}S_2)(CO)_6$ (**12**).

6.4.3 Photoluminescence studies of InP with $Fe_2(\mu\text{-}S_2)(CO)_6$

The original idea on constructing photocathode responsible for water splitting using visible light come across when we found the fluorescence of InP nano-particles in dispersion in toluene is slowly quenched in the presence of $Fe_2(\mu\text{-}S_2)(CO)_6$. This quenching is indicative of the binding of the complex **12** sub-site to the InP photosensitiser and the electron transfer to the sub-site. **Figure 6.4** shows the temporal evolution of the photoluminescence intensity of the InP nano-crystals when exposed to $Fe_2(\mu\text{-}S_2)(CO)_6$ in toluene. The response is consistent with the slow exchange of surface ligands with the sub-site analogue, giving rise to a Förster Resonance Energy Transfer (FRET). From here we know that InP acts as a "donor" molecule, absorbs a photon and transfers the energy non-radioactively to the "acceptor" molecule, which in this case is the $Fe_2(\mu\text{-}S_2)(CO)_6$. The photoluminescence of the quantum dots was completely quenched when the system was equilibrated and a sufficient concentration of the sub-site analogue was present.

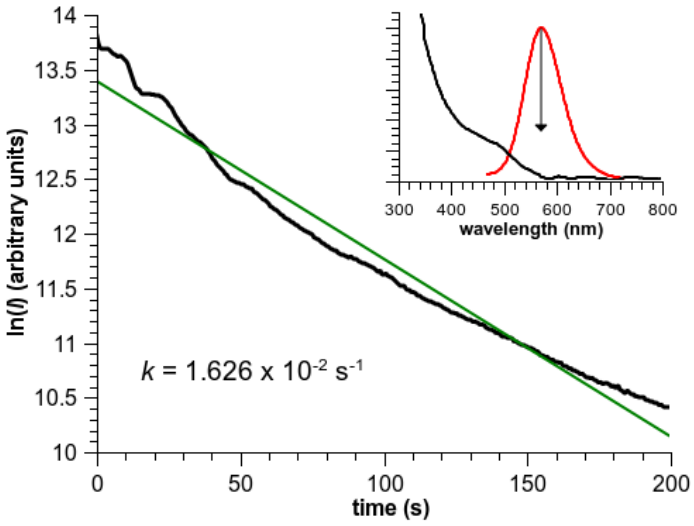

Figure 6.4. Luminescence quenching of InP quantum dots by $Fe_2(\mu\text{-}S_2)(CO)_6$(**12**)in toluene. The process follows roughly a first-order rate law with rate constant k. Inset: UV/vis. absorption and photoluminescence spectrum of InP quantum dots in cyclohexane.

6.4.4 Photolysis studies on mixture of InP with $Fe_2(\mu\text{-}S_2)(CO)_6$

Photolysis of $Fe_2(\mu\text{-}S_2)(CO)_6$ in the presence of InP were studied by using FTIR to examine the changes of the mixture under the illumination of light source with wavelength 395 nm. Within an hour of the experiment time, parent peaks responsible to $\upsilon(CO)/cm^{-1}$ for complex **12** had shifted to lower frequency about 7 cm^{-1} for each peaks (**Figure 6.5**). These new peaks at 2074, 2034 and 1995 cm^{-1} were different from what has been observed previously in $Fe_2(\mu\text{-}S_2)(CO)_6$ alone under the same experimental setup. It is believed, in the presence of InP, the dimerisation of $Fe_2(\mu\text{-}S_2)(CO)_6$ to $Fe_4S_4(CO)_{12}$ is not possible, possibly, the anion state of $[Fe_2(\mu\text{-}S_2)(CO)_6]^-$ is suggested stabilised. This again proved the binding of the complex **12** to the InP photosensitiser is applicable. **Scheme 6.3** indicates the possible reaction happening inside the infrared cell and the explanation on the electron flow will be discussed in the later section.

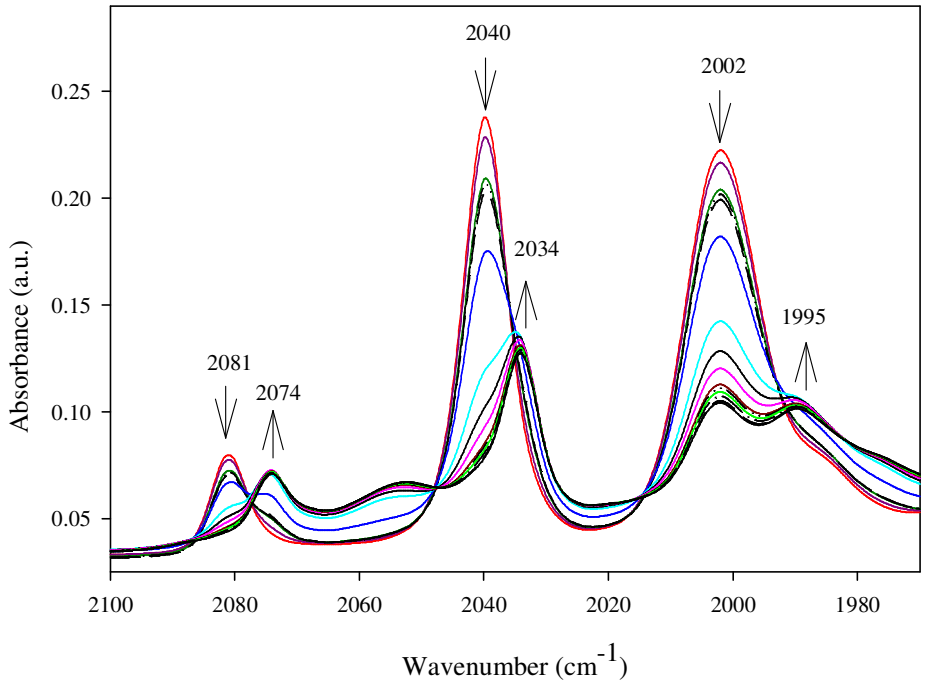

Figure 6.5. FTIR spectrum of InP with $Fe_2(\mu\text{-}S_2)(CO)_6$ (**12**) in toluene, continuously exposed to light emitting diode at 395 nm.

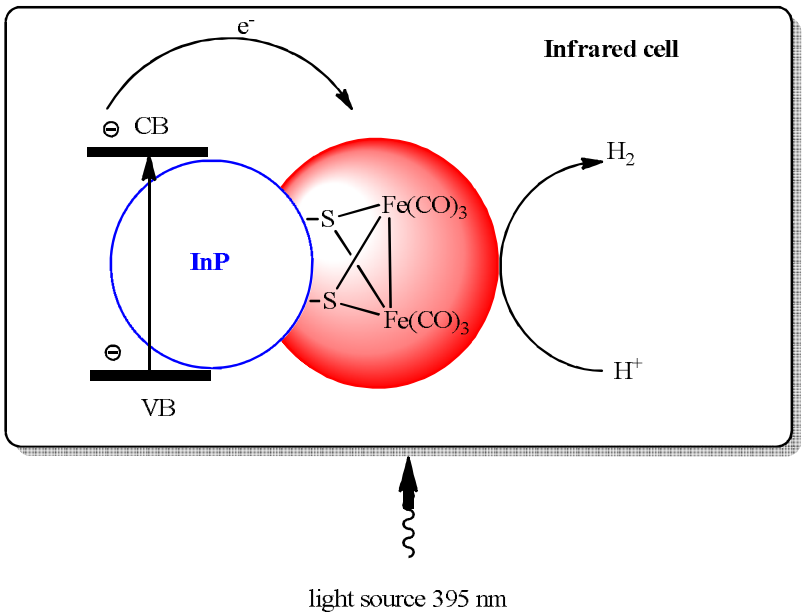

Scheme 6.3. Suggested electron flow under photolysis of InP with $Fe_2(\mu\text{-}S_2)(CO)_6$ (**12**).

6.4.5 Investigation on nano-photocathode

The nano-cathode array was assembled in the following fashion. Gold electrode was first modified by adsorbing a monolayer of 1,4-benzene dithiol which enabled the binding of a primary layer of the InP nano-crystals to the gold. The role of 1,4-benzene dithiol here is to act as linker. One side of its thiol group (S^-) is attaches to the gold surface whereas the other side is binds to InP. Layer-by-layer build-up of the nano-particle assembly was achieved by alternate exposure to the dithiol and the nano-crystal solutions. Finally, the $Fe_2(\mu\text{-}S_2)(CO)_6$ cluster was introduced onto the assembly by exposure of the modified electrode to a solution of $Fe_2(\mu\text{-}S_2)(CO)_6$ in toluene followed by thorough rinsing with toluene. **Figure 6.6** shows a schematic representation of the modified gold electrode.

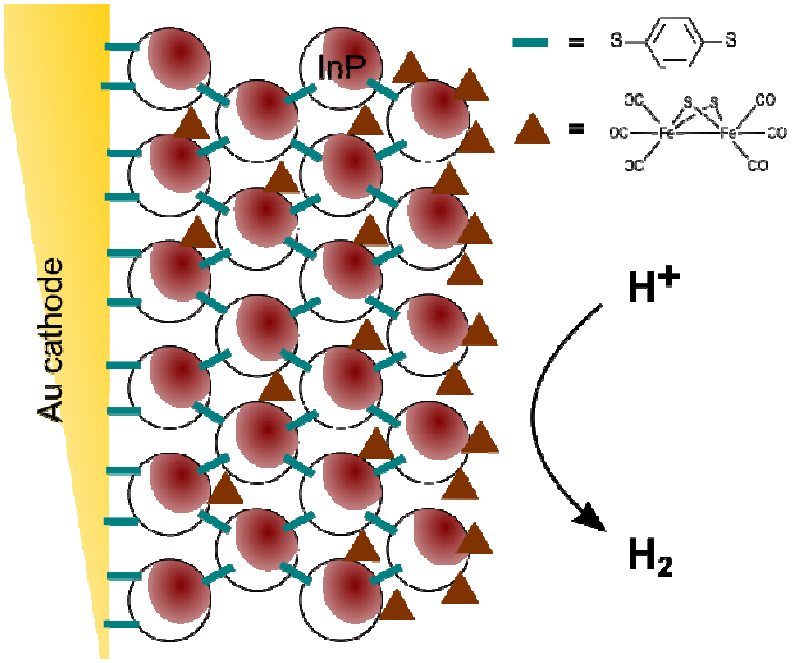

Figure 6.6. Schematic cross-section of InP nano-crystal modified gold electrode with adsorbed/intercalated $Fe_2(\mu\text{-}S_2)(CO)_6$ (**12**) sub-site analogue.

6.4.5.1 Fourier transforms infrared spectroscopy

The presence of the $Fe_2(\mu\text{-}S_2)(CO)_6$ sub-site absorbed within the assembly was confirmed by (diffuse) reflectance FTIR spectroscopy. **Figure 6.7** shows the carbonyl stretching region for the parent complex in solution (cyclohexane as solvent) and that for the bonded sub-site. It is found that when $Fe_2(\mu\text{-}S_2)(CO)_6$ bonded to InP nano-crystal in the assembly, the spectra exhibited abnormal infrared effects (AIREs), a term which introduced by Sun and his co-workers during their studies in deposition of nano-metre thin film on various metal electrodes. [266] On each occasion, when CO adsorbed on electrodes of these nano-materials, it will give rise to this abnormal infrared characteristic, in comparison with normal IR spectra for CO adsorbed on a bulk platinum electrode, where the direction of absorbed CO bands is completely inverted. The "inversion" of the spectrum is a consequence of a surface enhanced phenomenon

associated with the IR active molecule bound to conducting nano-particles. [267, 268] There is some broadening of bandwidth but a minimal shift in the carbonyl absorption frequencies, suggesting the sub-site analogue is weakly chemisorbed within the array. The bandwidth broadening in FTIR absorption enhancement in AIREs is related to the surface of material at the nano-metre scale, most probably interconnected to the film thickness and its structure. On a different work performed by Sun and co-workers, they have theoretically simulated the transformation of these abnormal IR properties by considering the interparticle interaction and electron-hole damping between those nano-islands and CO molecules. [269] It may be nevertheless pointed out that, it is still far away from completely understanding the mechanism of the transformation of anomalous IR properties involved nano-structured films assembly. Further experimental and theoretical studies are still required to gain more insight into the origin of the anomalous IR properties of the materials.

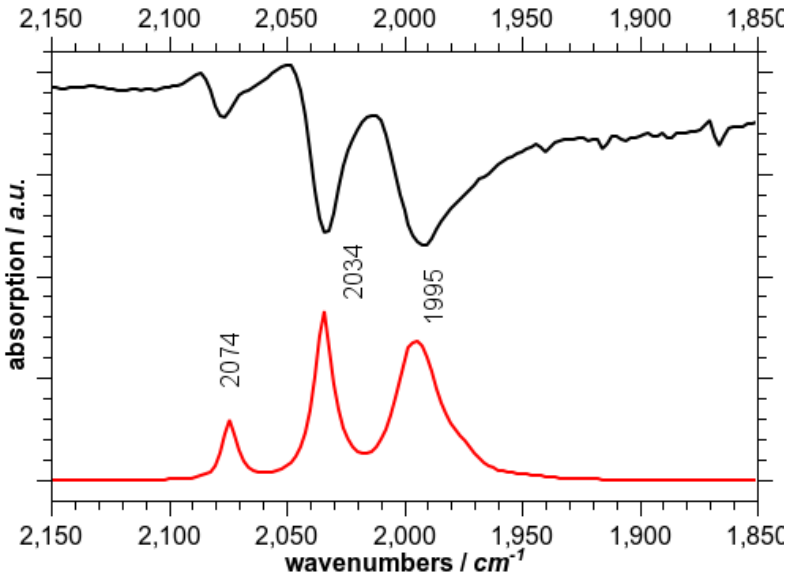

Figure 6.7. FTIR spectra of the carbonyl stretching region of the $Fe_2(\mu\text{-}S_2)(CO)_6$ (**12**) sub-site in solution (red) and bound to the InP nano-particle film (black). The "inversion" of the spectrum is indicative for CO bound to conducting nano-particles. [267, 268]

6.4.5.2 Photocurrent measurement

Figure 6.8 displays the photocurrent obtained at an InP assembly (10 layers) containing the $Fe_2(\mu\text{-}S_2)(CO)_6$ electrocatalyst upon illumination in 0.1 M aqueous $Na[BF_4]$ at pH 7, at -400mV *versus* {Ag/AgCl - 3M [NaCl]}. Each measurement at different potentials (-100 to -700 mV) also displays the same pattern for the photocurrent graph. The photocurrent was measured at a 30 seconds time frame. For the first ten seconds, no light is illuminated towards the modified gold electrode. Thus, there is no significant activity in the measured photocurrent. When the light emitting diode with wavelength 395 nm is illuminate, a noteworthy current is recorded, indicating electron is transferring from valence band to conduction band after receiving the photon from the light source. When the light is switched off, the current drops.

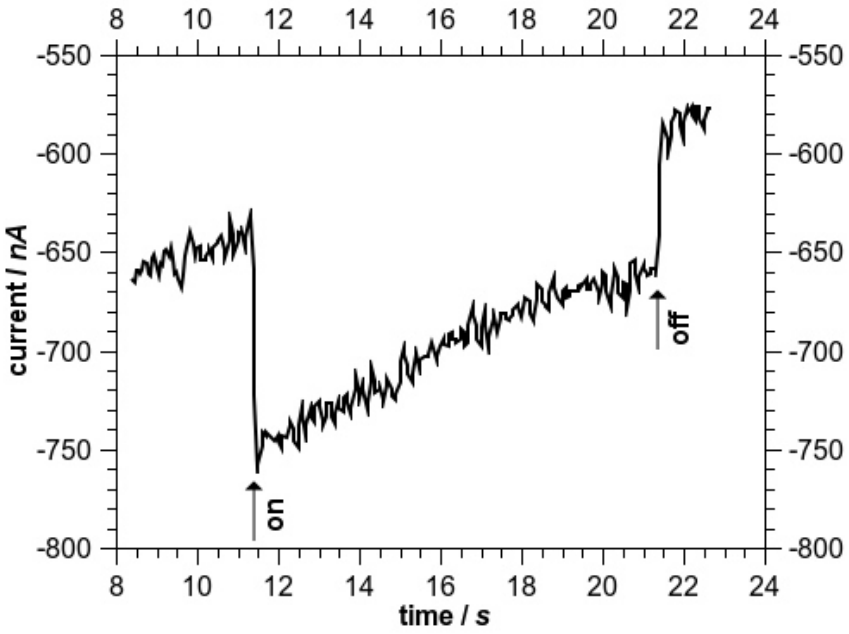

Figure 6.8. Photocurrent measured at a bias potential of -400 mV *vs.* Ag/AgCl in 0.1 M $Na[BF_4]$ under illumination with a 395 nm light emitting diode. Electrode area was 0.40 cm^2.

Figure 6.9 shows the photocurrent obtained at various bias potentials for the InP catalyst electrode array and for appropriate controls. Again, from this it is clear that a significant photoelectrocatalytic current is only observed with the complete InP catalyst assembly. Notably, the maximum photocurrent occurs at a potential over -250 mV more positive than the H_2/H^+ couple at pH 7. The current decreases after this optimum potential. The photocurrent observed at the blank gold electrode and the InP array can be attributed to the well documented photoelectric effect. [270] The background cathodic dark current is most likely caused by reduction of oxygen traces in the electrolyte.

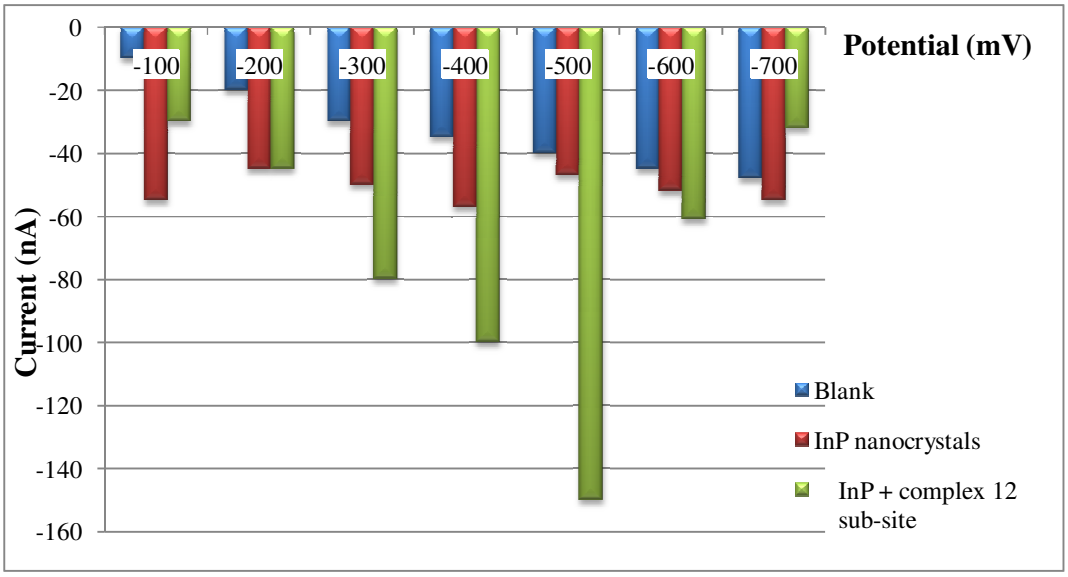

Figure 6.9. Photocurrent response at different bias potentials, electrode area 0.40 cm^2.

6.4.5.3 Electrolysis

A photocurrent could be sustained for at least one hour without degradation, at a bias potential of -400 mV (in practise, a slight enhancement of current, *I* was observed at longer times), thereby, demonstrating the robustness of the system. We used a closed cell, as depicted in **Figure 6.10**, for the bulk electrolysis which allowed us to analyse the gas headspace by gas chromatography. The right hand side of the same figure

shows the energy diagram of the photocathode and the suggested mechanism for the photocatalytic reduction of protons.

After the passage of 2.58 µC (±10 %) we detected a substantial quantity of 16.2 nano moles of H_2 in the headspace above the electrolyte by gas chromatography, which corresponds to a current yield of approximately 60%.

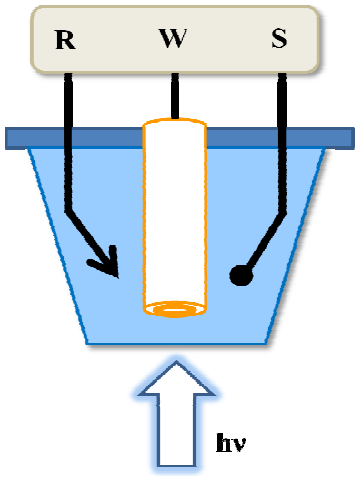

Figure 6.10. Schematic representation of the closed electrochemical cell used (R = reference electrode, W = working electrode and S = secondary electrode).

Scheme 6.4 depicts the energy levels of the photoproduction of H_2 during electrolysis process. The mechanism of the photoproduction of H_2 most likely involves the absorption of incident light by the InP nano-crystals and excitation of an electron into the conducting band of the nano-particles. Subsequently, electrons are transferred from the conduction band which lies at *ca* -1.0 V *versus* Ag/AgCl [271] into the LUMO of the catalytic sub-site *ca*. -0.90 V *versus* Ag/AgCl, thereby effecting the reduction of protons. The intimate mechanism of the electrocatalytic molecular hydrogen is likely to involve Fe-H and/or S-H intermediates. [109, 272] The holes generated in the valence band

of the nano-crystals are immediately filled by electrons available from the underlying gold substrate held at -400 mV *versus* Ag/AgCl.

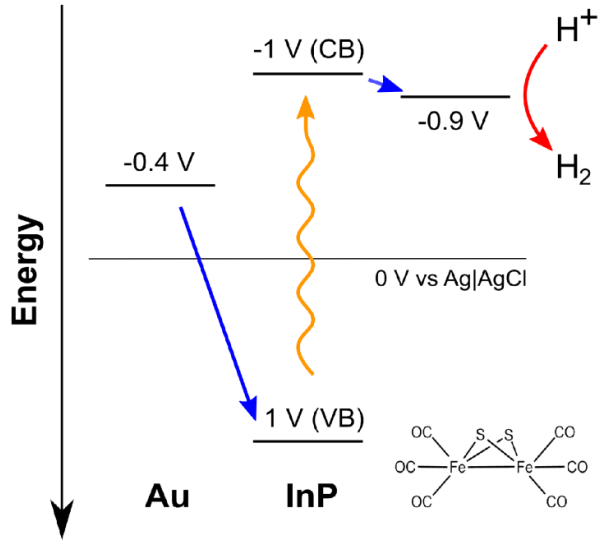

Scheme 6.4. Energy levels of the photoproduction of H_2 during electrolysis process (respective redox potentials of the components of the photocathode). Potentials are versus Ag/AgCl-3M NaCl, CB = conduction band, VB = valence band.

6.5 General conclusion

In conclusion, solar generation of dihydrogen from water remains a world class problem; the elaboration of efficient and economically viable photocatalyst remains a realistic goal for inorganic chemists but it is obvious that mechanisms of H_2 production is still insufficiently understood. Nevertheless, in this study, we have shown that it may be possible to construct a relatively robust and efficient system to the photoelectrochemical production of dihydrogen. The system does not rely on excited states of organic molecules/ligands, unlike most of the state of the art approaches. The whole system comprises of inexpensive and non-toxic elements and may be a promising alternative for the inexpensive production of dihydrogen.

6.6 Experimental

6.6.1 General

Electrochemical measurements were made using a HEKA Electronics (Germany) potentiostat type PG 310, photoelectrochemical experiments were carried out in an aqueous 0.1 M $Na[BF_4]$ electrolyte, under dinitrogen, in a two-compartment cell at ambient temperature. The platinum secondary electrode was separated from the main compartment of the cell by a frit, so that oxygen produced there did not intermingle with molecular hydrogen produced at the working electrode.

Working electrodes were prepared by vapour deposition of gold onto glass slides to a thickness of 200 nm. These were thoroughly rinsed with ethanol and dried.

The photoluminescence of the quantum dots was recorded on a FluoroLog 3 spectrometer from Horiba Jobin (UK). Irradiation was performed using a home built high-power light emitting diode array. Reflectance FTIR spectra were recorded on a Perkin Elmer BX single beam spectrometer, using gold disc electrodes modified with the indium phosphide catalyst array. Dihydrogen was measured by gas chromatography using a Hewlett Packard 5890 series II GC with a thermal conductivity detector (TCD) and employing a molecular sieve 5A (80-100 mesh), 2 m column, run at 60 ^{o}C with argon as the carrier gas.

6.6.2 Synthesis of indium phosphide nano-crystals

The synthesis of indium phosphide nano-crystals were carried out by Thomas Naan's research group. The details of the synthesis have been reported previously. [260] Indium chloride (0.1 mmol, 22 mg), stearic acid (0.1 mmol, 28.5 mg) together with zinc undecylenate (0.1 mmol, 43 mg) and hexadecylamine (HDA) (0.2 mmol, 48 mg) were

mixed in a 50 mL two-necked flask with ODE or methyl myristate (3 mL). The flask was repeatedly evacuated and re-filled with dinitrogen gas to provide a water and oxygen-free reaction atmosphere. Then, the solution was quickly heated to 280 ºC under strong agitation. When the temperature of the solution became stable, stock $(TMS)_3P$-ODE (0.2 $mmol.mL^{-1}$, 0.5 mL) solution was rapidly injected. The solution was kept at 240 ºC for 20 minutes. Differently sized nano-crystals were obtained by adjusting the initial concentrations of zinc undecylenate and HDA.

6.6.3 Electrode modification

All operations were performed under anaerobic conditions (MBraun Lab Star Glove Box, < 0.1 ppm O_2), using freshly distilled, degassed solvent. The following protocol was used to prepare the working electrode. First, the electrode was primed by adsorbing a monolayer as a linker, which was achieved by placing 1,4-benzene dithiol (10 μL of 1 mM) in toluene onto the surface of the electrode. After complete evaporation of the thiol solution, the electrode surface was thoroughly rinsed with toluene. Following this, 10 μL of an InP nano-crystal solution were placed onto the electrode and following the evaporation of the solvent, the electrode was again rinsed with toluene. This process was repeated a further nine times to build up a nano-particle electrode assembly of 10 layers. Finally, $Fe_2(\mu\text{-}S_2)(CO)_6$ was incorporated into the structure by soaking overnight in a 3 mM toluene solution of the complex, followed by thorough rinsing with toluene.

6.6.4 Electrolysis

The electrolysis was performed in a closed photoelectrochemical cell operating with a three-electrode configuration. Platinum (Pt) gauze was used as the secondary electrode (separated from the main compartment by a frit) and Ag/AgCl-3 M NaCl as the reference electrode. The cell was flushed with dinitrogen prior to use and charged with

0.1 M aqueous $Na[BF_4]$ electrolyte. The modified gold photocathode (0.40 cm^2) was placed alongside the secondary and reference electrodes in the cell. The photocathode was illuminated using a light emitting diode array with 395 nm wavelength for 30 seconds at different potential range from -100 to -700 mV. The purpose was to determine the suitable potentials to perform the electrolysis. Electrolysis was carried out by continuously exposing the photocathode to light emitting diode for 50 minutes at a constant potential of -400 mV *vs.* Ag/AgCl while the solution was stirred at moderate speed. The gas headspace above the electrolyte was sampled using a gas-tight syringe and analysed by gas chromatography.

6.7 Dihydrogen yield calculation

From experiment, 0.50 mL of the gas headspace above the electrolyte was sampled using a gas-tight syringe and analysed by gas chromatography.

For standard, 0.50 mL H_2 gas was injected in 580 mL flask. 0.50 mL of gas was sampled and analysed by gas chromatography.

H_2 injected ($mol.L^{-1}$)

$$= \frac{0.50}{22414} x \frac{1000}{580}$$
$$= 3.85x10^{-5}$$

H_2 detected ($mol.L^{-1}$)

$$= 3.85x10^{-5} x \frac{0.0244\%}{0.40\%}$$
$$= 2.35x10^{-6}$$

where 0.0244 and 0.40 is the percentage area of H_2 detected from the cell and standard respectively.

From the cell, amount of H_2 produced,

$$= 2.35 x 10^{-6}\ mol.L^{-1} x \frac{6.9 mL}{1000 mL}$$

$$= 1.62 x 10^{-8}\ moles$$

$$= 1.62\ x\ 10^{-8}\ moles\ x\ 96{,}485\ C.mol^{-1}$$

$$= 1.56\ x 10^{-3}\ Coulombs$$

where 96,485 is Faraday constant.

From experiment, average current produced is 0.86 x 10^{-6} A.

Therefore, number of coulombs produced within 50 min of measurement time

$$= 0.86\ x\ 10^{-6}\ A\ x\ 50\ \text{min}\ \ x\ 60\ \text{sec}$$

$$= 2.58\ x 10^{-3}$$

Percentage of H_2 produced

$$= \frac{1.56 x 10^{-3}}{2.58 x 10^{-3}}\ x 100 = 60\%$$

Chapter 7

Conclusions and Future Works

The present work has contributed to the field of synthetic [FeFe]-hydrogenase active site model complexes. A wide scope of subjects, ranging from the synthesis of synthetic molecules related to [FeFe]-hydrogenase, assembled an artificial H-cluster on electrode surface, an attempt towards the H-cluster construction involving *Pyrococcus furiosus* ferredoxin, as well as building a photocathode for dihydrogen production based on modification of indium phosphide nano-crystals with simple diiron sub-site has been explored.

The work presented in this thesis can be summarised as follows. An improved synthetic route towards the tripodal ligand responsible for diiron sub-site target molecule synthesised was established.

In the exploration of electropolymerisation technique, a stable hydride intermediate of dicyanide sub-site is obtained through protonation of the complex deposited on poly(pyrrole) framework. This has given a new approach on protonation studies which is a key answer to the mechanism of molecular hydrogen production in the catalytic cycle of [FeFe]-hydrogenase. The design and synthesis of the first model of H-cluster on surface bound electropolymers *via* electropolymerisation of poly(pyrrole) derivative has been described. The electron transfer chemistry of this system has been studied by

electrochemical technique together with its mechanistic aspects of the interplay between sub-site and cluster is explored.

An approach for incorporating sub-site analogues into wild type ferredoxin of *Pyrococcus furiosus* has been established. Different types of ligands including thiophenol, ionic iron sub-site have been used to study reaction with the protein. Preliminary results are optimistic where it seems possible that chemistry at one of the iron on the robust {4Fe-4S} mutant ferredoxin can be carried out.

A robust and efficient system for the photoelectrochemical production of molecular hydrogen has been developed. This system which comprises inexpensive and non-toxic elements such as indium phosphide nano-particles, and simple iron carbonyl sub-site analogue does not rely on excited states of organic molecules/ligands, unlike most of the state of the art approaches. Thus, promising alternative for the inexpensive production of dihydrogen.

This research may open the way for future studies towards including a deeper understanding of the mechanism of action of [FeFe]-hydrogenase. This would be facilitated by work on cyanation of the model H-cluster, which would provide a closer analogue of the natural site and allow further studies of the electronic interactions between sub-site and cluster and the potential for electrocatalysis.

The assembly of new solid state materials for electrocatalysis which are likely to require the synthesis of new ligands/polymers, possessing both functionality for covalent binding of dicyanide sub-sites, electron transfer relays, proton transfer relays and possibly hemi-labile ligands. It is particularly attractive to envisage catalytic sites

embedded in a conducting polymer. Incorporating sub-sites within a functionalised polymeric environment may also provide a means of stabilising Fe(I)-Fe(II) assemblies.

Chapter 8

Appendix

Notes on characterisation techniques used

8.1 Fourier transforms infrared spectroscopy

FTIR spectroscopy is very useful in determining compounds with polar groups such as carbonyl and cyanide as these groups can give a change in dipole moment during vibration. Carbonyl and cyanide exhibit strong absorptions *i.e.* high intensity stretching bands in the FTIR spectrum. It has also been very useful to characterise different redox states of [FeFe]-hydrogenase as they exhibit very different spectra. [49] For an example, the number of carbonyl bands depends on the number of CO ligands and the symmetry of the metal complex. The carbonyl stretching frequencies in the FTIR spectrum of $[Fe_2(\mu\text{-pdt})(CO)_6]$ have been assigned by Hall and Cao (**Figure 8.1**). [273] C_{2v} symmetric, hexacarbonyl complexes of the $[Fe_2(\mu\text{-}S_2R)(CO)_6]$ type all show similar FTIR patterns in the CO region, although shifted depending on the electronic properties of the bridging dithiolate ligand.

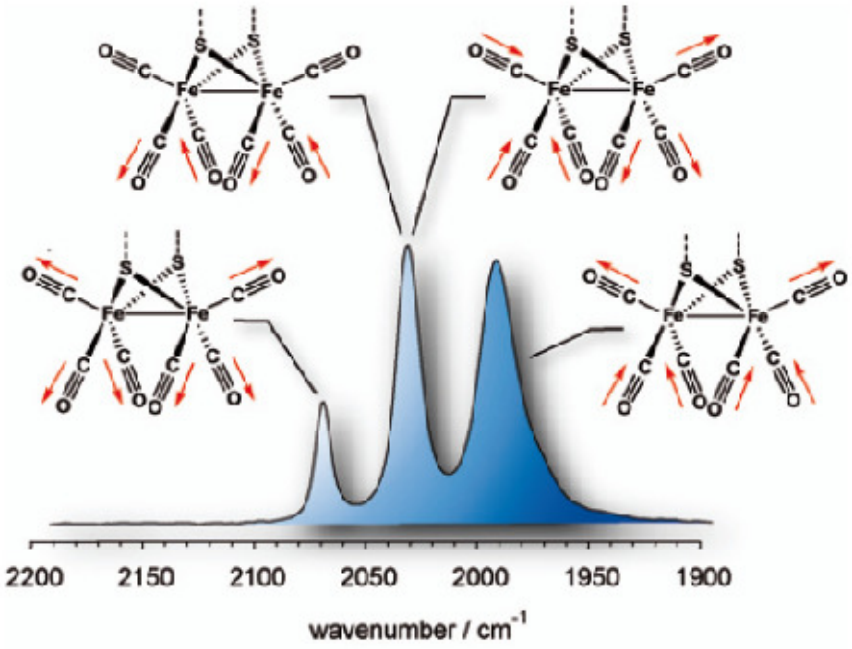

Figure 8.1. The assignments (most prominent showed) of the CO stretching frequencies of the FTIR spectra for $[Fe_2(\mu\text{-}S_2R)(CO)_6]$ complexes. The FTIR spectrum of $[Fe_2(\mu\text{-pdt})(CO)_6]$ is shown as an example (adapted from ref. [273]).

8.2 Electrochemistry

Electrochemical methods can be used as a probe of molecular orbital energy levels of the metal centre. Indeed, reduction potential is directly connected to the lowest unoccupied molecular orbital (LUMO) whereas the highest occupied molecular orbital (HOMO) is related to the oxidation potential. [274-276] The effect of substituting one ligand for another on the redox potential can also give a valuable insight into the detailed mechanism of electron transfer chemistry, which in turn can provide information on the capacity of metallo systems to electrocatalyse proton reduction. [234]

Electrode dynamics are concerned with the application of a potential to an electrolytic solution and the measure of the resulting current. Thus, electron transfer reaction between electrode and solution containing the sample can be investigated, **Scheme 8.1**.

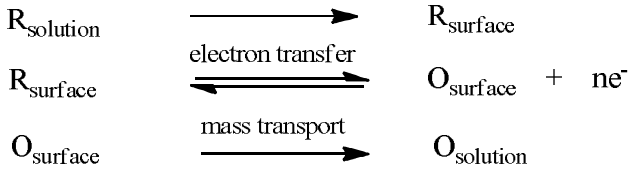

Scheme 8.1. Mass transport and electron transfer in close proximity to the electrode.

Electrochemistry offers a wide range of accessible techniques and this thesis is concerned with only a few of them. Cyclic voltammetry (CV) and bulk controlled electrolysis have been used in order to investigate the electronic properties of the chemical models of the sub-site and H-cluster.

8.3 Cyclic voltammetry (CV)

Cyclic voltammograms are recorded with stationary solutions so that electrochemical response relies mostly on "natural" diffusion on electroactive species to the electrode surface. The potential of the working electrode is swept at a desired scan rate (υ) from initial applied potential E_1 to switching potential E_2. Once E_2 is reached, the potential is then swept back towards E_1. The initial potential E_1 is chosen so that no electron transfer occurs whereas E_2 enables rapid electron transfer. A typical response for a reversible electron transfer is illustrated on **Figure 8.2**. Oxidative current is depicted as a positive wave and reductive current is depicted as a negative wave. For a rapid electron transfer, the shape of a voltammogram is intimately related to the diffusion of the studied species at the electrode surface. The first few stages of the wave are under

Nernstian control in which oxidised and reduced species are both in equilibrium, as stated in **Equation 8.1**.

$$E = E^\circ + \frac{RT}{nF} \ln \frac{[O]}{[R]} \qquad \textbf{Equation 8.1}$$

On the forward scan, the oxidised species builds up at the electrode surface ($[R]_{surface}$ tends to zero) until a maximum current is reached. Because the electrode is stationary and the solution is unstirred, the species to electrolyse (R in the present case) is only bought to the electrode surface by diffusion from the bulk. As more species is electrolysed, "fresh" species has further to diffuse to the electrode and this result in the current response dropping off. The maximum currents in oxidation and reduction are assigned as peak currents I_p^{ox} and I_p^{red}. In the case of rapid kinetics of electron transfer and full reversibility of a given process the ratio $I_p^{ox} / I_p^{red} = 1$.

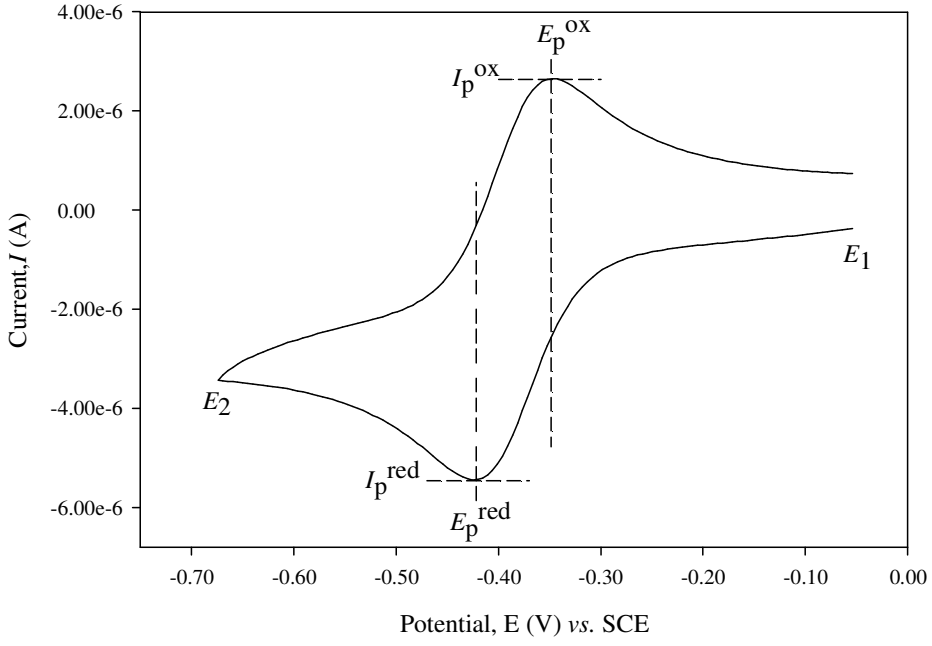

Figure 8.2. Cyclic voltammogram for a reversible electron transfer reaction (ferrocene in this case) (taken from reference [234]).

In the case of diffusion controlled systems, with reversible and irreversible processes, the peak current response applies to **Equation 8.2**. This is commonly known as the Randles-Sevcik equation from which plots of i_p *versus* $\upsilon^{1/2}$ should be linear with intercept passing through the origin.

To find out the number of electrons involved in a given process, it is possible to compare with peak current of a related molecule at the same concentration provided the two molecules have a similar D_o.

$$i_p = \left(2.69 \times 10^5\right) n^{3/2} A D_o^{1/2} v^{1/2} C_o^* \qquad \textbf{Equation 8.2}$$

With: n = number of electrons/molecule

A = electrode area (cm^2)

D_o = diffusion coefficient ($cm^2.s^{-1}$)

v = scan rate ($V.s^{-1}$)

C_o^* = bulk concentration of the electroactive species ($mol.cm^{-3}$)

Another method for calculating the n number is by looking at the anodic and cathodic peak separation for a reversible couple. Given by the Nernst equation at 25 °C, the theoretical separation, ΔE_p should b equal to $\left| E_p^{ox} - E_p^{red} \right| = 59/n$ (mV). This method has to be carefully considered as many experimental factors can influence the measurement. The half potential, $E_{1/2}$ is situated midway between the peak potential and this value should be close to standard potential, E^o of the O/R couple.

In some cases of irreversibility, because a wave is sometimes broad, it can be difficult to determine the peak potential. It is then more convenient to report $E_{p/2}$, which is the potential at ½ i_p.

Reversibility is an ideal case of cyclic voltammetry as electrolysis at the electrode surface does not always imply generation of stable species. Irreversible processes are in fact very common. Chemical reactions following electron transfer (EC type) or even more complex situations such as ECE can lead to very different and original voltammograms from which suitable mechanisms can be determined. [234]

Whereas for the case of chemically modified electrodes or surface electrochemistry, the peak current, and indeed the current at each point on the wave, is proportional to the surface coverage, Γ and potential scan rate, υ, which is in contrast to the $\upsilon^{1/2}$ dependence observed for Nernstian waves of diffusing species. [234]

$$i_p = \frac{n^2F^2\Gamma A v}{4RT}$$

Equation 8.3

With: n = number of electrons/molecule

A = electrode area (cm^2)

F = Faraday constant (C)

v = scan rate ($V.s^{-1}$)

Γ = surface coverage ($mol.cm^{-2}$)

R = gas constant ($J.mol^{-1}.K^{-1}$)

T = absolute temperature (K)

The area under the reduction wave, corrected for any residual current, represents the charge required for the full reduction of the layer, that is, $nFA\Gamma$. The anodic wave on scan reversal is the mirror image of the cathodic wave reflected across the potential axis. For an ideal Nernstian reaction under Langmuir isotherm conditions, $E_p^{ox} = E_p^{red}$. [234]

8.4 Electrolysis

Electrolysis at a potential that slightly encompasses a redox process (controlled potential) implies that the current is maintained at a maximum value. Coulometric measurements were carried out here so that number of coulombs was used to determine the number of electrons involved per molecule electrolysed (**Equation 8.4**).

$$Q_o = n F N_o \qquad \textbf{Equation 8.4}$$

With Q_o = number of coulombs at completion of electrolysis

N_o = number of moles initially present in solution.

Alternatively, as the current decreases sometimes very slowly to zero, it can be useful to plot i_L *versus* Q_t so that Q_o is determined at the intercept of $i_L = 0$.

The time-scale of such technique, typically between 10 and 60 minutes, is significantly longer than that of voltammetric methods and this implies that chemical reaction following electron transfer have more chance to occur. Therefore, this method can only be applied in the case where electro-generated products are reasonably stable in time-scale of the experiment.